

Jordan Journal of P H Y S I C S

An International Peer-Reviewed Research Journal

Volume 14, No. 2, June 2021, Thu al-Qi'dah 1442 H

Jordan Journal of Physics (JJP): An International Peer-Reviewed Research Journal funded by the Scientific Research Support Fund, Jordan, and published quarterly by the Deanship of Research and Graduate Studies, Yarmouk University, Irbid, Jordan.

EDITOR-IN-CHIEF:

Ibrahim O. Abu Al-Jarayesh

Department of Physics, Yarmouk University, Irbid, Jordan.

ijaraysh@yu.edu.jo

EDITORIAL BOARD:	ASSOCIATE EDITORIAL BOARD
<p>Prof. Nabil Y. Ayoub <i>President, American University of Madaba, Madaba, Jordan.</i> nabil.ayoub@gju.edu.jo</p> <p>Prof. Jamil M. Khalifeh (May God have mercy on him) <i>Department of Physics, University of Jordan, Amman, Jordan.</i> jkhalifa@ju.edu.jo</p> <p>Prof. Tareq F. Hussein <i>Department of Physics, The University of Jordan, Amman, Jordan.</i> t.hussein@ju.edu.jo</p> <p>Prof. Marwan S. Mousa <i>Department of Physics, Mu'tah University, Al-Karak, Jordan.</i> mmousa@mutah.edu.jo</p> <p>Prof. Mohammad Al-Sugheir <i>Department of Physics, The Hashemite University, Zarqa, Jordan.</i> msugh@hu.edu.jo</p> <p>Prof. Abdalmajeid M. Alyassin <i>Department of Physics, Yarmouk University, Irbid, Jordan.</i> alyassin@yu.edu.jo</p> <p>Prof. M-Ali H. Al-Akhras (AL-Omari) <i>Department of Physics, Jordan University of Science & Technology, Irbid, Jordan.</i> alakmoh@just.edu.jo</p> <p>Prof. Ibrahim A. Bsoul <i>Department of Physics, Al al-Bayt University, Mafraq, Jordan.</i> Ibrahimbsoul@yahoo.com</p>	<p>Prof. Mark Haggmann <i>Desert Electronics Research Corporation, 762 Lacey Way, North Salt Lake 84064, Utah, U. S. A.</i> MHaggmann@NewPathResearch.Com</p> <p>Dr. Richard G. Forbes <i>Dept. of Electrical and Electronic Engineering, University of Surrey, Advanced Technology Institute and Guildford, Surrey GU2 7XH, UK.</i> r.forbes@surrey.ac.uk</p> <p>Prof. Roy Chantrell <i>Physics Department, The University of York, York, YO10 5DD, UK.</i> roy.chantrell@york.ac.uk</p> <p>Prof. Susamu Taketomi <i>2-35-8 Higashisakamoto, Kagoshima City, 892-0861, Japan.</i> staketomi@hotmail.com</p>

Editorial Secretary: Majdi Al-Shannaq.

Languages Editor: Haider Al-Momani

Manuscripts should be submitted to:

Prof. Ibrahim O. Abu Al-Jarayesh
Editor-in-Chief, Jordan Journal of Physics
Deanship of Research and Graduate Studies
Yarmouk University-Irbid-Jordan
Tel. 00 962 2 7211111 Ext. 2075
E-mail: jjp@yu.edu.jo
Website: <http://Journals.yu.edu.jo/jjp>

Jordan Journal of
P H Y S I C S

An International Peer-Reviewed Research Journal

Volume 14, No. 2, June 2021, Thu al-Qi'dah 1442 H

INTERNATIONAL ADVISORY BOARD

Prof. Dr. Ahmad Saleh

Department of Physics, Yarmouk University, Irbid, Jordan.
salema@yu.edu.jo

Prof. Dr. Aurore Savoy-Navarro

LPNHE Université de Paris 6/IN2P3-CNRS, Tour 33, RdC 4,
Place Jussieu, F 75252, Paris Cedex 05, France.
auore@lphnep.in2p3.fr

Prof. Dr. Bernard Barbara

Laboratoire Louis Neel, Salle/Room: D 108, 25, Avenue des
Martyrs BP 166, 38042-Grenoble Cedex 9, France.
Barbara@grenoble.cnrs.fr

Prof. Dr. Bruno Guiderdoni

Observatoire Astronomique de Lyon, g, avenue Ch. Antre-F-69561,
Saint Genis Laval Cedex, France.
Bruno.guiderdoni@olos.univ-lyon1.fr

Prof. Dr. Buford Price

Physics Department, University of California, Berkeley, CA 94720,
U. S. A.
bprice@berkeley.edu

Prof. Dr. Colin Cough

School of Physics and Astronomy, University of Birmingham, B15
2TT, U. K.
c.gough@bham.ac.uk

Prof. Dr. Desmond Cook

Department of Physics, Condensed Matter and Materials Physics
Research Group, Old Dominion University, Norfolk, Virginia
23529, U. S. A.
Dcook@physics.odu.edu

Prof. Dr. Evgeny Sheshin

MIPT, Institutskij per. 9, Dogoprudnyi 141700, Russia.
sheshin@lafeet.mipt.ru

Prof. Dr. Hans Ott

Laboratorium fuer Festkorperphysik, ETH Honggerberg, CH-
8093 Zurich, Switzerland.
ott@solid.phys.ethz.ch

Prof. Dr. Herwig Schopper

President SESAME Council, Chairman Scientific Board UNESCO
IBSP Programme, CERN, 1211 Geneva, Switzerland.
Herwig.Schopper@cern.ch

Prof. Dr. Humam Ghassib

Department of Physics, The University of Jordan, Amman 11942,
Jordan.
humamg@ju.edu.jo

Prof. Dr. Khalid Touqan

Chairman of Jordan Atomic Energy Commission, Amman, Jordan.

Prof. Dr. Nasr Zubeidey

President: Al-Zaytoonah University of Jordan, Amman, Jordan.
President@alzaytoonah.edu.jo

Prof. Dr. Patrick Roudeau

Laboratoire de l'Accelérateur, Lineaire (LAL), Université Paris-
Sud 11, Batiment 200, 91898 Orsay Cedex, France.
roudeau@mail.cern.ch

Prof. Dr. Paul Chu

Department of Physics, University of Houston, Houston, Texas
77204-5005, U. S. A.
Ching-Wu.Chu@mail.uh.edu

Prof. Dr. Peter Dowben

Nebraska Center for Materials and Nanoscience, Department of
Physics and Astronomy, 255 Behlen Laboratory (10th and R
Streets), 116 Brace Lab., P. O. Box 880111, Lincoln, NE 68588-
0111, U. S. A.
pdowben@unl.edu

Prof. Dr. Peter Mulser

Institute fuer Physik, T.U. Darmstadt, Hochschulstr. 4a, 64289
Darmstadt, Germany.
Peter.mulser@physik.tu-darmstadt.de

Prof. Dr. Rasheed Azzam

Department of Electrical Engineering, University of New Orleans
New Orleans, Louisiana 70148, U. S. A.
razzam@uno.edu

Prof. Dr. Shawqi Al-Dallal

Department of Physics, Faculty of Science, University of Bahrain,
Manamah, Kingdom of Bahrain.

Prof. Dr. Wolfgang Nolting

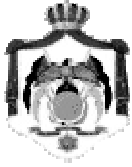
Institute of Physics / Chair: Solid State Theory, Humboldt-
University at Berlin, Newtonstr. 15 D-12489 Berlin, Germany
Wolfgang.nolting@physik.hu-berlin.de

Prof. Dr. Ingo Hofmann

GSI Darmstadt, Planckstr. 1, 64291, Darmstadt, Germany.
i.hofmann@gsi.de

Prof. Dr. Jozef Lipka

Department of Nuclear Physics and Technology, Slovak University
of Technology, Bratislava, Ilkovicova 3, 812 19 Bratislava,
Slovakia.
Lipka@elf.stuba.sk



The Hashemite Kingdom of Jordan



Yarmouk University

Jordan Journal of
PHYSICS

An International Peer-Reviewed Research Journal
Funded by the Scientific Research Support Fund

Volume 14, No. 2, June 2021, Thu al-Qi'dah 1442 H

Instructions to Authors

Instructions to authors concerning manuscript organization and format apply to hardcopy submission by mail, and also to electronic online submission via the Journal homepage website (<http://jip.yu.edu.jo>).

Manuscript Submission

1- **E-mail to** : jip@yu.edu.jo

2- **Online**: Follow the instructions at the journal homepage website.

Original *Research Articles*, *Communications* and *Technical Notes* are subject to critical review by minimum of two competent referees. Authors are encouraged to suggest names of competent reviewers. *Feature Articles* in active Physics research fields, in which the author's own contribution and its relationship to other work in the field constitute the main body of the article, appear as a result of an invitation from the Editorial Board, and will be so designated. The author of a *Feature Article* will be asked to provide a clear, concise and critical status report of the field as an introduction to the article. *Review Articles* on active and rapidly changing Physics research fields will also be published. Authors of *Review Articles* are encouraged to submit two-page proposals to the Editor-in-Chief for approval. Manuscripts submitted in *Arabic* should be accompanied by an Abstract and Keywords in English.

Organization of the Manuscript

Manuscripts should be typed double spaced on one side of A4 sheets (21.6 x 27.9 cm) with 3.71 cm margins, using Microsoft Word 2000 or a later version thereof. The author should adhere to the following order of presentation: Article Title, Author(s), Full Address and E-mail, Abstract, PACS and Keywords, Main Text, Acknowledgment. Only the first letters of words in the Title, Headings and Subheadings are capitalized. Headings should be in **bold** while subheadings in *italic* fonts.

Title Page: Includes the title of the article, authors' first names, middle initials and surnames and affiliations. The affiliation should comprise the department, institution (university or company), city, zip code and state and should be typed as a footnote to the author's name. The name and complete mailing address, telephone and fax numbers, and e-mail address of the author responsible for correspondence (designated with an asterisk) should also be included for official use. The title should be carefully, concisely and clearly constructed to highlight the emphasis and content of the manuscript, which is very important for information retrieval.

Abstract: A one paragraph abstract not exceeding 200 words is required, which should be arranged to highlight the purpose, methods used, results and major findings.

Keywords: A list of 4-6 keywords, which expresses the precise content of the manuscript for indexing purposes, should follow the abstract.

PACS: Authors should supply one or more relevant PACS-2006 classification codes, (available at <http://www.aip.org/pacs/pacs06/pacs06-toc.html>)

Introduction: Should present the purpose of the submitted work and its relationship to earlier work in the field, but it should not be an extensive review of the literature (e.g., should not exceed 1 ½ typed pages).

Experimental Methods: Should be sufficiently informative to allow competent reproduction of the experimental procedures presented; yet concise enough not to be repetitive of earlier published procedures.

Results: should present the results clearly and concisely.

Discussion: Should be concise and focus on the interpretation of the results.

Conclusion: Should be a brief account of the major findings of the study not exceeding one typed page.

Acknowledgments: Including those for grant and financial support if any, should be typed in one paragraph directly preceding the References.

References: References should be typed double spaced and numbered sequentially in the order in which they are cited in the text. References should be cited in the text by the appropriate Arabic numerals, enclosed in square brackets. Titles of journals are abbreviated according to list of scientific periodicals. The style and punctuation should conform to the following examples:

1. Journal Article:

- a) Heisenberg, W., Z. Phys. 49 (1928) 619.
- b) Bednorz, J. G. and Müller, K. A., Z. Phys. B64 (1986) 189
- c) Bardeen, J., Cooper, L.N. and Schrieffer, J. R., Phys. Rev. 106 (1957) 162.
- d) Asad, J. H., Hijjawi, R. S., Sakaji, A. and Khalifeh, J. M., Int. J. Theor. Phys. 44(4) (2005), 3977.

2. Books with Authors, but no Editors:

- a) Kittel, C., "Introduction to Solid State Physics", 8th Ed. (John Wiley and Sons, New York, 2005), chapter 16.
- b) Chikazumi, S., C. D. Graham, JR, "Physics of Ferromagnetism", 2nd Ed. (Oxford University Press, Oxford, 1997).

3. Books with Authors and Editors:

- a) Allen, P. B. "Dynamical Properties of Solids", Ed. (1), G. K. Horton and A. A. Maradudin (North-Holland, Amsterdam, 1980), p137.
- b) Chantrell, R. W. and O'Grady, K., "Magnetic Properties of Fine Particles" Eds. J. L. Dormann and D. Fiorani (North-Holland, Amsterdam, 1992), p103.

4. Technical Report:

Purcell, J. "The Superconducting Magnet System for the 12-Foot Bubble Chamber", report ANL/HEP6813, Argonne Natl. Lab., Argonne, III, (1968).

5. Patent:

Bigham, C. B., Schneider, H. R., US patent 3 925 676 (1975).

6. Thesis:

Mahmood, S. H., Ph.D. Thesis, Michigan State University, (1986), USA (Unpublished).

7. Conference or Symposium Proceedings:

Blandin, A. and Lederer, P. Proc. Intern. Conf. on Magnetism, Nottingham (1964), P.71.

8. Internet Source:

Should include authors' names (if any), title, internet website, URL, and date of access.

9. Prepublication online articles (already accepted for publication):

Should include authors' names (if any), title of digital database, database website, URL, and date of access.

For other types of referenced works, provide sufficient information to enable readers to access them.

Tables: Tables should be numbered with Arabic numerals and referred to by number in the Text (e.g., Table 1). Each table should be typed on a separate page with the legend above the table, while explanatory footnotes, which are indicated by superscript lowercase letters, should be typed below the table.

Illustrations: Figures, drawings, diagrams, charts and photographs are to be numbered in a consecutive series of Arabic numerals in the order in which they are cited in the text. Computer-generated illustrations and good-quality digital photographic prints are accepted. They should be black and white originals (not photocopies) provided on separate pages and identified with their corresponding numbers. Actual size graphics should be provided, which need no further manipulation, with lettering (Arial or Helvetica) not smaller than 8 points, lines no thinner than 0.5 point, and each of uniform density. All colors should be removed from graphics except for those graphics to be considered for publication in color. If graphics are to be submitted digitally, they should conform to the following minimum resolution requirements: 1200 dpi for black and white line art, 600 dpi for grayscale art, and 300 dpi for color art. All graphic files must be saved as TIFF images, and all illustrations must be submitted in the actual size at which they should appear in the journal. Note that good quality hardcopy original illustrations are required for both online and mail submissions of manuscripts.

Text Footnotes: The use of text footnotes is to be avoided. When their use is absolutely necessary, they should be typed at the bottom of the page to which they refer, and should be cited in the text by a superscript asterisk or multiples thereof. Place a line above the footnote, so that it is set off from the text.

Supplementary Material: Authors are encouraged to provide all supplementary materials that may facilitate the review process, including any detailed mathematical derivations that may not appear in whole in the manuscript.

Revised Manuscript and Computer Disks

Following the acceptance of a manuscript for publication and the incorporation of all required revisions, authors should submit an original and one more copy of the final disk containing the complete manuscript typed double spaced in Microsoft Word for Windows 2000 or a later version thereof. All graphic files must be saved as PDF, JPG, or TIFF images.

Allen, P.B., “.....”, in: Horton, G.K., and Muradudin, A. A., (eds.), “Dynamical.....”, (North.....), pp....

Reprints

Twenty (20) reprints free of charge are provided to the corresponding author. For orders of more reprints, a reprint order form and prices will be sent with the article proofs, which should be returned directly to the Editor for processing.

Copyright

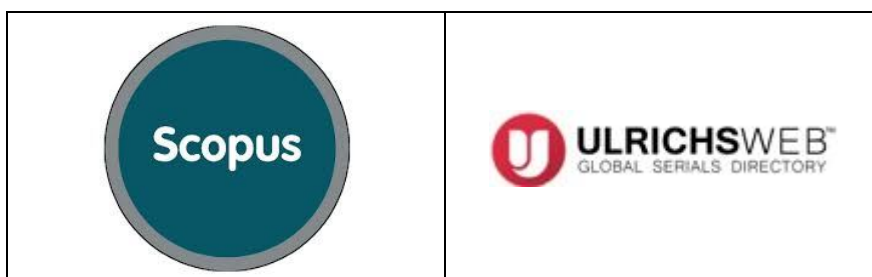
Submission is an admission by the authors that the manuscript has neither been previously published nor is being considered for publication elsewhere. A statement transferring copyright from the authors to Yarmouk University is required before the manuscript can be accepted for publication. The necessary form for such transfer is supplied by the Editor-in-Chief. Reproduction of any part of the contents of a published work is forbidden without a written permission by the Editor-in-Chief.

Disclaimer

Opinions expressed in this Journal are those of the authors and neither necessarily reflects the opinions of the Editorial Board or the University, nor the policy of the Higher Scientific Research Committee or the Ministry of Higher Education and Scientific Research. The publisher shoulders no responsibility or liability whatsoever for the use or misuse of the information published by JJP.

Indexing

JJP is currently indexing in:



Jordan Journal of
P H Y S I C S

An International Peer-Reviewed Research Journal

Volume 14, No. 2, June 2021, Thu al-Qi'dah 1442 H

Table of Contents:

Articles	Pages
Structural and Optical Characterization of Thermally Oxidized Titanium Thin Films Prepared by Ion Beam-assisted Deposition (IBAD) Technique N. Hamdadou and I. M. Odeh	101-109
Calculation of Darken Stability Functions of Al-In and Bi-Zn Binary Liquid Alloys O. W. Abodunrin and A. A. Ajayi	111-116
Multifactor Authentication Car Tracking System Using Fingerprint Verification Ndianabasi. H. Valentine, Ogrri J. Ushie and Emmanuel I. Akaerue	117-128
Spatial and Temporal Variation of Clearness Index in Iraq Waleed I. Al-Rijabo, Rajaa A. Basheer and Amal M. Banoosh	129-138
Spectroscopic and Quantum Chemical Investigations of Hypothetical m-Diacetylaminoazopyrimidine and Its Photovoltaic Properties Hitler Louis, Israel Solomon Etim, Nelson Ibe Nzeata and Ayuk Usaji Atu	139-154
Coupling of Upper Hybrid Surface Plasmon Modes in Magnetoplasma Waveguide Structure Fuad Rawwagah	155-160
Factors Motivating Virtual Lab Simulations Adoption in Secondary School Physics Instruction in Jordan Salah M. Jaradat, Marwan S. Mousa, Donald Dunn and Casey Reason	161-167
Fullerite Nano-materials as a Moderator in Neutron Irradiators with Radium Sources: Feasibility and Advantages F. Qamar and M. Nahili	169-176
Comparing of the Natural Radioactivity in Soil Samples of University at Al-Husseineya and Al-Mothafeen Sites of Kerbala, Iraq Abrar A. Ibrahim, Abdalsattar K. Hashim and Ali A. Abojassim	177-191

Structural and Optical Characterization of Thermally Oxidized Titanium Thin Films Prepared by Ion Beam-assisted Deposition (IBAD) Technique

N. Hamdadou^a and I. M. Odeh^b

^a *Laboratoire de Micro et de Nanophysique (LaMiN), Ecole Nationale Polytechnique d'Oran (ENPOran), BP 1523 El Mnaouer, Oran 31000, Algeria.*

^b *Physics Department, Yarmouk University, Irbid 21163, Jordan.*

Doi: <https://doi.org/10.47011/14.2.1>

Received on: 28/10/2019;

Accepted on: 11/06/2020

Abstract: Titanium oxide (TiO₂) thin films have been grown by thermal oxidation of sputtered Titanium (Ti) thin layers using ion beam-assisted deposition (IBAD). X-ray diffraction showed that prior to oxidation, the films are composed of hexagonal crystallites of Ti. After oxidation, a film structure transition occurs from monoclinic β -TiO₂ type to tetragonal anatase type as the annealing temperature of Ti layer is increased from 250 °C to 550 °C. The film thickness was about 230 nm. Visualization and scanning by atomic force microscope (AFM) revealed a low roughness of the samples, which increases when the annealing temperature is increased. The optical transmittances of the films in the visible spectrum were in the range of 85-95%. The values of optical band gap have been estimated to be 3.43 eV and 3.61 eV, for thin films annealed at 250°C and 550°C, respectively.

Keywords: TiO₂ thin film, IBAD, XRD, Structural and optical properties.

Introduction

Due to the unusual optical and electronic properties of transparent conducting oxides, attention has been paid to these materials for various applications. Titanium oxide (TiO₂) is a large bandgap semiconductor with interesting properties. It is transparent to visible light, has a high refractive index (at $\lambda = 550$ nm, $n = 2.54$ for anatase or 2.75 for rutile) and low absorption and consequently, it is widely used as an optical coating material [1, 2]. Also, it potentially has electronic device applications, such as dye sensitized photovoltaic cells, gas sensors, electrochromic and planar wave guides [3-5]. The dielectric constant of TiO₂ is high ($\epsilon > 100$); therefore, it is suggested as an alternative for gate dielectrics to SiO₂ for memory and logic devices [6].

TiO₂ crystallizes in four polymorphic forms: anatase (tetragonal), rutile (tetragonal), brookite

(orthorhombic) and β -TiO₂ (monoclinic) [7]. Anatase is the preferred phase for photo-induced applications, which justifies the research efforts put on its synthesis and on the study of its different properties. The photocatalytic application has been found to vary with its structural form and is reportedly higher in the anatase form compared to other forms [8-10].

A wide range of techniques have been used to prepare TiO₂ thin films, such as sputtering [11], electron beam evaporation [12, 13], pulsed laser deposition [14], chemical vapor deposition (CVD) [15] and sol-gel process [16]. However, it has been found that obtaining TiO₂ thin films, which are stable and have the properties required for the applications, is not always obvious. Indeed, the continuation of work on TiO₂ thin film preparation seems necessary. Therefore, the aim of the present work is to prepare post-deposition thermally oxidized TiO₂ thin films

having good crystalline qualities with a reproducible process. Therefore, we have used Ion Beam Assisted (sputtering) Deposition (IBAD) technique to prepare our samples. To the best of our knowledge, this technique has not been used previously in a similar experiment, which motivated us to do this work.

Experimental Techniques

TiO₂ Thin Films Preparation

The substrates used were soda lime glasses of dimensions (25×8×1) mm³; they were cleaned in an ultrasonic bath with acetone to remove any greasy traces, followed by alcohol and were then

rinsed in running distilled water. Titanium thin layers of about 80 nm thickness have been deposited by simultaneous reactive DC sputtering and ion beam-assisted deposition (IBAD) technique. Fig.1 shows the actual setup and vacuum chamber during sample deposition.

We have used an End-Hall type ion beam source and a rotating substrate holder specifically designed, built and retrofitted to the vacuum chamber in such a way that ions from the source were directed to impinging onto the rotating substrate holder at about 50–55 degrees during deposition.



FIG. 1. Deposition set-up for the preparation of titanium thin films.

A low-tension high-current transformer supplied the necessary power to the W-filament of the ion source during deposition. An independent power supply (HP 6521A) supplied the accelerating voltages of 200–300 V applied to the ion source such that the ions leaving the source would have an energy of about 100–150 eV. A 75-mm DC magnetron sputtering accessory (Edwards, UK) fitted with a high purity target (Titanium) formed the main source of titanium atoms.

A novel substrate holder (Rotating Hexa-Holder) capable of loading six substrates simultaneously was designed and constructed specifically for this type of sample deposition, as shown in Fig. 1. The distance between the glass substrate and the source (Ti) target was kept at about 10 cm. A 1 kW DC power supply (MDX 1 K Magnetron Drive, Advanced Energy, USA) delivered the DC power to the water-cooled titanium target. Thoroughly cleaned glass substrates were used throughout this work. In

addition to normal cleaning, glass substrates were bombarded with the ion source for five minutes prior to deposition to remove any traces from the surface. The films deposited were annealed at temperatures of 250°C, 350°C, 450°C and 550°C, for 2 hours. Annealing was conducted in a programmable MAGHMA THERM type oven.

TiO₂ Thin Films Characterization

The films structures was examined by BRUKER D8 diffractometer using Cu K α ₁ radiation ($\lambda=1.5406$ Å). Diffractograms were recorded from 10° to 90° with a step of 0.01°. The full width at half-maximum (FWHM) of the diffraction peaks was given directly by the X'Pert software program. The film thickness and axial roughness were checked by BRUKER Dektak XT type profilometer. AFM images were acquired using a Flex-Axiom Nanosurf system. Imaging was performed in phase contrast mode and image dimensions were 500 nm x 500 nm and 1000 nm x 1000 nm. Optical measurements

have been carried out in the wavelength range 190 – 1100 nm, using a 210 SPECORD Plus UV-Visible spectrophotometer.

Experimental Results and Discussion

XRD Analysis

The structure of the films was determined by XRD, Figs. 2 and 3. The films without annealing

crystallized in the Ti hexagonal structure, Fig. 2. The peaks are indexed using the ICDD card N° 44-1294. The peak at 47.606° is attributed to SiO₂ of the glass substrate referring to the ICDD card N°04-0379.

Fig. 3 shows XRD patterns of the films after annealing at 250 °C, 350 °C, 450 °C and 550 °C, for 2 hours.

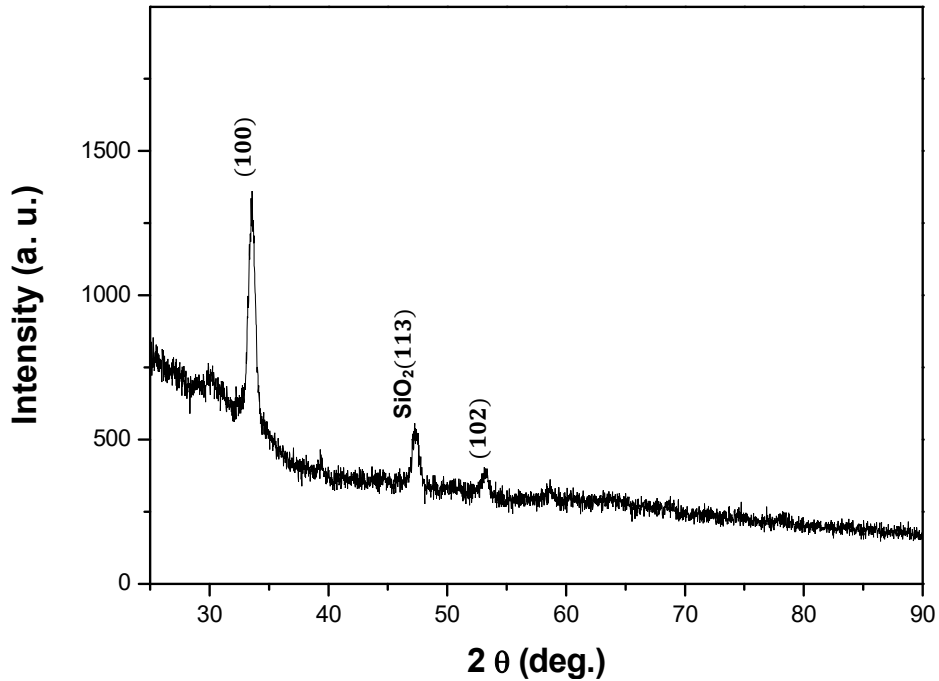


FIG. 2. XRD pattern of Ti thin film prepared by IBAD process.

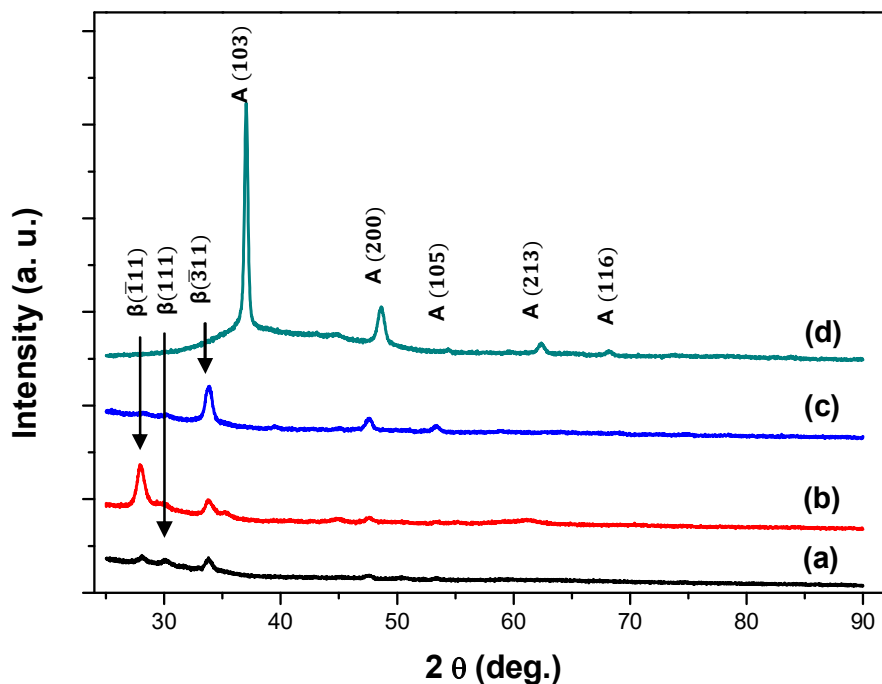


FIG. 3. XRD patterns of thin films obtained after annealing at 250°C (a), 350°C (b), 450°C (c) and 550°C (d), for 2 h.

Relationships used to deduce lattice parameters for hexagonal, monoclinic and tetragonal structure are respectively [17]:

$$\frac{1}{d_{hkl}^2} = \frac{4h^2 + hk + k^2}{3a^2} + \frac{l^2}{c^2} \quad (1)$$

$$\frac{1}{d_{hkl}^2} = \frac{h^2}{a^2 \sin^2 \beta} + \frac{k^2}{b^2} + \frac{l^2}{c^2 \sin^2 \beta} - \frac{2hl \cos \beta}{ac \sin^2 \beta} \quad (2)$$

$$\frac{1}{d_{hkl}^2} = \frac{h^2 + k^2}{a^2} + \frac{l^2}{c^2} \quad (3)$$

where a , c and β are lattice parameters and d_{hkl} is the reticular distance for the (hkl) plane family.

The average grain size D was calculated using Scherrer formula [18]:

$$D = K \frac{\lambda}{\beta \cos \theta} \quad (4)$$

where $K = 0.9$, $\lambda = 1.5406 \text{ \AA}$ and β is the full width at half maximum (FWHM) of the diffraction peaks. β was calculated by Warren formula [19]:

$$\beta^2 = B^2 - b^2 \quad (5)$$

where B is the measured peak width and b is the instrumental broadening, which is equal to 0.09° in this case.

ICDD card references, crystalline structure, lattice parameters and mean grain sizes deduced from different diffractograms are reported in Table 1.

TABLE 1. Crystalline parameters of thin films of Ti and TiO₂.

Thin film	ICDD card reference	Structure	Lattice parameters	Mean grain size D (nm)
Before annealing	44-1294	Hexagonal	$a = 2.990 \text{ \AA}$ $c = 4.515 \text{ \AA}$	26
Annealed at 250°C for 2h	46-1238	Monoclinic	$a = 12.163 \text{ \AA}$ $b = 3.735 \text{ \AA}$ $c = 6.513 \text{ \AA}$ $\beta = 107.29^\circ$	29
Annealed at 350°C for 2h	46-1238 and 21-1272	- Monoclinic - Tetragonal Anatase type (105)	$a = 12.163 \text{ \AA}$ $b = 3.735 \text{ \AA}$ $c = 6.513 \text{ \AA}$ $\beta = 107.29^\circ$ $a = b = 3.741 \text{ \AA}$ $c = 9.582 \text{ \AA}$	28 20
Annealed at 450°C for 2h	46-1238 and 21-1272	- Monoclinic - Tetragonal Anatase type (105)	$a = 12.163 \text{ \AA}$ $b = 3.735 \text{ \AA}$ $c = 6.513 \text{ \AA}$ $\beta = 107.29^\circ$ $a = b = 3.741 \text{ \AA}$ $c = 9.582 \text{ \AA}$	28 20
Annealed at 550 °C for 2h	21-1272	Tetragonal Anatase type	$a = b = 3.741 \text{ \AA}$ $c = 9.582 \text{ \AA}$	28

A phase transition between monoclinic β - TiO₂ structure and tetragonal anatase structure is observed when the annealing temperature is increased from 250 °C to 550 °C. The grain size is not affected by the increase of annealing temperature. The presence of the two structures at the intermediate temperatures 350 °C and 450 °C confirms this transition. The transformation of the structure from monoclinic to tetragonal

under the effect of temperature means a transition to a more ordered structure. Therefore, the crystallinity seems to improve with annealing temperature. This is explained by the fact that on annealing at elevated temperatures, atoms acquire high enough ability to organize themselves in a more crystalline arrangement [20, 21].

AFM Visualization

Images of TiO₂ thin film surfaces were taken at scan ranges of 500 nm and 1000 nm, Figs.4 and 5. The values of roughness parameters as the arithmetic mean height Sa, the root-mean-square height Sq, the maximum height Sz, the maximum peak height Sp and the maximum pit height Sv, are reported in Table 2.

The surface roughness of the sample annealed at 550°C (4.48 nm rms) slightly increased compared to the one annealed at 250°C (3.01 nm rms). This is also reflected by the mean height of the analyzed grains (2.19 nm vs. 2.01 nm). The phase contrast is strong at grain boundaries. This contrast might be due to crosstalk with topographic features.

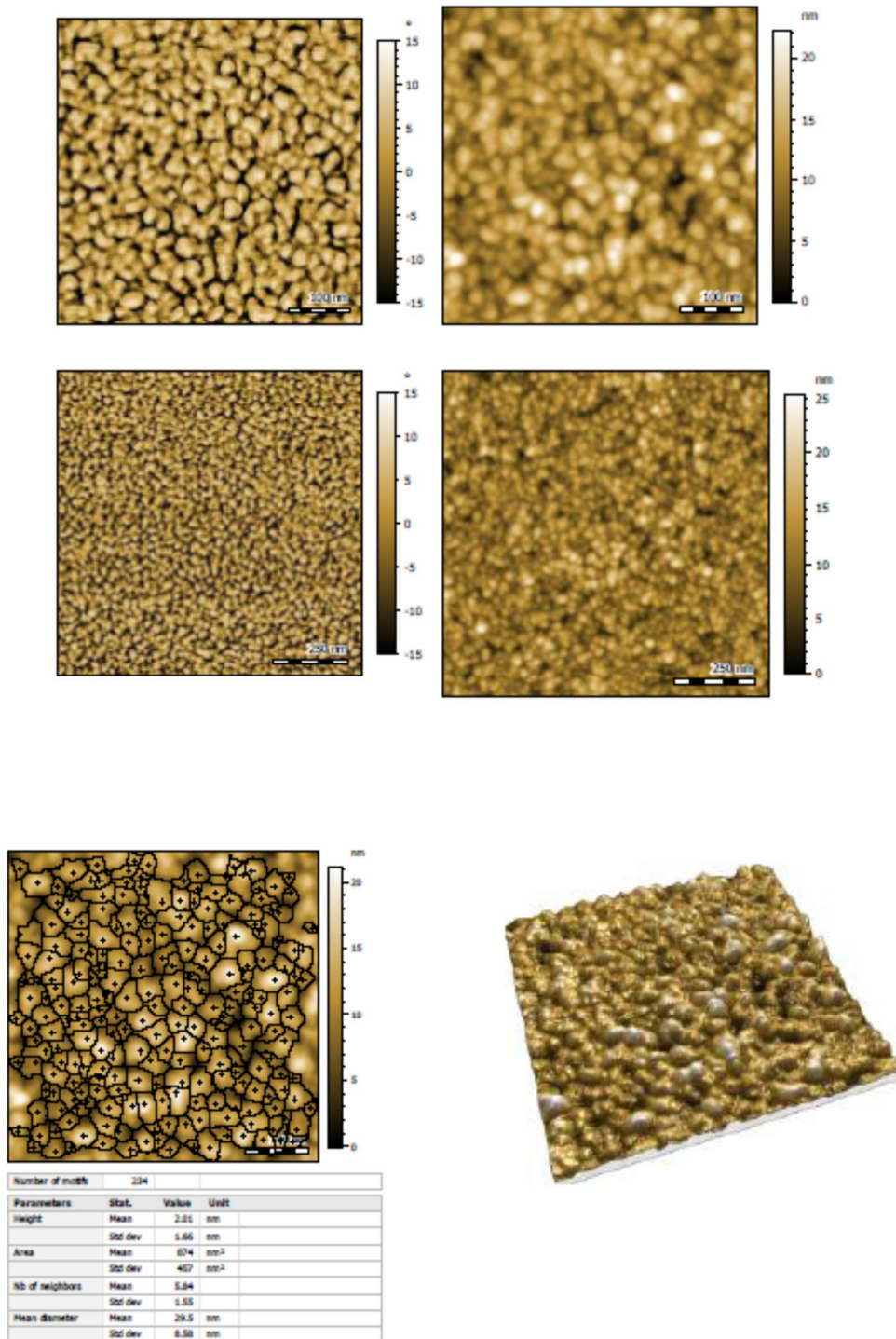


FIG. 4. AFM images for TiO₂ thin film obtained after annealing at 250°C for 2 h.

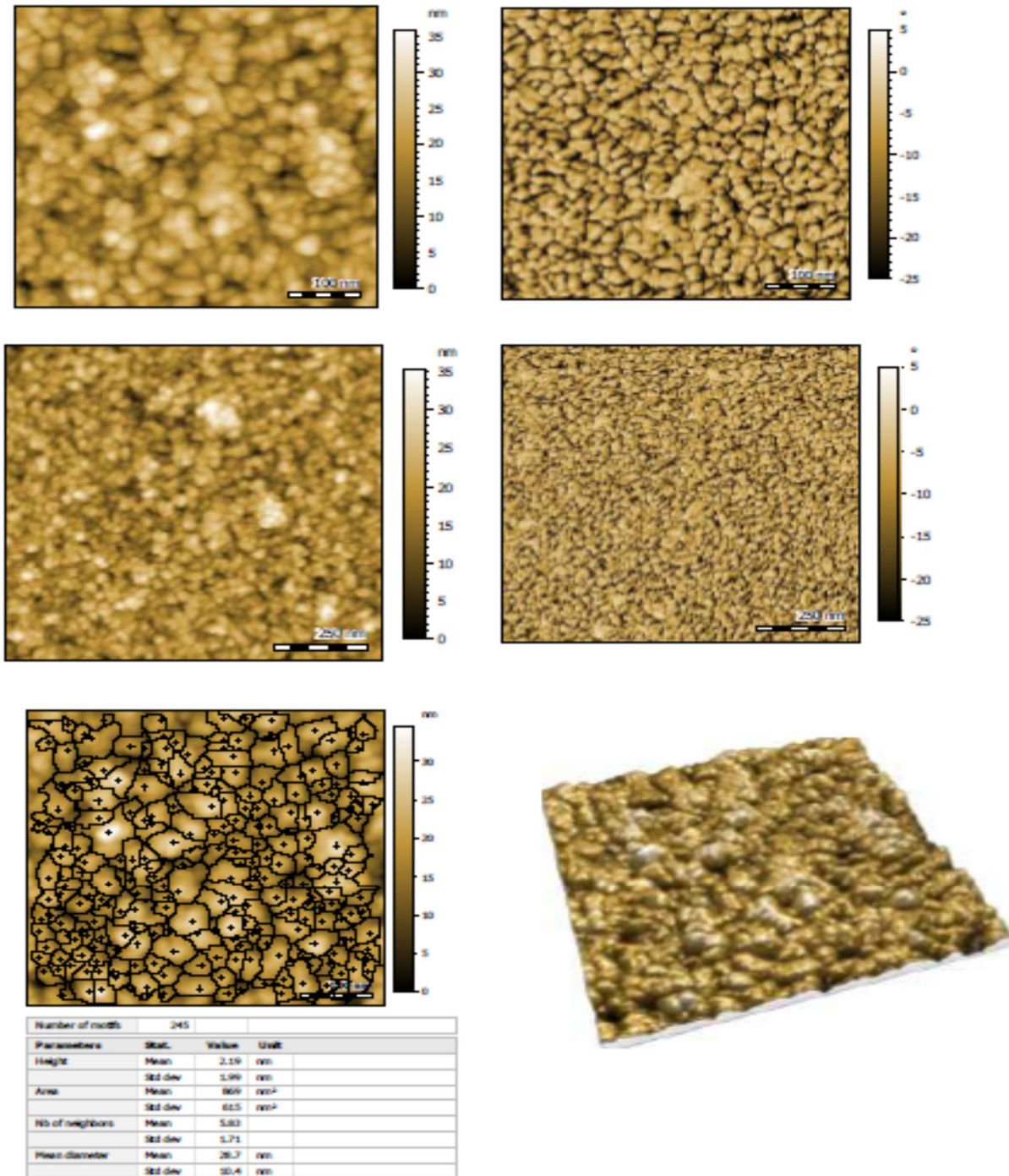


FIG. 5. AFM images for TiO₂ thin film obtained after annealing at 550°C for 2 h.

TABLE 2. Roughness and grain parameters of TiO₂ thin films obtained after annealing for 2 h at 250 °C and 550 °C.

Thin film obtained at roughness and grain parameters	250 °C	550 °C
Sa (Arithmetic Mean Height) (nm)	2.38	3.58
Sq (Root Mean Square Height) (nm)	3.01	4.48
Sz (Maximum Height) (nm)	22.20	36.00
Sp (Maximum Peak Height) (nm)	11.20	17.60
Sv (Maximum Pit Height) (nm)	11.10	18.40
Mean Grain Size (nm)	29.96	28.80
Mean Number of Grain Neighbors	5.84	5.83

Optical Measurements

Optical transmittance, Fig. 6, absorption coefficient, Figs. 7 and 8 and optical energy gap, Fig. 9, of thermally oxidized Titanium films

have exhibited high transmission of 85 - 90% in the wavelength range of 300 – 800 nm and wide energy gap, in agreement with published data.

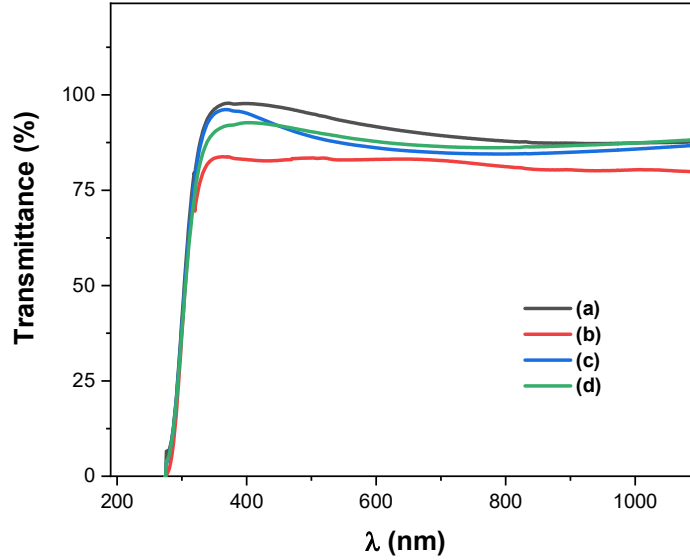


FIG. 6. Transmittance spectra *versus* wavelength for thin films obtained at 250°C (a), 350°C (b), 450°C (c) and 550°C (d), for 2 hours.

The results of the absorption coefficient calculation for different samples are provided in Figs. 7 and 8. From the transmission spectra and the thickness determined by the profilometer, we calculated the absorption coefficients using the following relation [22]:

$$\alpha = \frac{1}{d} \ln\left(\frac{100}{T(\%)}\right), \quad (6)$$

where d is the film thickness and T is the transmittance.

In the low-energy region of the incident photon (1–2.75 eV), we see a decrease in the absorption coefficient. Considering the annealing temperature, we have found that the optical absorption coefficient increases when the temperature goes from 250 °C to 350 °C and then decreases for the temperatures 450 °C and 550°C.

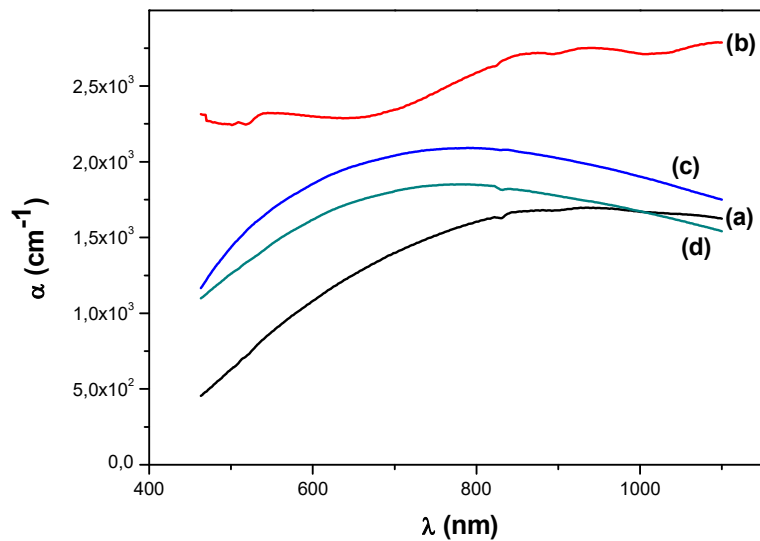


FIG. 7. Optical absorption coefficient *versus* wavelength for thin films obtained after annealing at 250°C (a), 350°C (b), 450°C (c) and 550°C (d), for 2 hours.

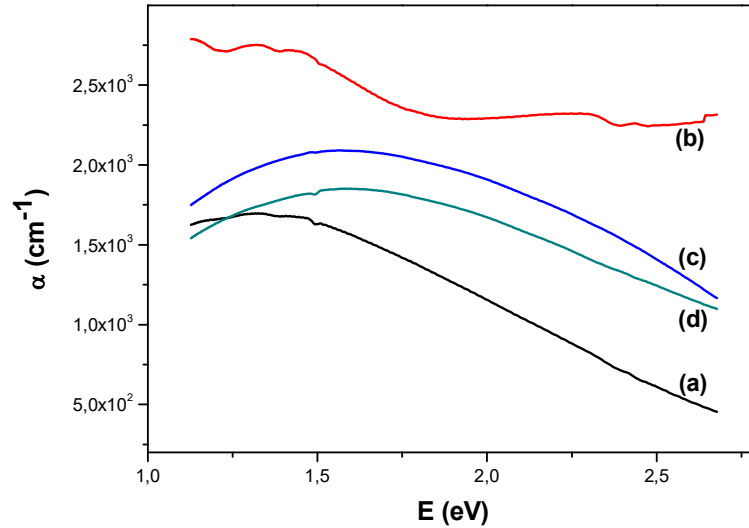


FIG. 8. Optical absorption coefficient *versus* photon energy for films after annealing at 250°C (a), 350°C (b), 450°C (c) and 550°C (d), for 2 hours.

The optical band gap energy of TiO₂ thin films annealed at 250°C and 550°C was calculated from the absorption spectra using the Tauc formula [23]:

$$(\alpha h\nu) = A(h\nu - E_g)^n, \quad (7)$$

where α is the absorption coefficient, $h\nu$ is the photon energy, A is a constant, E_g is the optical band gap and n is a number equal to 2 and 1/2 for indirect and direct allowed transition, respectively. Knowing that TiO₂ is an indirect gap material [24, 25], the optical band gap values are obtained by extrapolating the linear part of $(\alpha h\nu)^{1/2}$ curves to $\alpha=0$, as shown in Fig.9.

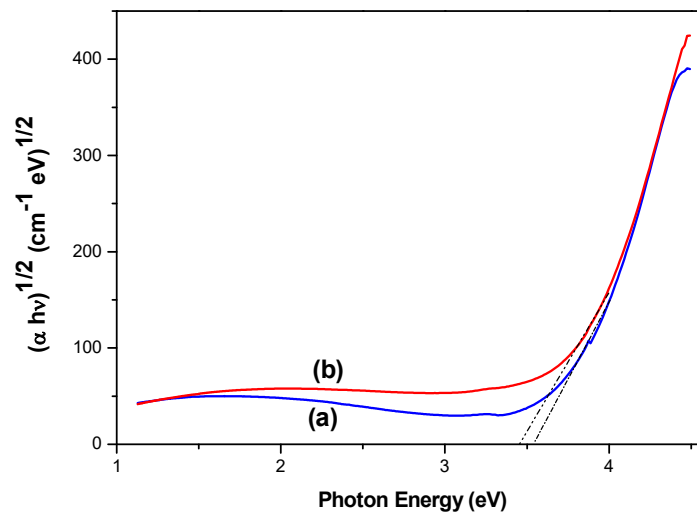


FIG. 9. Plots of $(\alpha h\nu)^{1/2}$ versus photon energy for thin films obtained after annealing at 250°C (a) and 550°C (b), for 2 hours.

The results of the optical analysis were interpreted in light of the crystalline properties deduced from the structural characterization of the different samples. The TiO₂ thin films with monoclinic β -TiO₂ and tetragonal anatase structures, obtained by annealing at 250 °C and 550 °C for 2 h, respectively showed better transmittance, Fig.6 and low absorption, Figs.7 and 8, compared to those of TiO₂ thin films having two phases resulting from annealing at

350 °C and 450 °C for 2 h. This leads to the conclusion that the optical absorption increases and the optical transmittance decreases, when the crystalline order is improved.

The obtained values of indirect optical band gap are 3.43 eV and 3.61 eV for thin films annealed at 250°C and 550°C, respectively. Certainly, the most cited value for anatase phase is 2.23 eV [21], but other works have obtained values comparable to ours [24, 25].

Conclusion

In this work, we have successfully prepared thin films of sputtered titanium using ion beam-assisted deposition (IBAD). The films were thermally oxidized and successfully annealed at temperatures of 250°C, 350°C, 450°C and 550°C. XRD spectra have shown that the film phase was modified from the monoclinic type to the tetragonal type by increasing the annealing temperature from 250 °C to 550 °C. Height

parameters deduced from roughness AFM analysis have noticeably increased as a result of thermal oxidation at higher temperatures. Optical measurements indicate high transmission films over the visible range and a wide optical energy gap in the range 2.43-3.61 eV.

Acknowledgements

The authors are grateful to Dr Ch. Bippes and Dr. R. Djaafar (Nanosurf AG, Switzerland) for the AFM visualization of our samples.

References

- [1] Martinu, L. and Poitras, D., *J. Vac. Sci. Technol. A*, 18 (2000) 2619.
- [2] Wang, Z., Helmersson, U. and Kall, P.O., *Thin Solid Films*, 405 (2002) 50.
- [3] O'Regan, B. and Grätzel, M., *Nature*, 353 (1991) 737.
- [4] Saveninije, T.J., Warman, J.M. and Goosens, A., *Chem. Phys. Lett.*, 287 (1998) 148.
- [5] Montesperelli, G. and Pumo, A., *Sens. Actuators B*, 24–25 (1995) 705.
- [6] Kingon, I., Maria, J.-P. and Streiffer, S.K., *Nature*, 406 (2000) 1032.
- [7] Borlaf, M., Colomer, M.T., Moreno, R. and Ortiz, A.L., *Journal of the European Ceramic Society*, 34 (2014) 4457.
- [8] Sen, S., Mahanty, S., Roy, S., Heintz, O., Bourgeois, S. and Chaumont, D., *Thin Solid Films*, 474 (2005) 245.
- [9] Tsai, S.J. and Cheng, S., *Catal. Today*, 33 (1997) 227.
- [10] Maruska, H.P. and Ghosh, A.K., *Sol. Energy*, 20 (1978) 443.
- [11] Tang, H., Prasad, K., Sanjines, R., Schmid, P.E. and Levy, F., *J. Appl. Phys.*, 75 (1994) 2042.
- [12] Guang-Lei, T., Hong-Bo, H. and Jian-Da, S., *Chin. Phys. Lett.*, 22 (2005) 1787.
- [13] Oh, S.H., Kim, D.J. and Hahn, S.H., *Mater. Lett.*, 57 (2003) 4151.
- [14] Kim, J.H., Lee, S. and Im, H.S., *Appl. Surf. Sci.*, 151 (1996) 6.
- [15] Campbell, S.A., Kim, H.S., Gilmer, D.C., He, B., Ma, T. and Gladfelter, W.L., *IBM J. Res. Dev.*, 43 (1999) 383.
- [16] Wang, Z., Helmersson, U. and Käll, P.O., *Thin Solid Films*, 405 (2002) 50.
- [17] Kaeble, E.F., “*Handbook of X-rays*”, Ed., (Mac Graw Hill, 1981).
- [18] Sherrer, P., *Göttinger Nachrichten*, 2 (1981) 98.
- [19] Warren, B.E., *J. Appl. Phys.*, 12 (1941) 3750.
- [20] Fallah, H.R., Ghasemi, M. and Hassanzadeh, A., *Physica E*, 39 (2007) 69.
- [21] Khan, A.F., Mehmood, M., Durrani, S.K., Ali, M.L. and Rahim, N.A., *Mater. Sci. in Semic. Process*, 29 (2015) 161.
- [22] Palik, E.D., “*Handbook of Optical Constants of Solids*”, Ed., (Academic Press, San Diego, 1998).
- [23] Tauc, J., “*Amorphous and Liquid Semiconductors*”, Ed., (Plenum Press, New York, 1974).
- [24] Wang, Z., Helmersson, U. and Kall, P.O., *Thin Solid Films*, 405 (2002) 50.
- [25] Sen, S., Mahanty, S., Roy, S., Heintz, O., Bourgeois, S. and Chaumont, D., *Thin Solid Films*, 474 (2005) 245.

Calculation of Darken Stability Functions of Al-In and Bi-Zn Binary Liquid Alloys

O. W. Abodunrin and A. A. Ajayi

Department of Mathematical and Physical Science, Afe Babalola University, Ekiti State, Nigeria.

Doi: <https://doi.org/10.47011/14.2.2>

Received on: 27/01/2020;

Accepted on: 29/07/2020

Abstract: The thermodynamic model based on clustering of two atoms is considered with the view to obtain the concentration-concentration fluctuation, $S_{cc}(0)$ and the darken stability function. The thermodynamic properties of these alloys were evaluated based on clustering of two atoms (A & B) or (B & A). Each system has the view of obtaining concentration-concentration fluctuation, $S_{cc}(0)$ enumerating the low-order atomic correlation in the nearest neighbour shell of liquid binary alloys. The highlights of reciprocals of $S_{cc}(0)$ of these alloys were noted. The values of $S_{cc}(0)$ for Al-In alloy throughout the entire concentration were positive and higher for activity ratio and lower than the ideal solution values for free energy of mixing at specific Al composition. The values of darken stability function of Al-In alloy fall below the ideal darken stability function for activity ratio and free energy of mixing. The indication of the reciprocal of $S_{cc}(0)$ for all the alloys is in support of homocoordination / heterocoordination in the nearest neighbour shell. The $S_{cc}(0)$ and darken stability function of Bi-Zn binary alloys were noted with fluctuations.

Keywords: Concentration-concentration fluctuation, Darken stability function, Ordering energy.

Introduction

This study focuses attention on an aspect where detailed information was not made available on the thermodynamic properties of binary liquid alloys [1]. Relevant properties include concentration-concentration fluctuation, $S_{cc}(0)$ and short-range order parameter, SRO [2]. The $S_{cc}(0)$ and SRO of some binary alloys were calculated without attaching the darken stability functions; i.e., $1/S_{cc}(0)$ [3]. The calculated experimental concentration-concentration fluctuation, $S_{cc}(0)$ using ordering energy from free energy of mixing and experimental activities of eleven binary alloys was computed without attaching their darken stability functions. For these properties, data was generated using inputs such as ordering energy

value, coordination number, melting temperature and Boltzmann constant. Thermodynamic expressions as functions of concentration from quasichemical model were employed in the described programs for generating data for these thermodynamic properties. The Al-In and Bi-Zn liquid alloys were selected based on the *fact* that the experimental number-number partial structural factor, $S_{NN}(0)$ concentration-concentration partial structural factor and $S_{cc}(q)$ were difficult to obtain from neutron diffraction experiment.

Therefore, the observation in this article focuses attention on the determination of ordering energy values of two binary liquid alloys from values of deviations in $S_{cc}(0)$ [3].

These ordering energy values were used in the calculation of $S_{cc}(0)$ and $1/S_{cc}(0)$ of the two binary liquid alloys. Similar method for generating values was followed by inscribing programs which involve using inputs from Table 1. The thermodynamic expressions made available by a quasichemical model which matches experimental observations for many alloys whose $S_{NN}(0)$ values are easily obtained

from neutron experiment were used. The quasichemical model has the capacity to accommodate higher-order atomic correlation forming the Four Atoms Cluster Model (FACM). This gives the advantage over other models.

The determined values of ordering energy are displayed in Table 1.

TABLE 1. Ordering energy (w) in eV of binary alloys.

Alloy	Temperature (°K)	Z	w_1 (eV)	w_2 (eV)	w_3 (eV)
Al-In	1338	10.0	0.0980	0.1127	0.1130
Bi-Zn	773	10.0	0.0210	0.0206	0.0206

Theory

The calculation of $S_{cc}(0)$ is often attracting attachment like $(S_{cc}(0))^{-1}$. This view provides additional facts that shed light on alloying behavior in terms of compound formation [4], self-coordination, phase segregation and complex concentration formation [5, 6]. Thermodynamically, the relationship between short-range order parameter, SRO, concentration-concentration fluctuation, $S_{cc}(0)$ and other thermodynamic properties had been cited in the literature [7-9]. Moreover, between G_m and $1/S_{cc}(0)$, it is given below. The following thermodynamic expressions are from the quasichemical model.

Quasichemical Expressions for Various Thermodynamic Functions

Free Energy of Mixing G_m ;

$$G_m = G_m^{id} + G_m^{xs} \quad (1)$$

$$G_m^{id} = RT\{c \ln c + (1-c) \ln(1-c)\} \quad (2)$$

$$G_m^{xs} = RT\{c \ln \gamma_A + (1-c) \ln \gamma_B\} \quad (3)$$

where G_m^{id} and G_m^{xs} are ideal and excess free energy of mixing. R is molar gas constant, T is temperature, c & $1-c$ represent the concentration of A and B atoms in the alloy, respectively. γ_A and γ_B are the activity coefficients and stand for:

$$\gamma_A = \left(\frac{\beta - 1 + 2c}{c(1 + \beta)} \right)^{\frac{z}{2}} \quad (4)$$

$$\gamma_B = \left(\frac{\beta + 1 - 2c}{(1-c)(1 + \beta)} \right)^{\frac{z}{2}} \quad (5)$$

$$\beta = (1 + 4c(1-c)(\eta^2 - 1))^{\frac{1}{2}}, \quad (6)$$

$$\text{where } \eta = \exp(w/zk_B T) \quad (7)$$

$$a_A = c \left(\frac{\beta - 1 + 2c}{c(1 + \beta)} \right)^{\frac{z}{2}} \quad (8)$$

$$a_B = (1-c) \left(\frac{\beta + 1 - 2c}{(1-c)(1 + \beta)} \right)^{\frac{z}{2}} \quad (9)$$

η and β are thermodynamic parameters which are interwoven.

The relationship between darken stability function, $1/S_{cc}(0)$ and free energy of mixing G_m is given as:

$$(S_{cc}(0))^{-1} = \frac{1}{Nk_B T} \left(\frac{\partial^2 G_m}{\partial c^2} \right)_{T,P,N} \quad (10)$$

Also, the relationship between activity (a_A or a_B) and darken stability function is given as:

$$(S_{cc}(0))^{-1} = \frac{1}{(1-c)a_A} \left(\frac{\partial a_A}{\partial c} \right)_{T,P,N} = \frac{1}{c a_B} \left(\frac{\partial a_B}{\partial (1-c)} \right)_{T,P,N} \quad (11)$$

From Eqs. (1), (2), (3) to (11), N is the total number of atoms in the alloy, k_B is the Boltzmann constant, T is the temperature, p is the pressure and Z is the coordination number of the alloys. The terms a_A and a_B in Eq. (11) represent the activities of atom A and atom B, respectively.

The expression for the ideal darken stability function is given by:

$$(S_{cc}^{id}(0))^{-1} = \frac{1}{c(1-c)} \quad (12)$$

$S_{cc}(0)1$, $1/S_{cc}(0)1$, $S_{cc}(0)2$ and $1/S_{cc}(0)2$ are from experimental activities, $S_{cc}(0)3$ and $1/S_{cc}(0)3$ are from experimental free energy of mixing.

Results and Discussion

In Fig. 1 and Table 2, it is observed that, in the range of compositions $0 < C_{Al} < 1.0$, the $S_{cc}(0)_{exp}$ obtained *via* each of the three methods indicates that the alloy is in perfect agreement. The values are greater and lower than the ideal values at $C_{Al} = 0.6$, which indicates homocoordination and heterocoordination, although in terms of magnitude, the results $S_{cc}(0)1$ and $S_{cc}(0)3$ are closer than $S_{cc}(0)2$. In

addition, at the composition $C_{Al} = 0.6$, the magnitude of $S_{cc}(0)1$ is the largest of the three. Hence, in the region $0 < C_{Al} < 1.0$, one can say that the usual Eqs. (10) and (11) give rise to the expected results in the Al-In liquid alloy. It is also observed from the Figure and the Table that the results from $S_{cc}(0)3$ appear to be more reliable than the results from $S_{cc}(0)1$ and $S_{cc}(0)2$.

In Fig. 2 and Table 2, it is observed that, in the range of composition $0.3 \leq C_{Al} \leq 0.7$, the $1/S_{cc}(0)_{exp}$ obtained *via* each of the three methods is in perfect agreement. In the region $0 \leq C_{Al} \leq 0.2$, $1/S_{cc}(0)1$ is closest to the ideal darken stability function ($1/S_{cc}(0)id$) and in the region $0.8 \leq C_{Al} \leq 1.0$, $1/S_{cc}(0)2$ is the closest to the ideal darken stability function.

TABLE 2. Calculated experimental concentration-concentration fluctuation and darken stability function of Al-In alloy. C_{Al} is the concentration of Aluminium in the alloy.

C_{Al}	$S_{cc}(0)1$	$S_{cc}(0)2$	$S_{cc}(0)3$	$S_{cc}(0)id$	$1/S_{cc}(0)1$	$1/S_{cc}(0)2$	$1/S_{cc}(0)3$	$1/S_{cc}(0)id$
0.0	0.000	0.000	0.000	0.00	0.0000	0.000	0.000	0.0000
0.1	0.150	0.204	0.162	0.09	6.667	4.901	6.172	11.1111
0.2	0.417	0.382	0.424	0.16	2.398	2.618	2.358	6.2500
0.3	0.997	1.035	0.974	0.21	1.003	0.966	1.027	4.7619
0.4	2.234	2.282	2.050	0.24	0.448	0.438	0.488	4.1667
0.5	5.864	5.239	8.053	0.25	0.171	0.191	0.124	4.0000
0.6	70.437	-128.993	-23.186	0.24	0.014	-0.008	-0.043	4.1667
0.7	6.775	5.922	3.550	0.21	0.148	0.169	0.282	4.7619
0.8	0.692	3.735	0.713	0.16	1.445	0.268	1.403	6.2500
0.9	0.237	0.189	0.289	0.09	4.219	5.291	3.460	11.1111
1.0	0.0000	0.000	0.000	0.00	0.000	0.0000	0.0000	0.0000

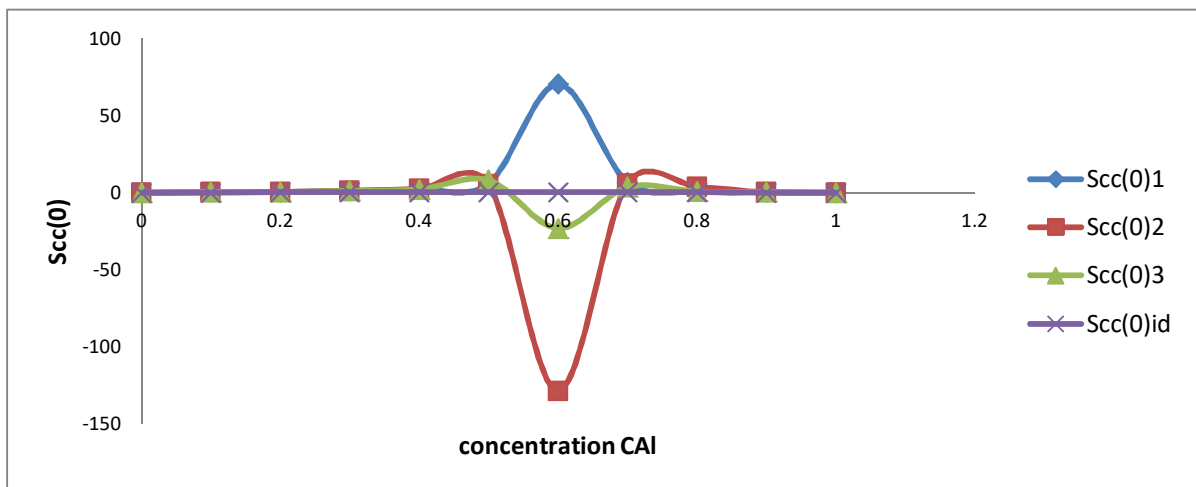


FIG. 1. Concentration-concentration fluctuation $S_{cc}(0)$ versus concentration C_{Al} .

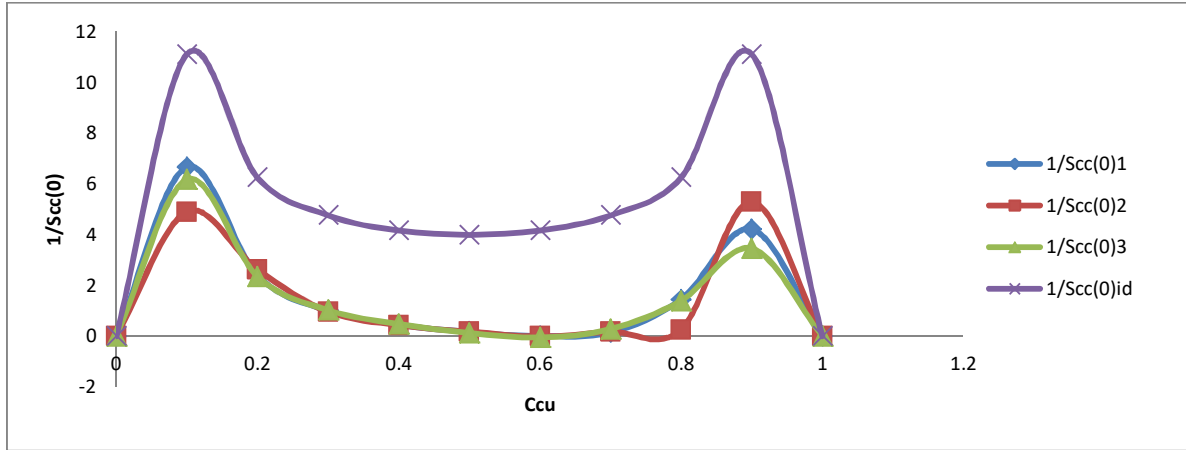


FIG. 2. Darken stability function *versus* concentration C_{Al} .

In Fig. 3 and Table 3 based on observation, in the range of composition $0.2 \leq C_{Bi} \leq 0.5$, the $Sc(0)_{exp}$ obtained *via* each of the three methods is not in perfect agreement and indicates that the alloy is homocoordinated and heterocoordinated, because its values are lower and greater than the ideal values, although in terms of magnitude, the results $Sc(0)2$ and $Sc(0)3$ are closer than $Sc(0)1$ in the range 0.4

$< C_{Bi} < 1.0$. In addition, at the composition $C_{Bi} = 0.2$, the magnitude of $Sc(0)1$ is the largest of the three. Hence in the region $0 < C_{Bi} < 1.0$, it is observed that the usual Eqs. (10) and (11) give rise to the expected results in the Bi-Zn liquid alloy. It is also observed from the Figure and the Table that the results from $Sc(0)2$ appear to be more reliable than the results from $Sc(0)1$ and $Sc(0)3$.

TABLE 3. Calculated experimental concentration-concentration fluctuation and darken stability function of Bi-Zn alloy. C_{Bi} is the concentration of bismuth in the alloy.

C_{Bi}	$Sc(0)1$	$Sc(0)2$	$Sc(0)3$	$Sc(0)id$	$1/Sc(0)1$	$1/Sc(0)2$	$1/Sc(0)3$	$1/Sc(0)id$
0.0	0.000	0.000	0.000	0.00	0.000	0.000	0.000	0.0000
0.1	0.837	0.442	8.315	0.09	1.195	2.262	0.120	11.1111
0.2	22.459	-5.384	-4.99	0.16	0.045	-0.171	-0.200	6.2500
0.3	2.593	1.935	1.894	0.21	0.386	0.513	0.528	4.7619
0.4	8.756	0.754	0.759	0.24	0.114	1.318	1.318	4.1667
0.5	0.482	0.503	0.513	0.25	2.075	1.988	1.949	4.0000
0.6	0.395	0.385	0.386	0.24	2.532	2.597	2.591	4.1667
0.7	0.301	0.292	0.281	0.21	3.322	3.559	3.559	4.7619
0.8	0.14	0.198	0.195	0.16	7.143	5.050	5.128	6.2500
0.9	0.133	0.099	0.135	0.09	7.519	10.101	7.4070	11.1111
1.0	0.000	0.000	0.000	0.00	0.000	0.000	0.000	0.0000

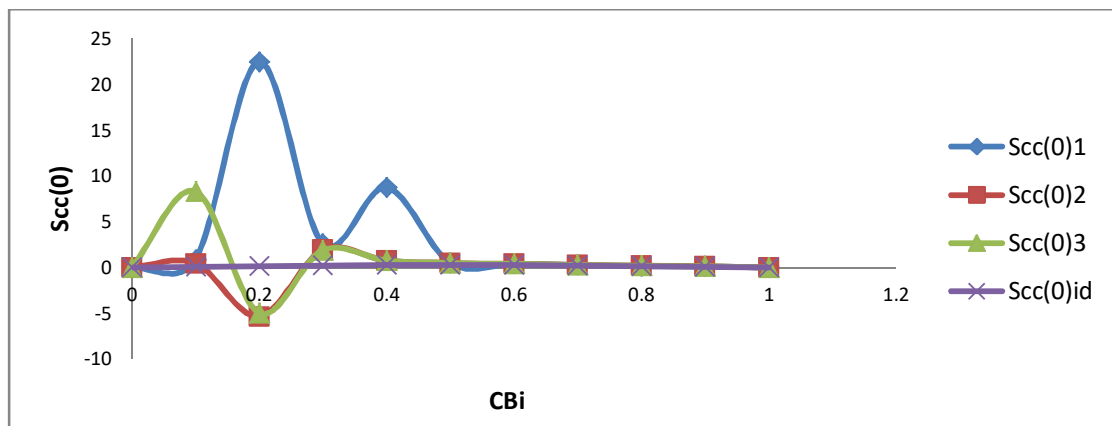


FIG. 3. Concentration-concentration fluctuation $Sc(0)$ *versus* concentration C_{Bi} .

In Fig. 4 and Table 3, in the range of composition $0 \leq C_{Bi} \leq 1.0$, the $1/\text{Sc}c(0)_{\text{exp}}$ obtained *via* each of the three methods is not in perfect agreement because of the regions $0.3 \leq C_{Bi} \leq 0.5$ and $0 \leq C_{Bi} \leq 0.2$. At $C_{Bi} = 0.1$, the

three approaches are below the ideal darken stability function. In the region At $C_{Bi} = 0.8$, only $1/\text{Sc}c(0)_1$ is above the darken stability function. At $C_{Bi} = 0.9$, only $1/\text{Sc}c(0)_2$ is close to the ideal darken stability function.

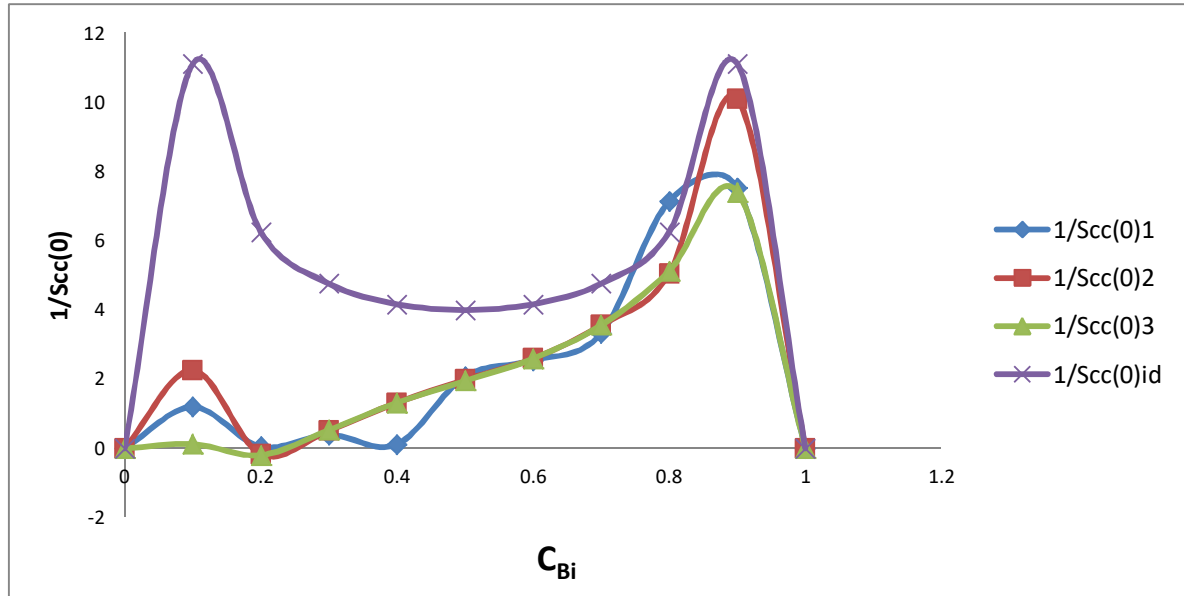


FIG. 4. Darken stability function *versus* concentration C_{Bi} .

Lastly, the darken stability functions for the three approaches are not in good agreement with the ideal darken stability function. This is in support of homocoordination and heterocoordination. The success of Eqs. (10) and (11) depends upon the true knowledge of the ordering energy w .

Concluding Remarks

This study has revealed, contrary to the belief that the $\text{Sc}c(0)_{\text{exp}}$ of liquid binary alloys can be computed *via* the experimental activities and experimental free energy of mixing using Eqs. (10) and (11) within a given set of data for experimental a_A , a_B and G_M from common source (as different sets of data for a system may not be

available, or if available may not necessarily agree throughout the entire composition) that:

- (1) There are no instance where the $\text{Sc}c(0)_{\text{exp}}$ obtained *via* each of the three methods agrees completely throughout the entire composition for the two alloys.
- (2) There is one instance where $\text{Sc}c(0)_{\text{exp}}$ obtained *via* each of the three methods has partial agreement instead of complete agreement (this is Al-In). The equality sign in Eqs. (10) and (11) is suggested to be an equivalence sign.

In conclusion, it is recommend that whenever $\text{Sc}c(0)_{\text{exp}}$ is needed, the common approach of obtaining it *via* experimental activity a_A should be seen as the best reliable method among the three.

References

- [1] Singh, R.N., Candian Journal of Physics, 65 (3) (1987) 309.
- [2] Bhatia, A.B. and Hargrove, W.H., Physical Review B, 10 (8) (1974) 3186.
- [3] Awe, O.E., Akinwale, I., Imeh, J. and Out, J., J. Phys. Chem. Liq., 48 (2) (2009) 243.
- [4] Chatterjee, S.K. and Prasad, L.C., Indian Journal of Pure and Applied Physics, 42 (2004) 283.
- [5] Lele, S. and Ramchandrarao, P., Metallurgical and Materials Transactions B, 12 (4) (1981) 659.
- [6] Adhikari, D., Singh, B.P, Jha, I.S. and Singh, B.K., Journal of Molecular Liquids, 156 (2-3) (2010) 115.
- [7] Singh, P., Physical Review B., 124 (3) (1984) 253.
- [8] Kotova, N., Golovata, N. and Usenko, N., Bulletin of Taras Shevchenko National University of Kyiv. Chemistry, 1 (55) (2018) 46.
- [9] Khanna, K.N. and Singh, P., Phys. Status Solidi. B, 122 (3) (1987) 233.

Multifactor Authentication Car Tracking System Using Fingerprint Verification

Ndianabasi. H. Valentine^a, Ogri J. Ushie^b and Emmanuel I. Akaerue^a

^a Department of Physics, University of Calabar, Nigeria.

^b Department of Electrical and Electronic Engineering, University of Calabar, Nigeria.

Doi: <https://doi.org/10.47011/14.2.3>

Received on: 14/02/2020;

Accepted on: 26/07/2020

Abstract: The design of an intelligent system used to detect and locate vehicle theft has become a viable and sustainable tool in the security system globally. Multifactor authentication car tracking system works in a way that if an unauthorized person tries to steal the vehicle, the user and user's relatives and a registered police station will be notified with the GPS location. The fingerprint records are stored in the memory of the system. When the fingerprint matches with the stored ones, the microcontroller triggers and powers the circuit. The GPS module gets the location information from satellites in the form of location coordinates. The GSM module sends a short message service immediately to notify the owner in case of any theft action. The fingerprint test-scan results of approximately 100 percent competency level demonstrate that this technology has an enormous potential to enhance effective security and tracking technology in vehicles, objects and humans.

Keywords: Tracking system, GPS, Fingerprint, Module.

PACS: Electronic, 07.50.EK, 84.30.-r.

Introduction

Global positioning system (GPS) trackers are portable devices that allow fleet managers, parents and vehicle owners of all kinds to monitor and track their cars and trucks. Real-time GPS trackers for cars are capable of providing instantaneous speed and location data, while less expensive options record this type of information for later use. With some GPS vehicle trackers, it is even possible to set up real-time alerts to go off whenever a driver speeds or deviates from a specific area.

The world population increase has led to a proportional increase in the demand of vehicles as a necessity of life in recent times. Improvement in science and technology has brought significant advancement in security measures to curb the menace of theft activities in

vehicles. Car jackers have also developed higher techniques to bridge these measures; hence, a system with fingerprint innovation and tracking mechanism is needed to replace the existing vehicles' security structures. Vehicle Tracking Systems are important security measures that should be considered for ensuring life and vehicles, since they are equipped to keep the user informed about the vehicle's location through a telecommunication system [1-4].

The present work is focused on more secure tracking means for automobiles. The vehicles equipped with this device need to recognize the user's fingerprint before the engine is ignited. A limitation on the number of users is set, which makes the automobile more secure. Alongside, the device improves the security operation of

vehicles, measures the impact level of recent developed fingerprint engine starter systems and automobile starters and evaluates the unique difference of the acceptability level of the systems. Recently, fingerprint identification is one of the most important biometric technologies which have drawn an extensive amount of attention. The uniqueness of a fingerprint makes it acceptable and easy in modern-day technologies. Fingerprint biometrics provides a reliable, robust and full-proof personal identification. Fingerprint biometrics is one of the efficient, secure, cost-effective and easy to use technologies for user authentication [5-7]. Fingerprint authentication, like other biometric methods, requires the physical presence of the person to be identified. It potentially prevents unauthorized admittance to access control systems or fraudulent use of ATMs, Time and Attendance Systems, cellular phones, smart cards, desktop PCs, workstations, vehicles and computer networks. Biometric recognition systems offer greater security and convenience than traditional methods of personal recognition [8-13].

Research Methodology

The fingerprint Verification technology describes a high-security car tracking system with multi-factor authentication method using knowledge factor (password) through keypad, combined with an inherence factor (biometric) using fingerprint, which makes it more secure than the existing ones [6, 9-12]. The system features are: fingerprint module, GPS module, GSM module and 433MHz Ultra High Frequency (UHF), Radio Frequency (RF) transmitter and receiver modules, which are used for keyless access and control of the car. An output on the receiver is used to activate or deactivate the car in an event of car hijack.

The presented multifactor authentication car tracking system was designated and constructed

into two sections: the transmitter section and the receiver section. The block diagrams of these sections are depicted in Fig. 1 and Fig. 2, respectively. The transmitter has a 4x3 matrix keypad and an acknowledge LED that briefly lights up each time one of the switches in the transmitter is pressed. Up to 16 separate transmitters can be used with one receiver in this design. The receiver on the other end combines the power of fingerprint, GPS and GSM module to add an extra security layer to the design.

Software is the key approach to this system; basically, three types of software were adopted for this design. These include Dip Trace which is a schematic capture program used in the designing of the schematic diagram, Proteus which is a simulation package used in the simulation of the finished design and Atmel Studio which is an Integrated Development Environment (IDE) used in the writing and compilation of the needed program for the work. In the design, a microcontroller was used to accomplish the task of monitoring and controlling of the system instead of a handful of digital integrated circuits (ICs) and other hardware to keep the component count low while maximizing the number of ways in which the design can be matched to real-life requirements. Adopting this approach gives room for the addition of new features and advancing functionality. This approach also makes the implementation far easier. The method used in the design is unique, due to the fact that wireless technology involves the combination of GPS, GSM and RF wireless transmitter and receiver modules. The hard-ware parts are combined with the power of software to archive the entire work, with the software being the key driving power. Using this method allows certain new features to be implemented easily through the configuration of the software instead of changing the hardware.

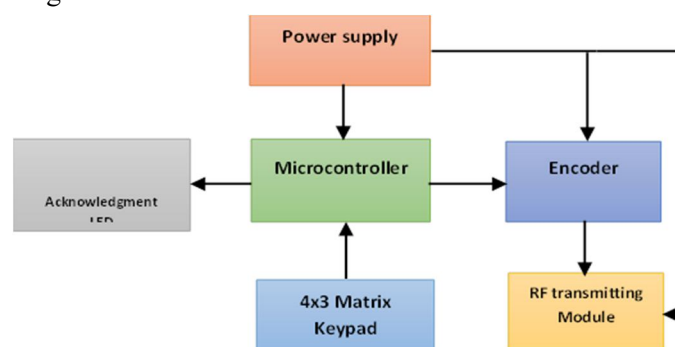


FIG. 1. Block diagram of transmitter section.

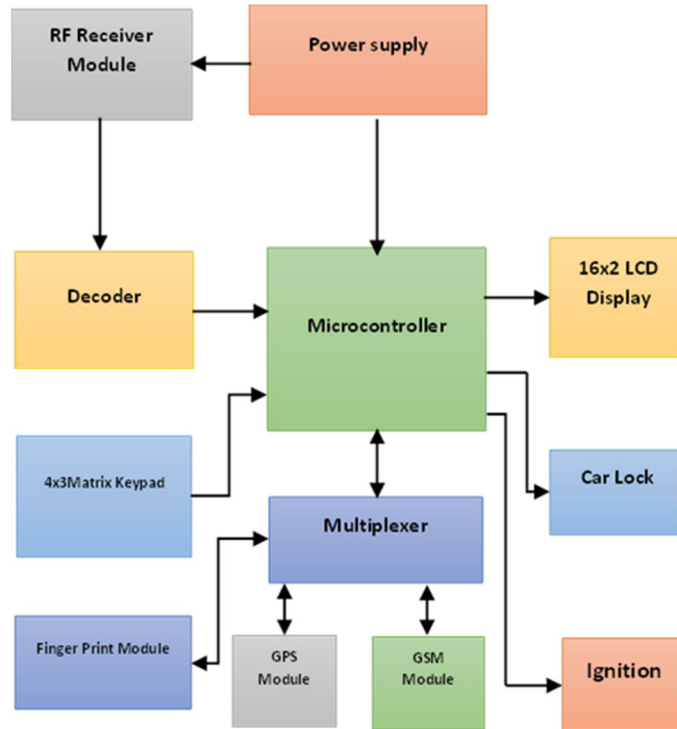


FIG. 2. Block diagram of receiver section.

The core of the tracking system is based on ATmega16 microcontroller, the responsibility of which is to monitor and manage the tracker. In the transmitter, the controller receives data from the keypad and transmits the received data *via* 433MHz transmitting module *via* HT12E encoder integrated circuit. In the receiver, the controller receives the transmitted data *via*

HT12D decoder integrated circuit and initializes the system to begin operation. The signal received from the fingerprint module is also sent to the microcontroller for processing. The circuit diagrams of the transmitter and the receiver sections are shown in Fig. 3 and Fig. 4, respectively.

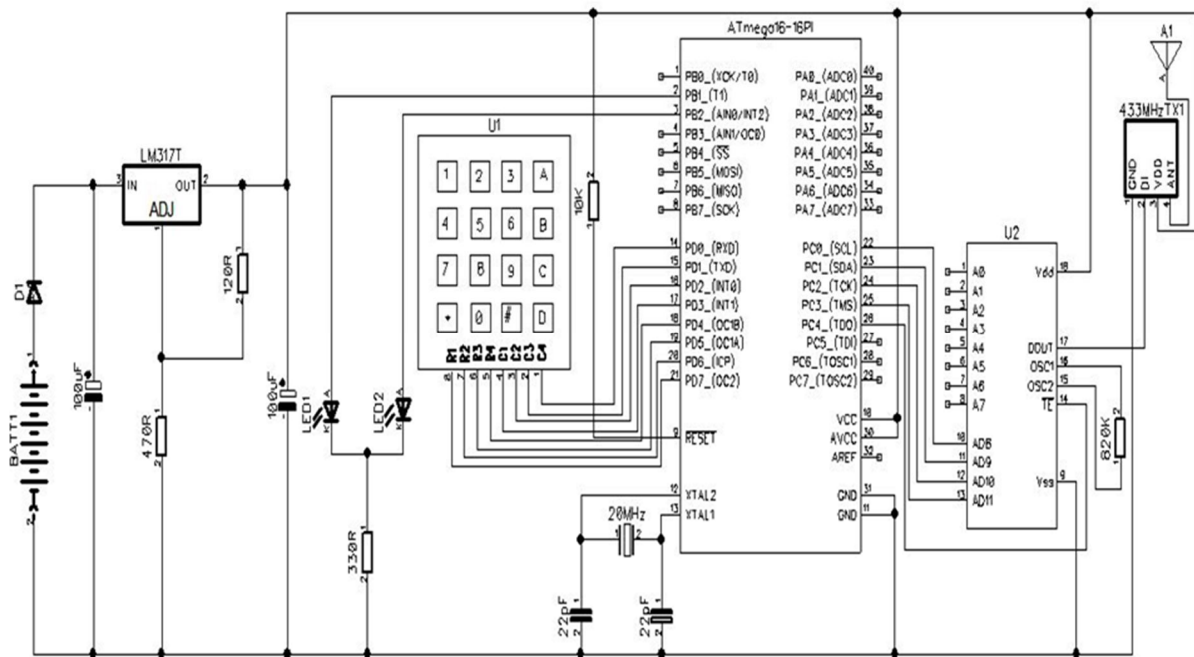


FIG. 3. Circuit diagram of transmitter section.

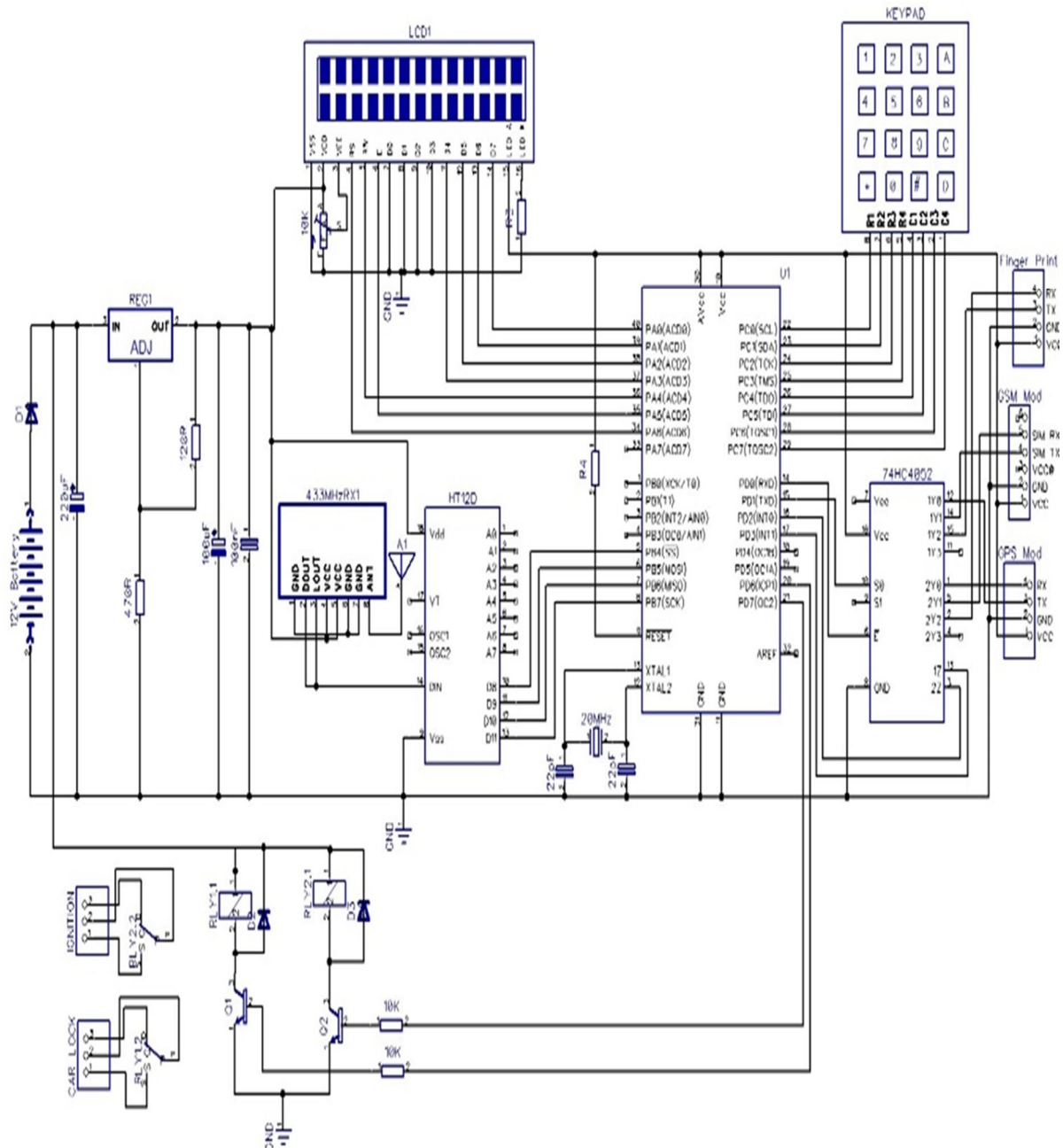


FIG. 4. Circuit diagram of receiver section of multifactor authentication car tracking system.

Stage-by-stage Breakdown of the System

The entire car tracking system is made up of seven major units as follows:

- (i) Power supply unit
- (ii) Receiver and decoder/remote control unit
- (iii) Microcontroller/data processing unit
- (iv) Authentication unit/data acquisition and management
- (v) LCD display unit
- (vi) Switching unit
- (vii) Communication unit/GPS and GSM modules.

The power supply unit is the general supply that supplies power to the entire system. Power for the circuit is derived from the car's 12V battery. The DC output from the car battery is fed to a positive adjustable voltage regulator type LM317 the responsibility of which is to supply constant +5V DC from +12VDC car battery for the microcontroller, RF transmitter and receiver modules, GSM, GPS, fingerprint module and LCD display, as shown in Fig. 5. The capacitors are responsible for decoupling the power supply line from ripple [14].

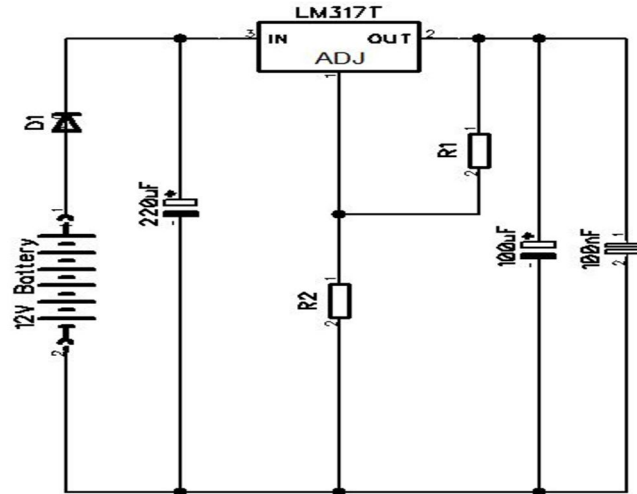


FIG. 5. Power supply unit of the car tracking system.

Receiver and decoder (remote control unit): This unit consists of a 433MHz Radio Frequency (RF) receiver and a decoder, with the function to receive the transmitted data that is sent from the transmitter and decode it back into binary data, before sending it to the microcontroller for processing. During operation, the decoder

decodes back the signal from the data in pin (DIN) into binary information (digital information) and then sends the information that it decodes to the microcontroller. The circuit diagram of the receiver and decoder section is shown in Fig. 6 [15].

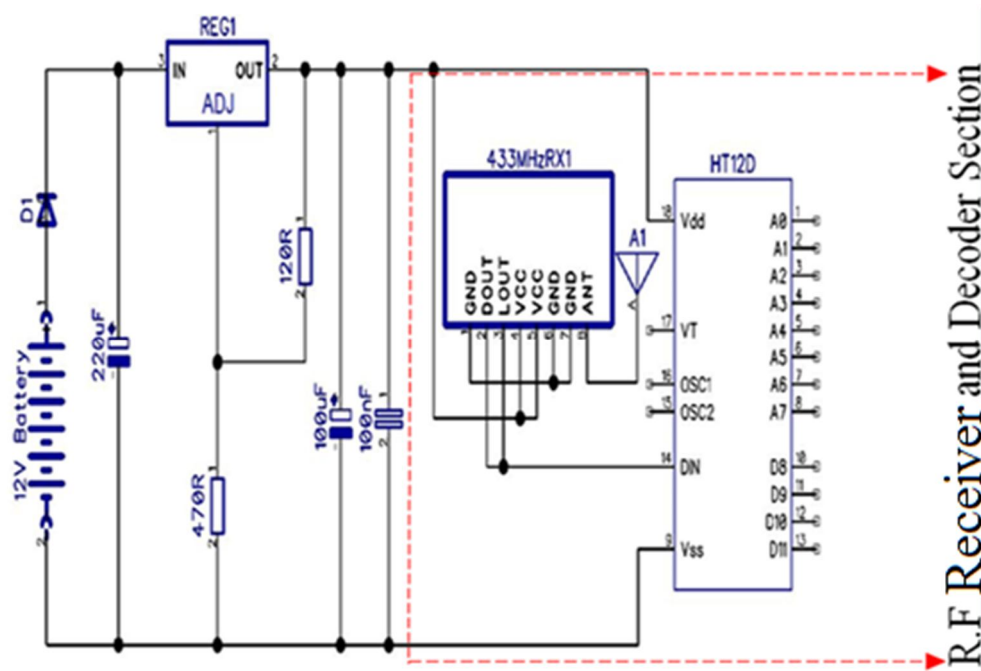


FIG. 6. Circuit diagram of the receiver and decoder section.

Microcontroller (data processing unit): This unit consists of an ATmega16 microcontroller, crystal oscillator and its loading capacitors. In spite of the seemingly complex operation of the work, the circuit itself is really very simple. Most of the intelligence is done by the microcontroller through a firmware program hidden inside the controller, which is really the heart of the circuit shown in Fig. 7. The

microcontroller runs at 20MHz using a crystal oscillator as its time base. In operation, the microcontroller monitors and manages every data and the signal that is coming from input devices (GPS, GSM, fingerprint module, RF transmitter and receiver modules) at the designated ports of the microcontroller, respectively [16].

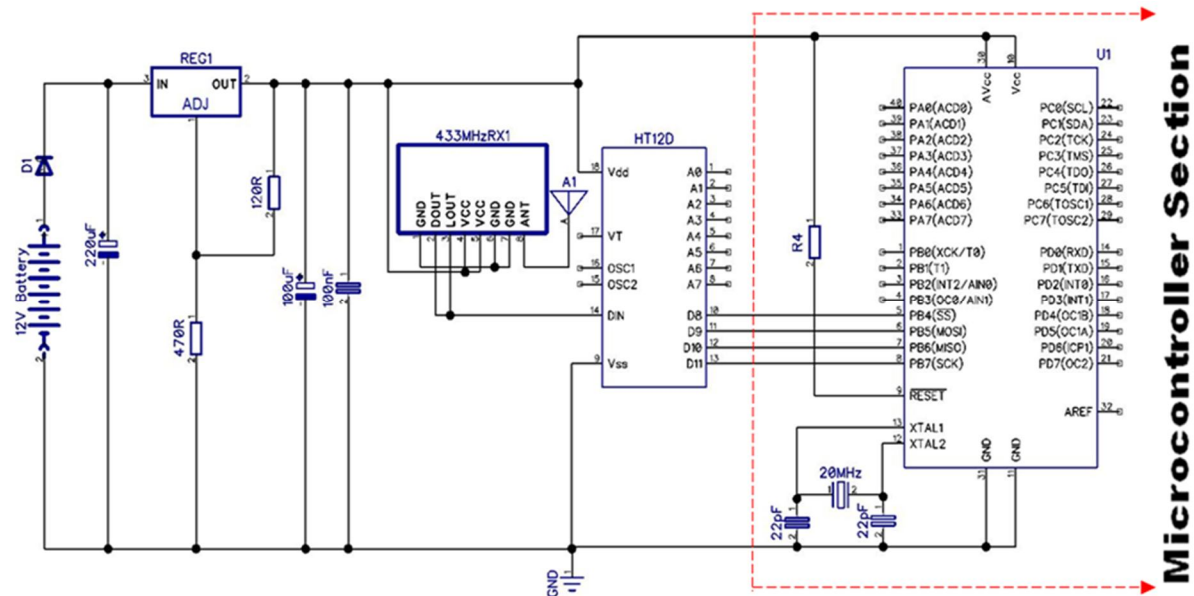


FIG. 7. Circuit diagram of the microcontroller section.

Authentication unit (data acquisition and management): Shown in Fig. 8, this unit is comprised of the keypad, fingerprint, GPS, GSM module and multiplexer. The functions of these modules are to receive and send data to the microcontroller for processing. When there is a

change in any of these input devices, it causes a change in the designated ports of the microcontroller to which they are connected and the controller in turn reads and interprets these values before executing the action in which it is being programmed to do [17].

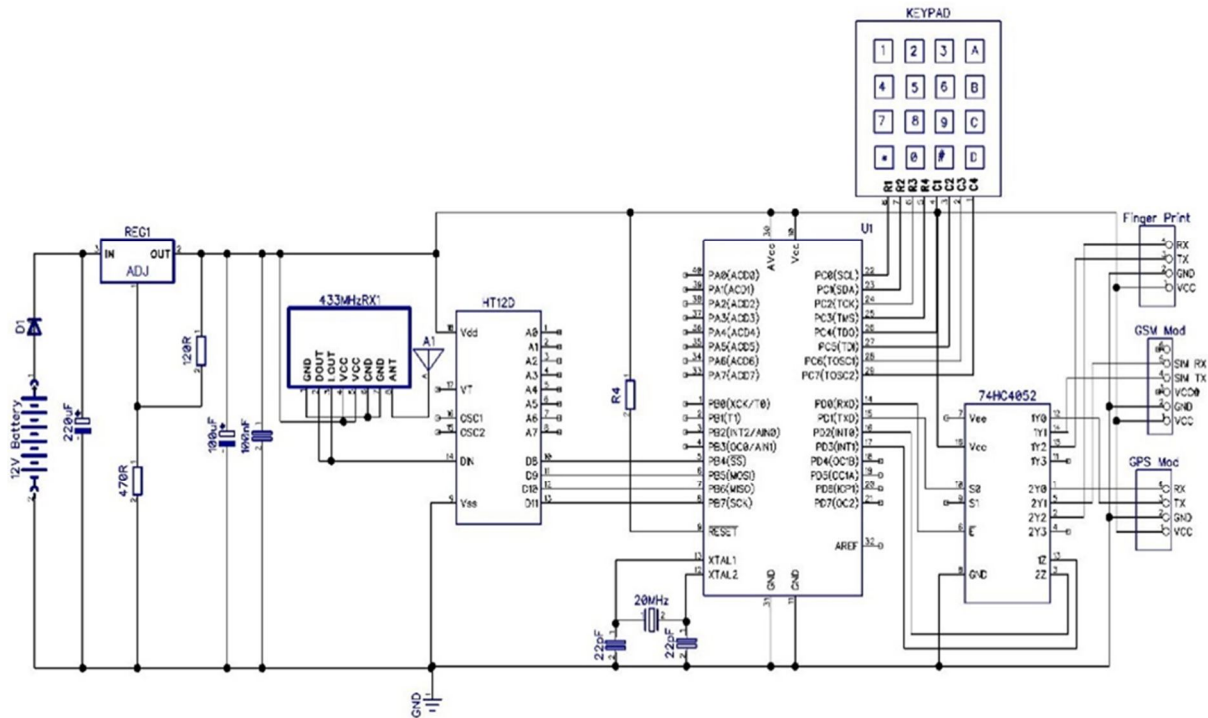


FIG. 8. Schematic diagram of the car tracking system with authentication unit.

The liquid crystal display (LCD) unit: It is a collection of a variable resistor and a current-limiting resistor for the LCD backlight. The display unit uses a standard 16-character by 2-line display wired in 4-bit mode to display the functionality, condition and status of the car

tracking system performance, as shown in Fig. 9. The displayed data is processed by the microcontroller before being sent to the display unit for display. The display data enables the user to know the status of the system [18].

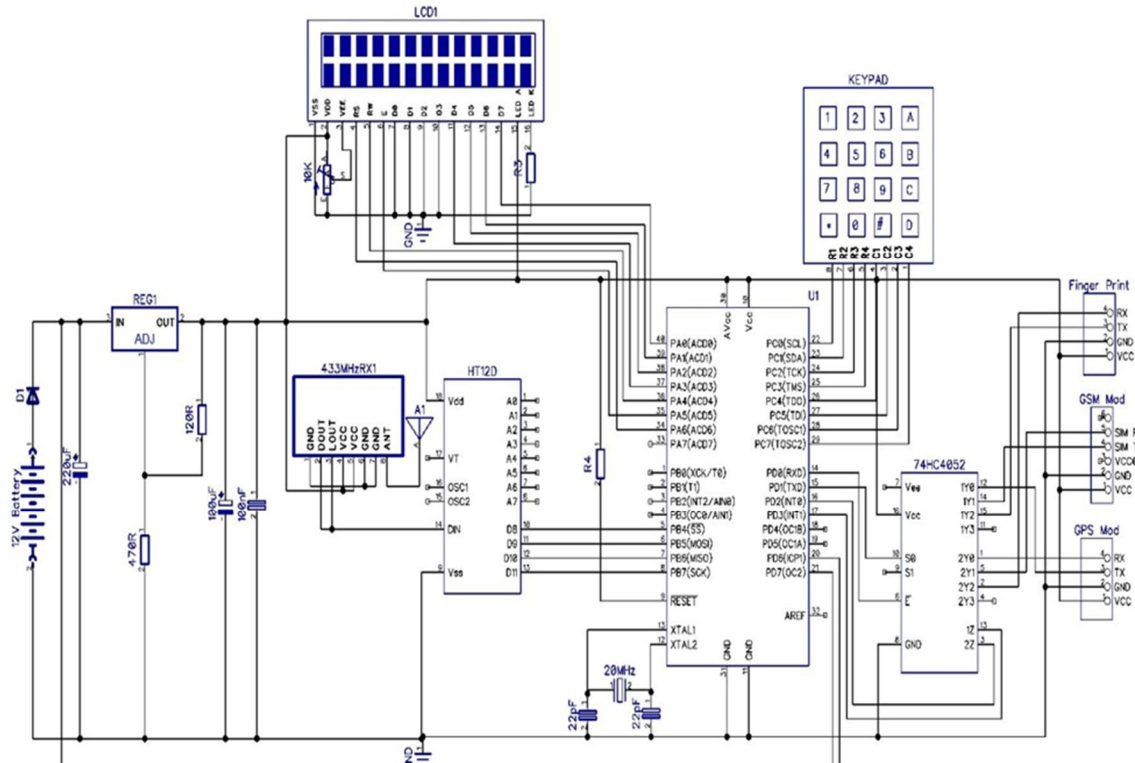


FIG. 9. Schematic diagram of the car tracking system with the display unit.

The switching and activation unit: It is saddled with the responsibility of engaging and disengaging the car when there is a change in the data received by the microcontroller through the respective input devices (keypad, fingerprint module, GPS and GSM modules). This section,

as shown in Fig. 10, is comprised of two transistors, two relays and diodes the function of which is to protect the transistors from getting damaged when there are occurrences of back Electromotive Force (EMF) during the operation of the system [19].

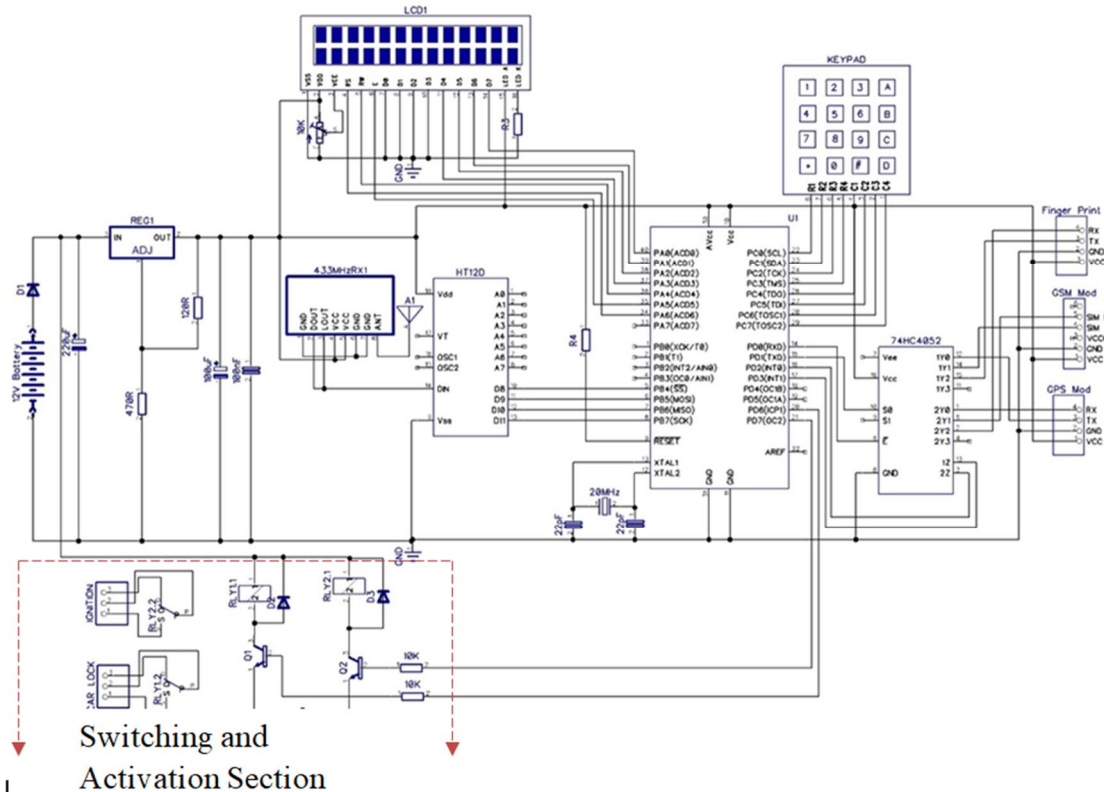


FIG. 10. The switching and activation unit of the car tracking system.

Communication unit /GPS and GSM module: GPS contains a serial port interface with the microcontroller. It receives and sends location data to the microcontroller and the microcontroller receives the data and transmits it to the user using GSM.

GSM module is interconnected with the microcontroller. The receiver pin of the microcontroller is wired with the transmitter pin of GSM modem and the transmitter pin of the microcontroller is wired with the receiver pin of GSM modem. The module uses the attenuation commands to select the mode in transferring and receiving messages and other functions, like calls, ... etc. It also uses time division multiple access technology. GSM/GPRS modem used in this work is SIM800 which is interfaced to the system to track and keep the coordinates of the car as well as sending an SMS text message to the user when unauthorized persons get access to the car. With the GSM and GPS modules, the user can track and control the car remotely. The modem also communicates and sends a text message to a dedicated security phone numbers when a wrong code or invalid fingerprint is detected in the system as well as the location (latitude and longitude) of the vehicle.

Results

The technique of this system is to use scan cues to determine the changes of the state of the phase voltage value. The difference in phase voltage instructs the microcontroller to switch to activate the lock and ignition switching system. When the system is switched on, it checks to get

the current status of the user in terms of fingerprint pattern; during this period, if this does not match the one stored in the system data EEPROM, the microcontroller takes over and activates the lock disengaging the ignition system of the car and then sends an SMS to the car owner notifying him/her of possible car theft with the location of the car. This system covers all the theoretical and practical areas specified for this research work. It helps in providing additional security measures by demanding the vehicle owner's fingerprint after a three minutes' drive, after three failed attempts by the system to recognize the fingerprint of the user. The steps below discuss the results of the system and its working conditions.

Step I. Access to the car using a handheld transmitting device (first-level authentication)

This is the separate unit of this research work and can also be called a handheld device. The test for this was first used to activate the car by inputting the 4-digit admin password (0124) in order to activate the vehicle; the red LED blinks at each input and a verification of the inputted pin saved in its EEPROM will be activated. If correct, it will send an RF signal to the car which in turn activates the car door in order to allow the user's access to the car. In the event of correct password entered by the user, the car doors unlock for the user to gain access to the car and a display (WELCOME CAR HAS BEEN ACTIVATED) appears, as shown in Fig. 11.



FIG. 11. Result for inputting the correct password combination.

Step II. Access to the car ignition system (second-level authentication)

However, the second-level authentication is carried out while the user is in the car and demands the fingerprint verification before the ignition is activated. The system demands that the right thumb of the user's finger be placed in the fingerprint module so as to authenticate the fingerprint recognized by the system. This is displayed in Fig. 12, as (SCANNING FP., PLS. PUT YOUR THUMB). Fig. 13 is an indication that the fingerprint module is carrying out a

verification process to ascertain that the finger placed in the fingerprint module is recognized by the system and the scanning process is completed. Then, the system will display the recognized fingerprint code with a predetermined identification number, ID NO: 000. Then, the system instructs the microcontroller to switch on the relay to activate the ignition switching system of the car for the user to start the car with the key. Fig. 14 shows that the finger placed in the fingerprint module is not recognized by the system.



FIG. 12. Result requesting to put the user's finger.



FIG. 13. Result showing scanning the correct finger.



FIG. 14. Result showing scanning a wrong finger.

Step III. Verifying that the car is not used by an intruder (third-level authentication)

In order to verify this level of authentication, a test was carried out on a car while on motion. The system demands the fingerprint within a 3-5 minutes' drive to ascertain the authenticity of the user for three times. After three failed attempts by the system to recognize the fingerprint while the car is still on motion, it demands for the thumb to be placed once again in the fingerprint module. This is an additional security measure to ensure that the car is driven by the owner whose fingerprint was verified and recognized by the fingerprint module in the system.

Step IV. Communication/ Tracking

This process shows a pop-up message as shown in Fig. 15 by sending a responder message to the car owner, relative and security agency's cell phone number as predefined in the system for tracking. On the receipt of this message, as shown in Fig. 16, the owner or either of the predefined phone numbers recognized by the system can now forward a programmed code message "@STOP" to the system to track the car by disengaging the car ignition system, thus confining the intruder inside the car by initiating the central lock system. Then, the system will automatically send the location and the coordinates of the car through GPS/GSM via S.M.S. for recovery.



FIG. 15. Result showing SMS sent to the designated mobile phone.



FIG. 16. Result showing an alert message sent to the user’s mobile phone.

Step V. Fingerprint authentication/ evaluation

For an extra authentication, fingerprint module is interfaced with the system in order to grant access to the user when required. When the fingerprint is inputted, the system then registers the fingerprint pattern and then prompts the user to start the car. After the verification of the fingerprint pattern, the microcontroller receives

the control command and energizes the ignition relay. Table 1 demonstrates the fingerprints test-scan of correct thumbs and wrong thumbs of users. The reliability test, as shown in Table 1, is a clear indication that the proposed system is a high-security car tracking system with approximately 100 percent competency level.

TABLE 1. Fingerprint test result and evaluation

S/No.	Input	Output (Result)	No. of Times Tested
1	Correct fingerprint identification	Image found with ID No: 000	12
2	Wrong fingerprint rejection	Image not found in the database	12
3	Correct fingerprint rejection	None	8
4	Wrong fingerprint acceptance	None	8

Conclusion

The main aim of this research work had been accomplished as described in the technical description of this work. It is satisfactory to say that there are several methods in which one can design a tracking system with intelligent security features that can be used in both domestic and industrial applications. With the above proposed type of system, the cost of paying insurance companies to manage and insure cars would be eliminated. The design specifications were established from an examination of related work

and the demand for tracking system applications. These criteria were critical in creating a work that met with the original objectives. Thus, having constructed a device that successfully met these specifications calls for future improvements in the area of other device compatibility as needed, as well as security camera integration. Miniaturization of the system is also recommended for future enhancement in the field of tracking technology.

References

[1] Kodavati, B. and Raju, V.K., IJERA, 3 (1) (2012) 616.
 [2] Yang, D.K., Cai, B.G. and Yuan, Y.F., IEEE Symposium on Intelligent Transportation Systems, 2 (2003) 1246.
 [3] Joshi, R.R., Proceedings, IEEE on Intelligent Vehicle Symposium, (2002) 36.
 [4] Deepika, V., Suneel, M., Chiranjeevi, M., Satya, V. and Swamy, T., IJACSCC, (2013).
 [5] Win, Z.M. and Sein, M., SICE Annual Conference, Waseda University, Tokyo, Japan, (2011) 13.
 [6] Saraswat, C., IJCSE, 2 (2) (2010) 264.
 [7] Rishabh, M. and Prashant, T., Thesis: National Institute of Technology Rourkela, Orissa-India, (2011), (Published).
 [8] Adeoye, T.O., JWCSIT, 4 (6) (2014) 76.

- [9] Ushie, O.J., Valentine, N.H., Ekong, I.B., Etido, M.G. and Bassey, J.U., JAET, 9 (2) (2019) 30.
- [10] Ahmed, A.E. and Mohammed, K., Open Comput. Sci., 10 (2020) 17.
- [11] Asmita, S.U. and Sankpal, S.S., IJITEE, 8 (10) (2019) 65.
- [12] Mounika, A. and Chepuru, A., IJRTE, 8 (2) (2019) 2399.
- [13] Power Supply Units: [https://en.wikipedia.org/wiki/Power_supply_unit_\(computer\)](https://en.wikipedia.org/wiki/Power_supply_unit_(computer)) [Accessed 31 January 2020].
- [14] Wireless transmitter and receiver RF modules: <https://www.electronicshub.org/wireless-transmitter-and-receiver-using-rf-module>. Retrieved 30th January 2020.
- [15] Darko, H. and Bojan, G.A., Sensors, 14 (6) (2014) 9755.
- [16] Naveen, K.V., Sujana, T., Likith, S.D. and Ramesh, C.G., IJSR, 4 (8) (2013) 419.
- [17] Liquid Crystal Display Device: https://en.wikipedia.org/wiki/Liquid_crystal_display. [Retrieved 30th, January, 2020].
- [18] Pressman, A.I., Billings, K. and Morey, T., "Switching Power Supply Design", 3rd edn., (McGraw-Hill, ISBN 0-07-148272-5p, 2009).
- [19] Aliyu, S., Abdullahi, U., Pomam, M., Hafiz, M., Sanusi, A. and Akanmu, S., 3rd Intern. Eng. Conf., Federal University of Technology, Minna, Nigeria, (2019).

Spatial and Temporal Variation of Clearness Index in Iraq

Waleed I. Al-Rijabo^a, Rajaa A. Basheer^b and Amal M. Banoosh^b

^a College of Education of Pure Science, Mosul University, Mosul, Iraq.

^b College of Education, Al-Hamdaniya University, Al-Hamdaniya, Iraq.

Doi: <https://doi.org/10.47011/14.2.4>

Received on: 01/03/2020;

Accepted on: 11/06/2020

Abstract: This study deals with the spatial and temporal variation of clearness index (KT) in different meteorological stations, well distributed in Iraq, during the period between 1995 and 2015. The results indicate that the clearness index varies with the geographical location and period of the year. Monthly values of clearness index (KT) in the months of January and December show the lowest values of the index ranging between 0.38 and 0.64. Meanwhile, August shows the highest values ranging between 0.53 and 0.71. Seasonal variation of KT is well noted. The range of (0.40 to 0.58) has been measured in winter, while the range of (0.53 to 0.70) has been detected in summer season. The annual variation of KT shows a range between (0.47 - 0.64) in all stations. The standard deviation (SD) of the monthly values of KT ranged between (0.01-0.06) for all stations, while the coefficient of variation (CV) for the monthly values of KT ranged between (2-10) percent.

Keywords: Clearness index, Global solar radiation, Extraterrestrial radiation, Time series, CV, SD.

Introduction

Clearness index (KT) is defined as the ratio of global solar radiation at ground level on a horizontal surface (H) to the extraterrestrial global solar radiation (H_0) [1].

In other words, KT is a measurement of the extinction of solar radiation due to the atmospheric events; i.e., the interaction of radiation with the clouds, air pollution and other atmospheric constituents [2, 3].

- * Low clearness index means low global radiation which usually attributes to a cloudy sky with a high portion of diffuse components.
- * High values of clearness index mean high global radiation, which is dominated by direct component [4, 5].

The following are the standard values of KT due to the daily clearness index in comparison to partition day of the type (clear, partially cloudy and cloudy), as has been taken from [6].

Clear day: $KT > 0.65$; partially cloudy day $0.35 < KT < 0.65$ cloudy day: $KT < 0.35$.

KT is really an important parameter in designing a renewable-energy source system; it can provide information concerning the real solar radiation in comparison with the available solar radiation [7].

Clearness index reflects both of the meteorological variation and climatic change in the troposphere depending on the location [8].

Evaluation of clearness index requires some astronomic calculations at the top of the troposphere, which take the time of the year into account [9].

Clearness index is affected by air pollution in both urban and rural areas. Therefore, it may serve as an indicator of air quality and air pollution by fine particles, particularly for upper atmospheric layers such as the stratosphere [10].

Over industrial and densely inhabited areas, the atmospheric pollution is greater than elsewhere, because the presence of aerosol particles and other pollutant materials in these areas is intense [11].

Large variation in KT occurs at both the temporal and the spatial scale. The regional features of KT and the effects of the atmospheric parameters on KT have not been sufficiently investigated, whereas the complex interactions of clouds, aerosols and pollutants occur throughout the year [12].

Material Methods

The mean monthly values of total global solar radiation were obtained from Iraqi

meteorological stations from 1995 until 2015 using 18 stations well distributed in Iraq. The missing data of the total solar radiation in some stations was estimated by means of using Glover model with local parameter [13].

The model:

$$H = H_0 [- 0.35 + 0.66 \cos (\Phi) + 0.46 \left(\frac{n}{N}\right)]$$

where Φ represents the latitude in (rad) and $\left(\frac{n}{N}\right)$ means the sunshine ratio.

Table 1 shows the geographical coordinators of the different stations and Fig. 1 shows the location of the different stations in Iraq.

TABLE 1. Geographical coordinators of the different stations.

Station	Latitude	Longitude	Altitude (m)	Station	Latitude	Longitude	Altitude (m)
Zakho	37.13°	42.68°	433	Rutba	33.03°	40.61°	631
Mosul	36.32°	43.15°	223	Kut	32.42°	44.75°	19
Sinjar	36.32°	41.83°	465	Nukhaib	32.03°	42.25°	305
Erbil	36.18°	44.00°	420	Karbala	32.62°	44.01°	29
Sulaimaniya	35.55°	45.41°	883	Amara	31.83°	47.16°	9
Kirkuk	35.47°	44.40°	331	Samawa	31.30°	45.31°	11
Baiji	34.60°	43.48°	115	Nasiriyah	31.08°	46.23°	3
Anna	34.47°	41.95°	139	Salman	30.50°	44.53°	220
Baghdad	33.30°	44.23°	32	Basra	30.52°	47.61°	2

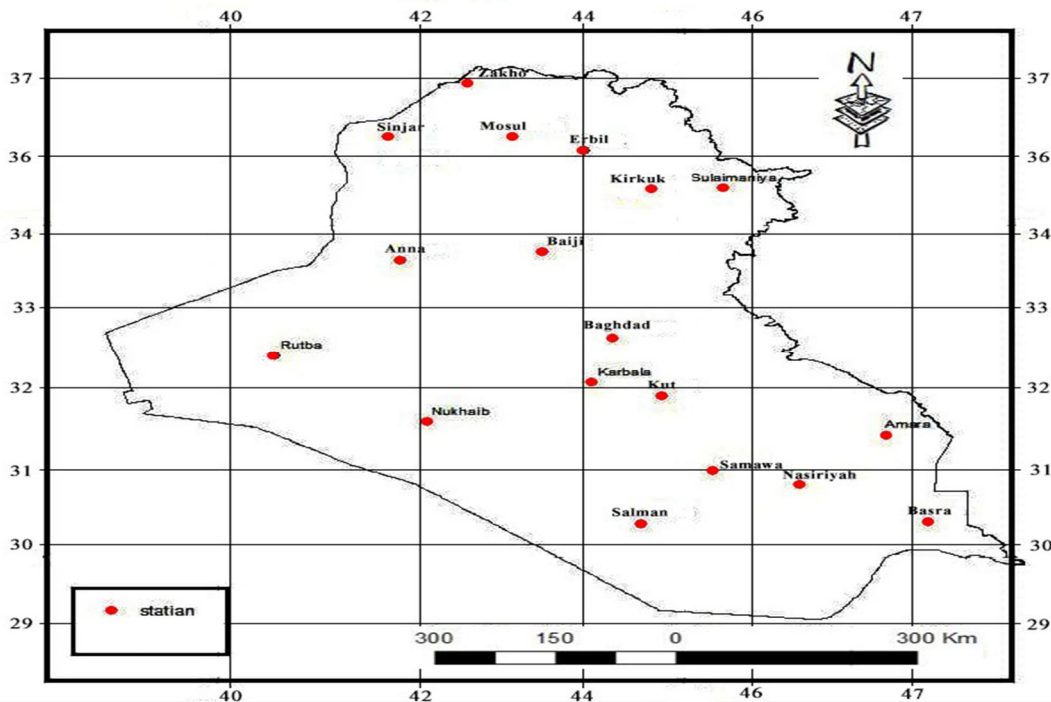


FIG .1. The location of the different stations in Iraq.

The mean monthly values of extraterrestrial radiation (H_o) are calculated by using the following equation [11].

$$H_o = \frac{24(60)}{\pi} G_{sc} \frac{dr}{[Ws]} \sin(\Phi) \sin(\delta) + \cos(\Phi) \cos(\delta) \sin(Ws) \quad (1)$$

where:

G_{sc} : is the solar constant (0.082 MJ / m².min),

dr : is the inverse relative Earth-Sun distance,

Ws : is the sunset hour angle (rad),

Φ : is the latitude (rad) and

Δ : is the solar declination (rad).

The inverse relative Earth-Sun distance (dr), and the solar declination (δ) are given by the following equations:

$$dr = 1 + 0.033 \cos \left[\frac{2\pi J}{365} \right] \quad (2)$$

$$\delta = 0.409 \sin \left[\frac{2\pi}{365} J - 1.39 \right] \quad (3)$$

where J is the day number of the year.

The sunset hour angle (Ws) is given by the following equation:

$$Ws = \arcsin [-\tan(\Phi) \tan(\delta)] \quad (4)$$

And the number of day light hours (N) are given by the following equation:

$$N = \frac{24}{\pi} Ws \quad (5)$$

The clearness index was found in 18 meteorological stations of Zakho, Mosul, Sinjar, Erbil, Sulaimaniya, Kirkuk, Baiji, Anna, Baghdad, Rutba, Kut, Nukhaib, Amara, Karbala, Samawa, Nasiriya, Salman and Basra distributed all over Iraq for the duration (1995 to 2015). Tables (2, 3) show the monthly, seasonally and annual values of KT for all stations.

GIS (V.9.3) and Surfer (V.10) were used as maps of the spatial variation of the mean monthly and seasonally values of KT obtained in Iraq.

TABLE 2. Mean monthly values of clearness index (KT) in different stations in Iraq during the period (1995-2015).

Months Stations		Jan.	Feb.	Mar.	Apr.	May	Jun.	Jul.	Aug.	Sep.	Oct.	Nov.	Dec.
Zakho	H_o	16.8	21.8	29	35.6	40.1	41.8	40.8	37	31	23.8	18	15.4
	H	7.6	10.2	13.6	17.6	21.6	24.6	24.7	22.8	18.7	13.0	8.7	7.1
	Kt	0.45	0.47	0.47	0.49	0.54	0.59	0.61	0.62	0.60	0.55	0.49	0.46
Mosul	H_o	17.3	22.3	29.4	35.8	40.1	41.7	40.8	37.1	31.3	24.2	18.5	15.9
	H	6.7	9.7	12.6	16.1	19.9	21.7	21.5	19.6	16.9	11.8	8.3	6.1
	Kt	0.39	0.44	0.43	0.45	0.50	0.52	0.53	0.53	0.54	0.49	0.45	0.38
Sinjar	H_o	17.3	22.3	29.4	35.8	40.1	41.7	40.8	37.1	31.3	24.2	18.5	15.9
	H	8.0	10.6	14.5	18.3	22.0	24.7	24.5	22.5	18.9	13.6	9.7	7.5
	Kt	0.46	0.48	0.49	0.51	0.55	0.59	0.60	0.61	0.60	0.56	0.52	0.48
Erbil	H_o	17.4	22.3	29.4	35.8	40.2	41.7	40.8	37.2	31.4	24.3	18.6	16
	H	8.0	10.8	14.5	17.6	21.5	24.5	23.9	22.4	18.8	13.5	9.5	7.3
	Kt	0.46	0.49	0.49	0.49	0.54	0.59	0.59	0.60	0.60	0.55	0.51	0.46
Sulaimaniya	H_o	17.8	22.7	29.7	36	40.2	41.7	40.8	37.3	31.6	24.6	19	16.4
	H	8.2	10.5	13.7	17.8	21.9	24.7	24.4	22.7	18.9	13.4	9.5	7.7
	Kt	0.46	0.46	0.46	0.49	0.55	0.59	0.60	0.61	0.60	0.55	0.50	0.47
Kirkuk	H_o	17.8	22.7	29.7	36	40.2	41.7	40.8	37.3	31.6	24.7	19	16.4
	H	7.7	10.2	13.3	16.9	20.7	23.0	23.5	21.9	18.8	13.6	9.4	7.0
	Kt	0.43	0.45	0.45	0.47	0.52	0.55	0.58	0.59	0.60	0.55	0.50	0.43
Baiji	H_o	18.3	23.2	30.1	36.2	40.2	41.6	40.7	37.4	31.9	25.1	19.5	16.9
	H	8.7	11.6	15.1	18.3	21.8	24.6	24.0	22.4	19.1	13.9	10.0	7.9
	Kt	0.47	0.50	0.50	0.51	0.54	0.59	0.59	0.60	0.60	0.55	0.51	0.47
Anna	H_o	18.4	23.3	30.1	36.2	40.2	41.6	40.7	37.4	32	25.2	19.6	17
	H	8.9	12.0	15.7	18.7	21.9	24.7	24.1	22.6	19.1	14.2	10.2	8.0
	Kt	0.49	0.52	0.52	0.52	0.55	0.59	0.59	0.60	0.60	0.56	0.52	0.47

Months Stations		Jan.	Feb.	Mar.	Apr.	May	Jun.	Jul.	Aug.	Sep.	Oct.	Nov.	Dec.
Baghdad	H _o	19.1	23.9	30.6	36.4	40.2	41.5	40.7	37.6	32.4	25.8	20.3	17.7
	H	10.3	13.4	16.5	20.2	22.9	25.3	25.1	23.1	19.8	15.3	11.2	9.0
	Kt	0.54	0.56	0.54	0.56	0.57	0.61	0.62	0.61	0.61	0.59	0.55	0.51
Rutba	H _o	19.3	24.1	30.7	36.5	40.2	41.5	40.7	37.6	32.4	25.9	20.5	17.9
	H	9.2	12.4	16.3	20.4	23.1	26.1	25.9	23.5	20.3	15.6	11.2	9.2
	Kt	0.48	0.52	0.53	0.56	0.58	0.63	0.64	0.63	0.63	0.60	0.55	0.51
Kut	H _o	19.7	24.4	30.9	36.6	40.2	41.4	40.7	37.7	32.6	26.2	20.8	18.3
	H	9.9	12.8	16.3	19.6	22.6	25.2	24.7	23.1	19.9	15.2	11.1	9.2
	Kt	0.50	0.53	0.53	0.54	0.56	0.61	0.61	0.61	0.61	0.58	0.53	0.50
Nukhaib	H _o	19.9	24.6	31.1	36.7	40.2	41.4	40.6	37.7	32.8	26.4	21	18.5
	H	9.9	15.7	19.7	23.0	25.3	28.6	28.2	26.6	22.8	17.6	13.6	11.0
	Kt	0.57	0.64	0.63	0.63	0.63	0.69	0.69	0.71	0.70	0.67	0.65	0.59
Karbala	H _o	19.5	24.3	30.9	36.5	40.2	41.5	40.7	37.6	32.6	26.1	20.7	18.2
	H	9.6	12.6	16.2	19.1	22.0	24.4	24.2	22.4	19.3	14.5	11.0	9.0
	Kt	0.49	0.52	0.52	0.52	0.55	0.59	0.59	0.60	0.59	0.56	0.53	0.49
Amara	H _o	20	24.7	31.2	36.7	40.2	41.4	40.6	37.7	32.8	26.5	21.1	18.6
	H	9.8	12.9	16.0	19.5	22.2	24.6	23.9	22.8	19.4	14.9	11.1	9.2
	Kt	0.49	0.52	0.51	0.53	0.55	0.59	0.59	0.61	0.59	0.56	0.53	0.49
Samawa	H _o	20.3	25	31.4	36.8	40.2	41.3	40.6	37.8	33	26.7	21.5	19
	H	10.6	13.5	16.8	19.7	22.3	24.8	24.8	23.4	19.8	15.4	11.7	9.7
	Kt	0.52	0.54	0.54	0.54	0.55	0.60	0.61	0.62	0.60	0.58	0.54	0.51
Nasiriya	H _o	20.5	25.1	31.4	36.8	40.2	41.3	40.6	37.8	33.1	26.8	21.6	19.1
	H	10.6	13.9	16.7	19.7	21.4	21.8	22.3	21.2	19.3	15.4	11.6	9.6
	Kt	0.52	0.55	0.53	0.54	0.53	0.53	0.55	0.56	0.58	0.58	0.54	0.50
Salman	H _o	20.8	25.4	31.7	36.9	40.2	41.2	40.5	37.9	33.2	27.1	21.9	19.5
	H	9.9	16.0	19.3	23.1	25.4	28.3	28.2	26.5	22.9	17.6	13.9	11.7
	Kt	0.55	0.63	0.61	0.63	0.63	0.69	0.70	0.70	0.69	0.65	0.63	0.60
Basra	H _o	20.8	25.4	31.6	36.9	40.2	41.2	40.5	37.9	33.2	27.1	21.9	19.4
	H	10.5	13.5	16.7	19.5	22.2	24.4	23.8	22.6	19.9	15.6	11.9	10.1
	Kt	0.51	0.53	0.53	0.53	0.55	0.59	0.59	0.60	0.60	0.57	0.54	0.52

TABLE 3. Mean seasonal and annual values of KT in different stations in Iraq.

Seasons/Stations	Winter	Spring	Summer	Autumn	Annual mean
Zakho	0.46	0.50	0.60	0.55	0.53
Mosul	0.40	0.46	0.53	0.50	0.47
Sinjar	0.47	0.52	0.60	0.56	0.54
Erbil	0.47	0.51	0.60	0.55	0.53
Sulaimaniya	0.46	0.50	0.60	0.55	0.53
Kirkuk	0.44	0.48	0.57	0.55	0.51
Bajji	0.48	0.52	0.59	0.55	0.54
Anna	0.51	0.53	0.60	0.56	0.55
Baghdad	0.54	0.56	0.61	0.59	0.57
Rutba	0.50	0.56	0.63	0.59	0.57
Kut	0.51	0.54	0.61	0.57	0.56
Nukhaib	0.58	0.63	0.70	0.67	0.64
Karbala	0.50	0.53	0.59	0.56	0.55

Seasons/Stations	Winter	Spring	Summer	Autumn	Annual mean
Amara	0.50	0.53	0.60	0.56	0.55
Samawa	0.52	0.54	0.61	0.57	0.56
Nasiriya	0.52	0.53	0.55	0.57	0.54
Salman	0.57	0.62	0.70	0.66	0.64
Basra	0.52	0.54	0.59	0.57	0.55

For studying the temporal variations of clearness index, five stations were selected which represent the north, middle and south parts of Iraq. These stations were (Mosul, Baiji, Baghdad, Kut and Amara).

The mean monthly, seasonally and annually values of KT in five of the selected stations were obtained by using Matlab (V.6.5) and Microsoft Office Excel 2011 different histograms.

The CV and SD for the monthly values of KT in these stations are calculated. Coefficient of variation (CV) represents the ratio of standard deviation to the mean. It's a useful statistic for comparing the degree of variation from one data series to another. Standard deviation (SD) is a statistic that measures the dispersion of a dataset relative to its mean.

Results and Discussion

Mean Monthly Values of KT in Different Stations

Table 2 shows the mean monthly values of KT in different stations in Iraq during the period (1995-2015).

The lowest KT values occurred in January, February and December, as these months are being characterized by high concentration of clouds and water vapor, in addition to that the angle of incidence of the solar radiation in these months is considered low.

Table 2 shows that the maximum value of KT during winter months is obtained in Nukhaib and Salman stations with the range of (0.61 - 0.64), while the minimum values are obtained in Mosul station with the range of (0.38-0.44).

In the months of spring (March, April and May), the table shows that the values of KT are slightly increased. Mosul station shows minimum values of a range between (0.43-0.50). Nukhaib and Salman stations reveal maximum values ranging between (0.61 -0.63).

The highest values of KT occurred most frequently between June and August. These

months typically tend to have less cloud cover in the sky.

The maximum value of KT during summer months was obtained in Nukhaib and Salman stations with the range of (0.69 - 0.71), while the minimum values were obtained in Mosul station with the range of (0.52- 0.53).

Mean Seasonally Values of KT in Different Stations

Table 3 shows the mean seasonally values of KT in all the studied Iraqi stations during the period (1995- 2015).

The maximum mean seasonal values of KT were obtained in Nukhaib station with the values of (0.58, 0.63, 0.70 and 0.67) in the seasons of winter, spring, summer and autumn, respectively.

The minimum seasonal values of KT were obtained in Mosul station with values of (0.40, 0.46, 0.53 and 0.50) in the seasons of winter, spring, summer and autumn, respectively.

Mean Annual Values of KT in Different Stations

Table 3 shows the mean annual values of KT in different stations. The maximum mean annual value of KT was obtained in Nukhaib and Salman stations with a value of (0.64), while the minimum mean annual value of KT was obtained in Mosul station with a value of (0.47).

Standard Deviation and Coefficient of Variation of KT in Different Stations

For studying the standard deviation (SD) and coefficient of variation (CV) of KT, five stations are selected to represent the north, middle and south parts of Iraq.

These stations are (Mosul, Baiji, Baghdad, Kut and Amara).

Table 4 shows the standard deviation (SD) and Table 5 reflects the coefficient of variation (CV) of the monthly values of KT during the period (1995-2015) for the five chosen stations.

We can see from Table 4 that the standard deviation of KT ranged between (0.01 - 0.05) for all stations during the months of those years.

From Table 5, we can see in winter months that the maximum values of (CV) in all stations ranged among: (6-13), (5-10), (6-7), (3-4) and

(5-8), in Mosul, Baiji, Baghdad, Kut and Amara stations, respectively.

The minimum values of (CV) are obtained in summer months with the ranges of (3-4), (4-6), (6-7), (2-4), (3-4) in these stations, respectively.

TABLE 4. Standard deviation (SD) of mean monthly values of (KT) for the selected stations during the period (1995-2015).

Months/Stations	Jan.	Feb.	Mar.	Apr.	May	Jun.	Jul.	Aug.	Sep.	Oct.	Nov.	Dec.
Mosul	0.04	0.03	0.03	0.03	0.03	0.02	0.01	0.02	0.03	0.04	0.04	0.06
Baiji	0.03	0.03	0.02	0.02	0.03	0.03	0.03	0.02	0.02	0.04	0.04	0.04
Baghdad	0.03	0.04	0.03	0.04	0.04	0.04	0.04	0.03	0.04	0.05	0.05	0.03
Kut	0.02	0.02	0.01	0.04	0.02	0.02	0.02	0.01	0.01	0.02	0.02	0.02
Amara	0.04	0.04	0.02	0.03	0.02	0.03	0.03	0.02	0.02	0.02	0.03	0.02

TABLE 5. Coefficient of variation (CV %) of mean monthly values of (KT) for the selected stations during (1995-2015).

Months/Stations	Jan.	Feb.	Mar.	Apr.	May	Jun.	Jul.	Aug.	Sep.	Oct.	Nov.	Dec.
Mosul	10	6	6	6	6	4	3	3	5	7	9	13
Baiji	5	5	3	4	6	6	5	4	3	8	8	10
Baghdad	6	7	7	8	8	7	6	6	7	9	10	7
Kut	3	4	2	7	4	3	4	2	2	4	5	4
Amara	8	8	4	6	4	4	4	3	3	4	6	5

Spatial Variation of KT in Different Regions in IRAQ

Figs. (2-a, b, c, d) show the spatial variation of the mean monthly values of clearness index during the period (1995-2015). From the figures, we can select three different regions:

The First Region: represents the north part of Iraq till Baiji station. The values of KT in this region ranged between: (0.38 - 0.50) in winter months, (0.43 - 0.55) in spring months, (0.52 - 0.62) in summer months and (0.45 - 0.60) in autumn months, respectively.

The Second Region: extends from the middle part of Iraq towards the south-east of it. This region includes the stations of (Anna, Baghdad, Rutba, Kut, Karbala, Amara, Samawa, Nasiriya and Basra).

The values of KT in this region ranged between (0.47 - 0.56) in winter months, (0.51 - 0.58) in spring months, (0.53 - 0.63) in summer months and (0.51-0.63) in autumn months, respectively.

The Third Region: formulates the south-west of Iraq and involves (Nukhaib, Salman) stations. The values of KT in this region ranged between (0.55 - 0.64) in winter months, (0.61 - 0.63) in spring months, (0.69 - 0.71) in summer months and (0.63 - 0.70) in autumn months, respectively.

In all these stations, August represents the maximum value of KT and December stands for the minimum value of KT.

Fig. 3 shows the spatial variation of the mean seasonally values of (KT).

From the figure we can nearly see three regions in all the seasons. The first region represents the north of Iraq till Baiji and Anna stations. The second region formulates the middle of Iraq toward the south-east of Iraq. The third region stands for the south-west of Iraq (Nukhaib and Salman) stations. The maximum value of KT in all these seasons was obtained in Nukhaib station, while the minimum value of KT in all stations was obtained in Mosul station.

Spatial and Temporal Variation of Clearness Index in Iraq

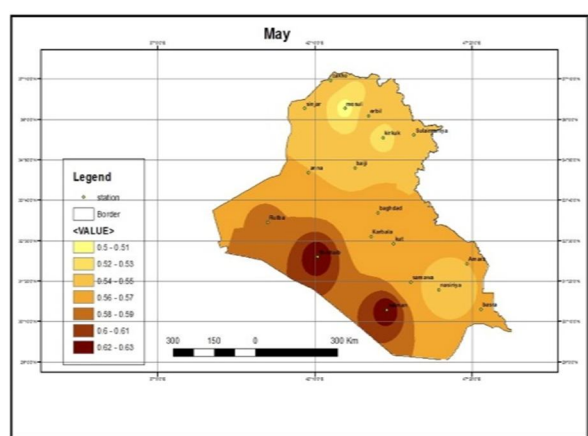
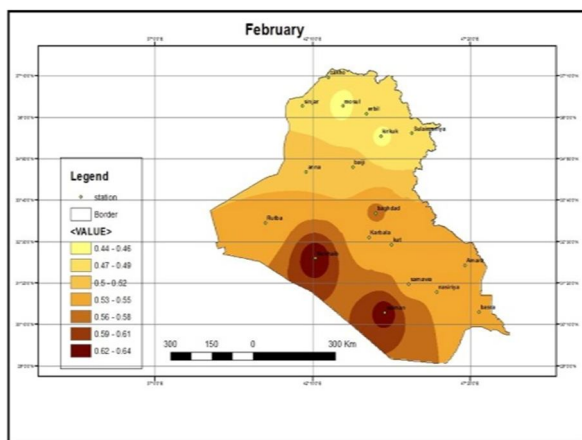
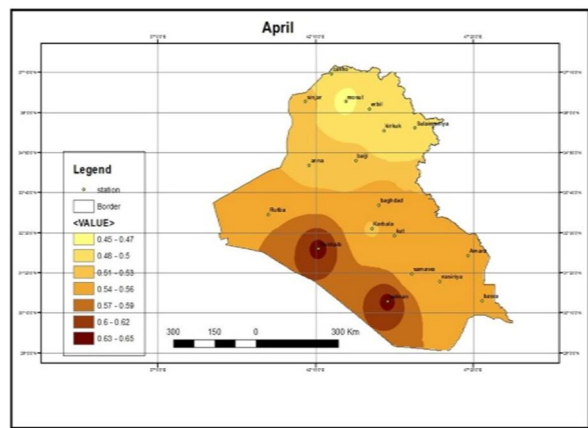
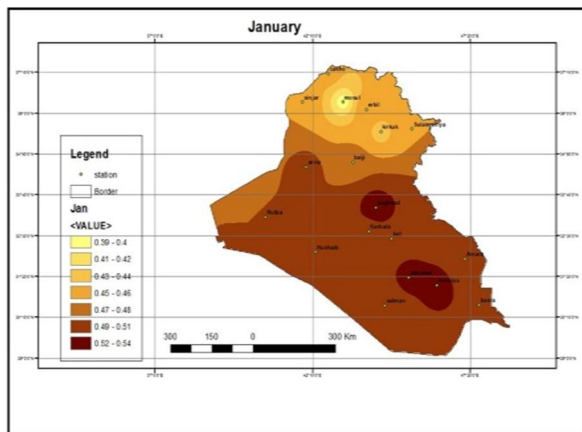
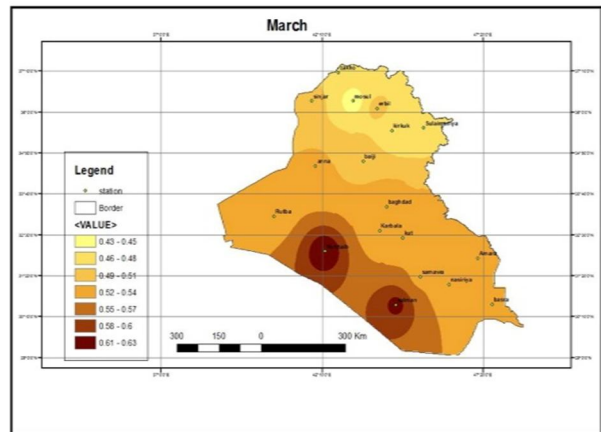
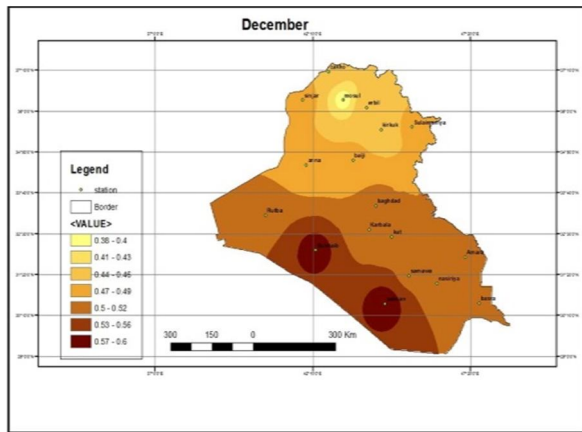


FIG. 2-a. Spatial variation of KT during winter months.

FIG. 2-b. Spatial variation of KT during spring months.

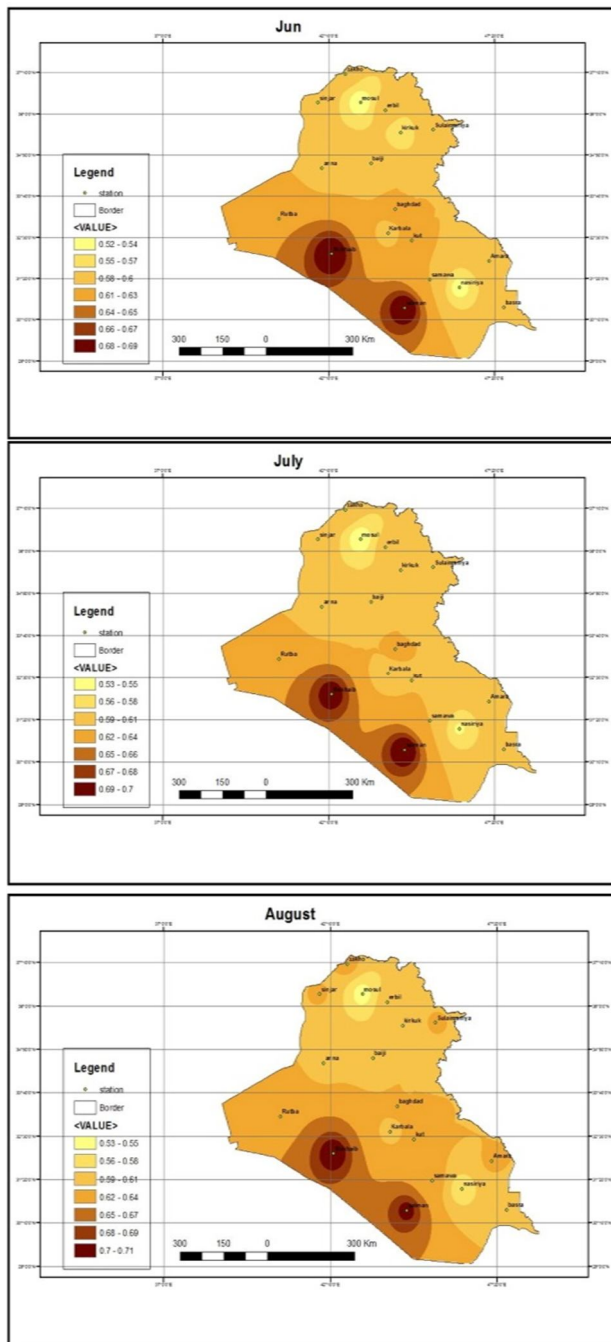


FIG. 2-c. Spatial variation of KT during summer months.

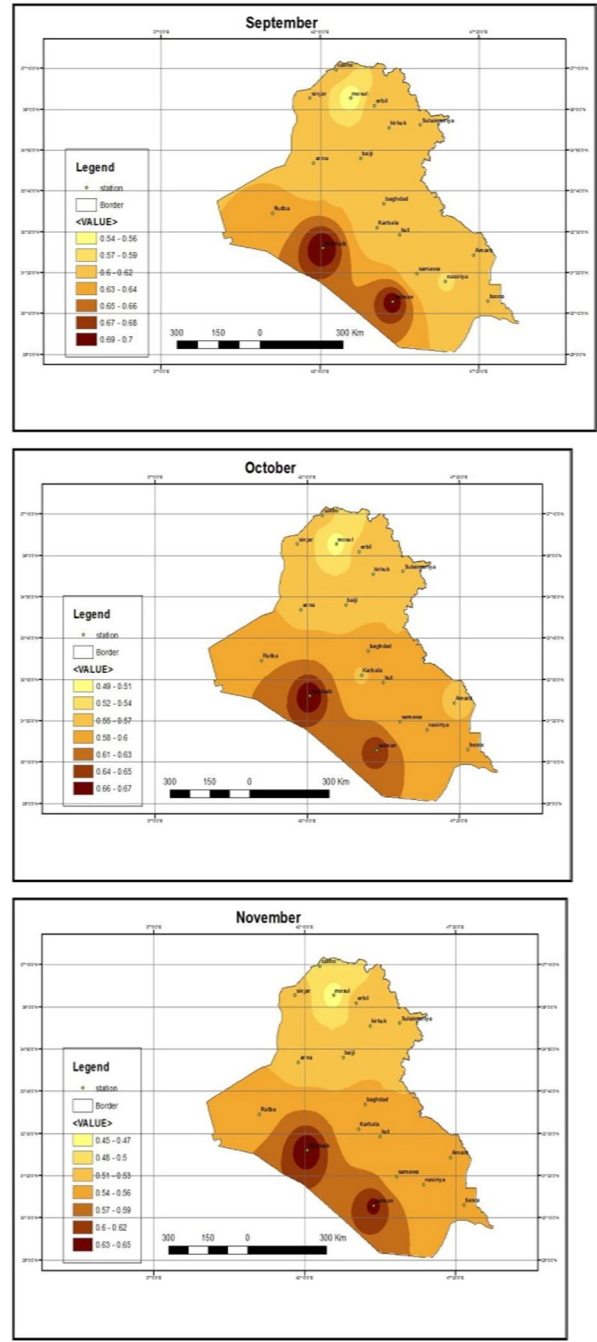


FIG. 2-d. Spatial variation of KT during autumn months.

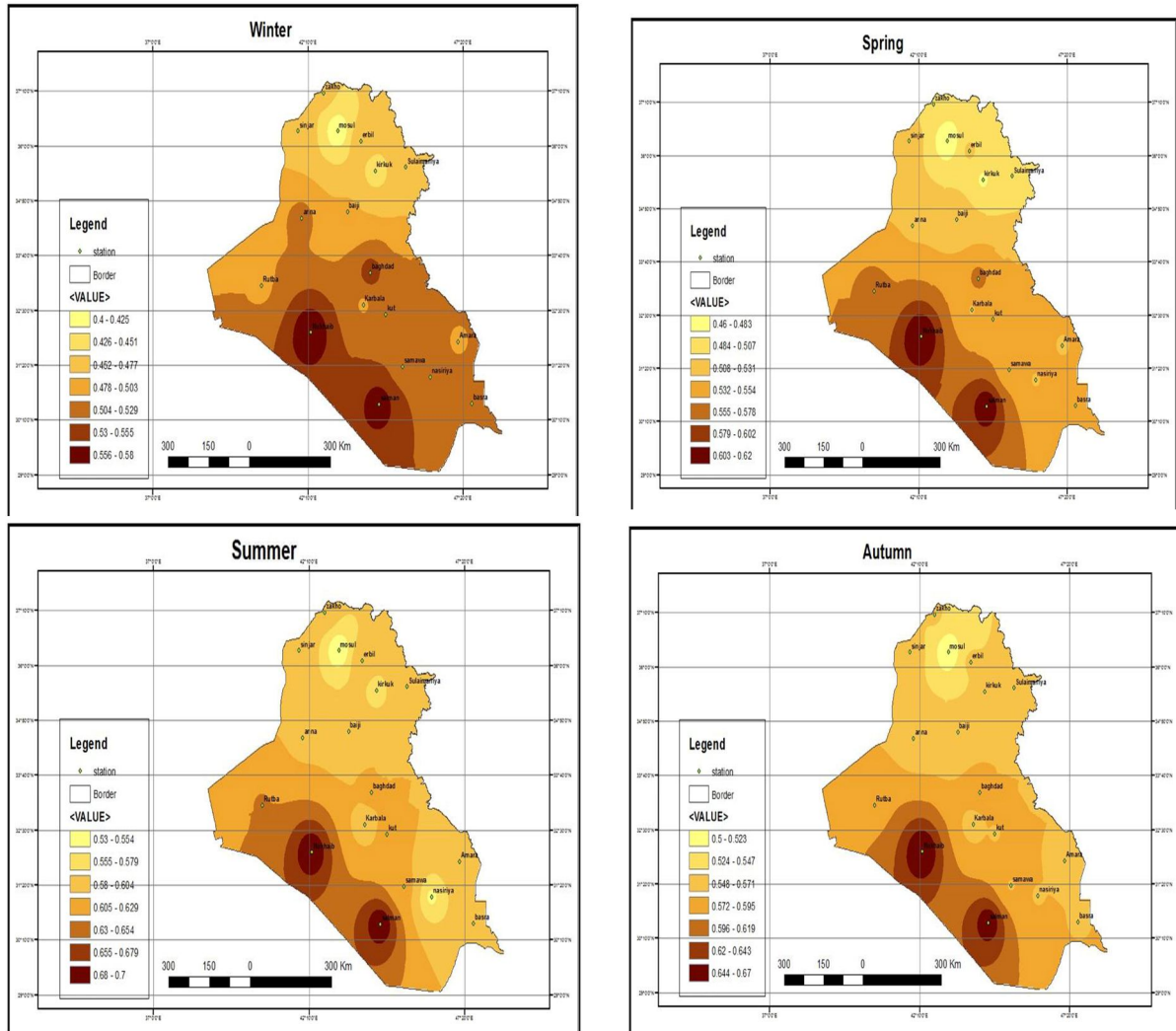


FIG. 3. Spatial variation of KT in the four seasons in Iraq.

Conclusions

In this study, solar radiation was used to evaluate the clearness index in 18 stations well distributed in Iraq during the period (1995-2015). Spatial and temporal variations of KT were studied.

The results showed that:

1. KT over Iraq varies with the geographical location and period of the year.
2. Spatial variation of KT in Iraq shows that Iraq can be divided into three zones: north, middle towards the south-east and south-west region.
3. The minimum monthly value of KT was obtained in Mosul station in December (0.38), while the maximum monthly value of KT was obtained in Nukhaib and Salman stations in Aug.(0.71)
4. The mean annual values of KT ranged between (0.47 - 0.64) in all those stations.
5. The SD of the monthly values of KT ranged between (0.01 - 0.06) for all the stations, while the CV values ranged between (2 - 13) %.

References

- [1] Serban, C., Proceedings of the 3rd International Conference on Maritime and Naval Science and Engineering, (2009).
- [2] Sanusi, Y.K. and Ojo., M.O., IOSR Journal of Applied Physics, 7 (5) (2015) 45.
- [3] Yusuf, A., International Journal of Physical Sciences Research, 1 (1) (2017) 53.
- [4] Li, D.H.W., Lau, C.C.S. and Lam, J.C., Building and Environment, 39 (1) (2004) 101.
- [5] Al-Rijabo, W.I. and Zahraa, M.H., IOSR Journal of Applied Physics, 5 (4) (2013) 08.
- [6] Kudish, A.I. and Ianetz, A., Energy Conversion and Management, 37 (4) (1996) 405.
- [7] Nematollahi, O., Alamdari, P. and Alemrajabi, A., 10th International Conference on Sustainable Energy Technologies, Istanbul, Turkey, (2011).
- [8] Waewsak, J. and Chancham, C., Thammasat Int. J. Sc. Tech., 15 (2) (2010) 54.
- [9] Al-Rijabo, W.I. and Yunis, F., Jordan J. Phys., 4 (2) (2011) 107.
- [10] Yeonjin, J., Hana, L., Jaemin, K., Youngbum, C., Jhoon, K. and Yusn, G.L., Atmosphere, 7 (4) (2016) 55.
- [11] Zakey, A.S., Abdelwahab, M.M. and Maker, P.A., Atmospheric Environment, 38 (11) (2004) 1579.
- [12] Karapantsios, T.D., Hatzimmoisiadis, K.A. and Balouktsis, A.I., Renewable Energy, 17 (1999) 169.
- [13] Iqbal, M., "An Introduction to Solar Radiation", (Academic Press, New York, 1983).

Spectroscopic and Quantum Chemical Investigations of Hypothetical *m*-Diacetylaminoazopyrimidine and Its Photovoltaic Properties

Hitler Louis, Israel Solomon Etim, Nelson Ibe Nzeata and Ayuk Usaji Atu

Department of Pure and Applied Chemistry, Faculty of Physical Sciences, University of Calabar, Calabar, Nigeria.

Doi: <https://doi.org/10.47011/14.2.5>

Received on: 17/03/2020;

Accepted on: 09/06/2020

Abstract: Here, an attempt is made to theoretically study and predict the electronic and spectroscopic (UV-Vis and IR) and structural properties, quantum chemical descriptors and subsequent application of diacetylaminoazopyrimidine in dye-sensitized solar cells (DSSCs). Ground- and excited-state time-dependent density functional theory (TD-DFT) calculations were carried out using material studio and ORCA software, respectively. The computed ground-state energy gap, chemical hardness, chemical softness, chemical potential, electronegativity and electrophilicity index are: 3.60 eV, 1.80 eV, 0.56 eV, 4.49 eV, -4.49 eV and 5.68, respectively. Conversely, the DFT-predicted excited-state quantum chemical descriptors are: 1.67 eV, 0.83 eV, 1.20 eV, 4.71 eV and -4.71 eV, corresponding to the energy gap, chemical hardness, chemical softness, chemical potential and electronegativity, respectively. Furthermore, vibrational frequency calculations confirm the presence of some key functional groups (N=N, C=O, C-H) present in the dye molecules. The computed optoelectronic parameters, such as light-harvesting efficiency, electron injection and open-circuit voltage are 0.06 eV, -8.59 eV and -5.75 eV, respectively. Overall, the dye possesses a relatively good current conversion efficiency as compared to other dyes studied in the literature; hence, it could be used as a novel material for photovoltaic technological applications.

Keywords: Diacetylaminoazopyrimidine, DFT, Excited state, Spectroscopy, DSSCs.

1. Introduction

Azo and azo-related functional groups form a highly colored class of organic compounds which are often utilized as dyes and pigments. They have attracted much attention and have been widely used in many practical applications, such as coloring fibers [1, 2], photo-electronic applications [3], printing systems [4, 5], optical storage technology [6,7], textile dyes [8-10], as well as in many biological reactions [11-13] and in analytical chemistry [14, 16]. Dye-sensitized solar cells (DSSCs) have been considered with significance interest due to the fascinating low cost of the conversion of photovoltaic energy compared to silicon-based semiconductor solar cells, as well as the availability of the raw

materials used for the fabrication of DSSC devices [17, 18]. Among other importance aspects, DSSCs utilize wide band-gap semiconductors, sensitized (dye molecules), transparent conductive oxide layers (TCO) and electrolytes (typically iodide/triiodide) [19]. The basic operational principles involve first the trapping of solar radiation by the dye molecules in the visible region of the spectrum, followed by the electronic excitation into the conductive band of the semiconductor; finally, an electron is regenerated to the dye by the redox electrolyte [20, 21].

To the best of our knowledge, neither quantum chemical calculations nor spectroscopic

investigations have yet been performed on diacetylaminopyrimidine, which is the motivating factor to carry out this investigation. Herein, quantum chemical calculations were performed in order to investigate the electronic structural properties (energy gap, charge distribution calculations), spectroscopic (UV/Vis, IR) properties, prediction of the quantum chemical descriptors (global reactivity descriptors, some geometrical parameters, such as bond lengths and bond angles), and subsequent prediction of photovoltaic properties of m-diacetylaminopyrimidine for possible application in DSSCs. Electronic absorption spectra of m-diacetylaminopyrimidine were computed and predicted by applying the time-dependent density functional theory (TD-DFT) computational method which gives information on the calculation of electronic excitation energies, oscillator strengths, total energies and maximum wavelength of absorption.

2. Computational Details

In order to obtain stable structures, the geometrical parameters of m-diacetylaminopyrimidine dye molecule (as shown in Fig. 1) in the ground state were optimized at DFT theory level using DMol3 material studio program with the dnd basis set. The frontier orbital gap helps characterize the chemical reactivity and the kinetic stability of the molecule. A molecule with a small frontier orbital gap is generally associated with a high chemical reactivity; low kinetic stability is termed as soft molecule [22]. In these processes, the potentially interesting electronic transitions are those involving narrow energy gaps. Both the Higher Occupied Molecular Orbitals (HOMO) and the Lower Unoccupied Molecular Orbitals (LUMO) are the main orbitals that take part in chemical stability. HOMO represents the ability to donate an electron, while LUMO as an electron acceptor represents the ability to acquire an electron. This electron absorption corresponds to the transition from the ground state to the first excited state and is mainly described by one electron excitation from the HOMO to the LUMO. The energy of the HOMO is directly related to the ionization potential, while LUMO energy is directly related to the electron affinity. The HOMO-LUMO analysis has been carried out to explain the charge transfer within m-diacetylaminopyrimidine.

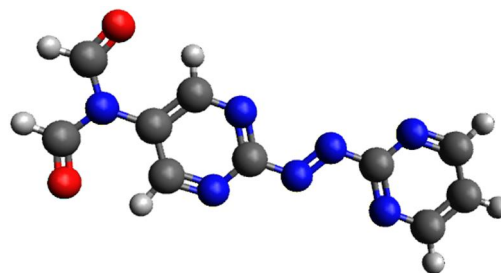


FIG. 1. Structure of m-diacetylaminopyrimidine dye molecule (the red, black, blue and white colors stand for oxygen, carbon, nitrogen and hydrogen, respectively).

HOMO and LUMO are very important parameters for quantum chemistry along with excited-state investigations. The investigation of the way the molecule interacts with other species could be elucidated from the HOMO-LUMO. HOMO, which can be thought of as the outermost orbitals containing electrons, tends to give electrons as an electron donor. On the other hand, LUMO can be thought of as the innermost orbitals containing free orbital to accept electrons. The HOMO-LUMO analysis has been carried out to explain the charge transfer within m-diacetylaminopyrimidine through the excited-state calculations with material studio.

Chemical hardness demonstrates the resistance to alteration in electron distribution. Chemical hardness formula is well correlated with the stability and reactivity of the chemical system [23]:

$$\eta = \frac{(E_{\text{LUMO}} - E_{\text{HOMO}})}{2}. \quad (1)$$

Following Parr and Pearson [24], the electronic chemical potential describes the escaping tendency of electrons from a stable system. Thus, its formula is:

$$\mu = -\frac{(E_{\text{HOMO}} + E_{\text{LUMO}})}{2}. \quad (2)$$

Chemical hardness demonstrates the resistance to alteration in electron distribution and chemical softness is an inverse of it. Chemical softness is also related with the stability and reactivity of the chemical system [23]:

$$S = \frac{1}{\eta}. \quad (3)$$

Electronegativity is described as the negative of electronic chemical potential. Since chemical potential describes the escaping tendency of

electrons from a stable system, electronegativity describes the retaining tendency of an electron in a stable system. The formula is thus [23]:

$$\chi = \frac{(E_{\text{HOMO}} + E_{\text{LUMO}})}{2}. \quad (4)$$

The global electrophilicity index introduced by Parr [23] is calculated in terms of chemical potential and hardness. It assesses the lowering of energy due to maximal electron flow between donor and acceptor. The formula is thus:

$$\omega = \mu^2 / 2\eta. \quad (5)$$

3. Results and Discussion

3.1. Geometrical Parameters

The optimized geometry of m-diacetylaminopyrimidine was obtained using material studio program and DFT method in gas phase. The structural properties (of the optimized geometrical parameters) which include bond distance and bond angle of the m-diacetylaminopyrimidine molecule in gas phase were obtained and reported in Tables 1 and 2. The total description of the molecular geometry of m-diacetylaminopyrimidine molecule in gas phase was obtained using *ab initio* and DFT method. From the optimized results, it is shown that there is no distortion in the structure and the angles are perfectly hexagonal for the heterocyclic compound (pyrimidine) molecule. This is due to the fact that there was no excitation in the ground state; therefore, the aromatic ring of pyrimidine is remaining unchanged. Also, the diacetyl amino group bonded to azopyrimidine did not act as a withdrawing group in ground state. The bond angles and distances were retained at the ground-state optimization, as shown in Tables 1 and 2. Table 1 shows that nonbonding distances from H2 to H1 and from H3 to H4 with values 2.561 Å and 2.520 Å are the highest bond distances. The least bond distance is 1.085 Å between C8-N6 atoms. From Table 2, the largest bond angle is 126.276° between the atoms of N2-C1-N1, while the least bond angle is 110.492° between the atoms of N3-C5-H3. The values obtained from the optimization are equivalent to the values obtained by Ali and coworkers [25].

TABLE 1. Ground-state bond distances in gas phase.

Bond distance	Gas phase reading in ground state (Å)
A1 (O1=C6)	1.196
A2 (C6-H2)	1.103
A3 (H2 H1)	2.561
A4 (C6-N3)	1.420
A5 (N3-C3)	1.421
A6 (N3-C5)	1.419
A7 (C5=O2)	1.196
A8 (C5-H3)	1.103
A9 (H3 H4)	2.520
A10 (C3=C2)	1.392
A11 (C2-H1)	1.086
A12 (C2-N1)	1.325
A13 (N1=C1)	1.334
A14 (C1-N2)	1.332
A15 (N2=C4)	1.323
A16 (C4-H4)	1.086
A17 (C1-N4)	1.428
A18 (N4=N5)	1.241
A19 (N5-C7)	1.430
A20 (C7=N7)	1.330
A21 (N7-C10)	1.330
A22 (C10-H5)	1.085
A23 (C10=C9)	1.387
A24 (C9-H6)	1.081
A25 (C9-C8)	1.387
A26 (C8-H7)	1.085
A27 (C8=N6)	1.332
A28 (N6-C7)	1.330

TABLE 2. Ground-state bond angles in gas phase.

Bond angle/degrees	Gas phase reading in ground state/degrees
B1 (O1=C6-H2)	123.872
B2 (O1=C6-N3)	125.618
B3 (H2-C6-N3)	110.510
B4 (C6-N3-C5)	123.009
B5 (C6-N3-C3)	118.362
B6 (N3-C3=C2)	121.695
B7 (N3-C3-C4)	122.185
B8 (N3-C5=O2)	125.952
B9 (N3-C5-H3)	110.492
B10 (O2=C5-H3)	123.555
B11 (H1-C2=C3)	120.548
B12 (H1-C2-N1)	117.343
B13 (C2=C3-C4)	116.111
B14 (C2-N1=C1)	116.621
B15 (C3=C2-N1)	122.108
B16 (C3-C4-H4)	120.596
B17 (C3-C4=N2)	122.328
B18 (H4-C4=N2)	117.074
B19 (C4=N2-C1)	116.459
B20 (N2-C1=N1)	126.276

Bond angle/degrees	Gas phase reading in ground state/degrees
B21 (N2-C1-N4)	120.724
B22 (N1=C1-N4)	112.874
B23 (C1-N4=N5)	114.344
B24 (N4=N5-C7)	112.448
B25 (N5-C7=N7)	118.177
B26 (N5-C7-N6)	113.978
B27 (C7-N6-C8)	115.596
B28 (C7=N7-C10)	115.407
B29 (N7-C10-H5)	116.379
B30 (N7-C10=C9)	122.433
B31 (H5-C10=C9)	121.185
B32 (C10=C9-H6)	121.572
B33 (C10=C9-C8)	116.577
B34 (H6-C9-C8)	121.847
B35 (C9-C8-H7)	121.307
B36 (C9-C8=N6)	122.149
B37 (H7-C8=N6)	116.541

3.2 Analysis of Frontier Molecular Orbitals

According to the interaction between the highest occupied molecular orbitals (HOMO) and the lowest unoccupied molecular orbitals (LUMO) of a structure, transitions of type $\pi - \pi^*$ are observed according to the molecular orbital theory. The calculated energy value for m-diacetylaminopyrimidine in ground state, gas phase are; $E_{\text{HOMO}} = -6.298$ eV, $E_{\text{LUMO}} = -2.697$ eV, $\Delta E = 3.601$ eV. The calculated energy value for m-diacetylaminopyrimidine in excited state, gas phase are; $E_{\text{HOMO}} = -5.540$ eV, $E_{\text{LUMO}} = -3.875$ eV, $\Delta E = 1.665$ eV. As can be seen from the calculated results of m-diacetylaminopyrimidine molecule at ground state and excited state, the energy gap is less than 4 as compared with the energy gap obtained by Yossa [26] which is greater than 4; therefore showing that our molecule is soft, can be reactive in many electronic devices and has a lower chemical reactivity with high kinetic stability. According to Demircioglu *et al.* [27], the narrow energy gap between HOMO and LUMO facilitates of the dye molecule makes the material nonlinear and optically active.

3.3 Chemical Descriptors

Comparing chemical hardness and softness, it would be observed that chemical hardness demonstrates the resistance to alteration in electron distribution in a chemical system, while chemical softness is related with the stability and reactivity of the chemical system. Chemical hardness obtained from the calculation was 1.8005 eV, whereas the calculated chemical

softness related with the stability and reactivity of the chemical system was 0.5554 eV. These obtained results show that the chemical hardness of m-diacetylaminopyrimidine at the ground state is greater than chemical softness. At the excited state, chemical hardness obtained from the calculation was 0.8325 eV, while the calculated chemical softness related with the stability and reactivity of the chemical system was 1.2012 eV. From the obtained values also, it is shown that chemical hardness is greater than chemical softness at the ground state, while chemical softness is greater than chemical hardness at the excited state. Therefore, m-diacetylaminopyrimidine at the ground state will demonstrate resistance to alteration in electron distribution in a chemical system, while at the excited state, it will demonstrate stability and reactivity when compared with Demircioglu's work [27].

Following Parr *et al.* [23], the electronic chemical potential describes the escaping tendency of electrons from a stable system and electronegativity describes the retaining tendency of an electron in a stable system. The chemical potential obtained from the calculated results of HOMO and LUMO at ground state was 4.498 eV and that obtained from the calculated value of electronegativity which is the negative value of electronic chemical potential was -4.498 eV. Also, the chemical potential obtained from the calculated results of HOMO and LUMO in the excited state was 4.7075 eV. In addition, the calculated value of electronegativity, which represents the negative value of electronic chemical potential, was found to be -4.7075 eV. The opposite values for both ground and excited states show that the electrons from a stable system will maintain their energy level without escaping [27]. According to Yossa *et al.* [26], a high value of chemical potential and electrophilicity characterizes a good electrophile, whereas a small value stands for a good nucleophile.

The global electrophilicity index assesses the lowering of energy due to maximal electron flow between donor and acceptor. The value obtained from the calculation as from chemical hardness and potential at ground-state level was 5.6184 eV. From the values of chemical potential of 4.498 eV, chemical hardness of 1.8005 eV and electrophilicity of 5.618 eV at ground-state level, electrophilicity aids in obtaining the energy of

assessing through chemical potential and hardness of the electrons. Also, the value obtained at the excited state for global electrophilicity index was 13.3096 eV. From the values of chemical potential of 4.7075 eV, chemical hardness of 0.8325 eV and electrophilicity of 13.3096 eV in the excited state level, we will have excess energy of assessing through chemical potential and hardness of the electrons. According to Yossa *et al.* [26], it is shown that m-diacetylaminoazopyrimidine is a good electrophile at the excited state and a good nucleophile at the ground state.

3.4 Mulliken Population Analyses

The calculation of atomic charges plays an important role in the application of quantum mechanical calculations to molecular systems [28]. Our interest here is in the comparison of different states of Mulliken charges to describe the electron distribution in m-diacetylaminoazopyrimidine compound as broadly as possible and assess the sensitivity of the calculated charges to changes in the choice

of the basis set. Mulliken charges are calculated by determining the electron population of each atom as defined in the basis functions. The intention is also to accurately model partial charge magnitude and location within m-diacetylaminoazopyrimidine. Mulliken analysis is a good way to account for differences in electronegativities of atoms within the molecule and use it to support Fukui analysis. The charge calculations are reported in Table 3. These results show that the Mulliken charges at complete convergence are greater and longer than the Mulliken charges at convergence. Therefore, the distribution of charges at Mulliken complete convergence will be much more rapid than the charges at Mulliken convergence. The choice of dnd basis set of material studio program is reliable, as it distinguishes clearly between the two convergences of Mulliken charges. From the population analysis, it was generally observed that 14 atoms are positively charged while 12 atoms are negativity charged.

TABLE 3. Mulliken atomic charges reading

Atom	Mulliken charges at convergence	Mulliken charges at complete convergence
C8	-0.041	-0.039
C9	0.283	0.286
C3	-0.044	-0.043
N7	-0.319	-0.316
C7	0.499	0.500
N6	-0.317	-0.316
N5	-0.171	-0.152
N4	-0.172	-0.154
C1	0.511	0.512
N2	-0.344	-0.339
N1	-0.342	-0.399
C2	0.025	0.026
C3	-0.176	-0.172
C4	0.025	0.027
N3	-0.470	-0.470
C5	0.326	0.326
C6	0.328	0.328
O1	-0.356	-0.352
O2	-0.355	-0.351
H3	0.138	0.139
H2	0.139	0.140
H4	0.174	0.179
H1	0.174	0.178
H7	0.162	0.167
H5	0.162	0.168
H6	0.161	0.168

3.5 Fukui Results and Analysis

The local reactivity descriptor like Fukui function indicates the preferred regions where a chemical species (molecule) will amend its density when the numbers of electrons are modified; or it indicates the tendency of the electronic density to deform at a given position upon accepting or donating electrons [23]. The condensed or atomic Fukui functions on the j_{th} atom site, for electrophilic $f_j^-(r)$, nucleophilic $f_j^+(r)$ and free radical f_j^0 attacks are defined as $f_j^0 f_j^+ = q_j(N + 1) - q_j, f_j^- = q_j(N) - q_j(N - 1)$ and $f_j^0 = 0.5[q_j(N + 1) - q_j(N - 1)]$ respectively, where q_j is the atomic charge (Mulliken or Hirshfeld) at the j_{th} atomic site in the anionic ($N + 1$), cationic ($N - 1$) or neutral molecule. Parr *et al.* [23] showed that sites in chemical species with the largest values of Fukui function (f_j) show high reactivity for corresponding attacks. The Fukui functions calculated from the Mulliken and Hirshfeld charges have been reported to be in good agreement [29]. The values of calculated Fukui functions for the electrophilic, nucleophilic and radical attack, as reported in Tables 4, 5 and 6,

respectively, indicate that in *m*-diacetylaminoazopyrimidine, the reactivity order for the nucleophilic case is $N4 > N5 > C9 > H5 > H1 > H4 > H7 > C3 > N6 > H6 > O1 > O2 > N7 > N2 > C7 > N1 > N7 > C8 > C2 > C4 > H3 > H2 > C6 > C5 > C1$ and the electrophilic reactivity order is $N5 > N4 > H5 > H6 > H7 > N2 > O2 > O1 > H4 > H1 > C3 > C9 > N1 > N7 > C8 > C4 > C2 > C3 > H3 > H2 > N6 > C6 > C5 > C7 > C1 > N3$, while the order of sites for free radical attack is $N4 > N5 > H5 > C9 > H7 > H6 > H1 > H4 > O2 > O1 > C3 > N2 > N7 > N6 > N1 > C3 > C7 > C8 > C2 > C4 > H3 > H2 > C5 > C6 > C1$. The local softness condensed to an atom location is defined by $s_j^\pm = f_j^\pm$ [30] and local electrophilicity indices are defined by $w_j^\pm = f_j^\pm w$ [31] and are also calculated to illustrate the reactivity of atoms. These equations envisage the most electrophilic site in a system having the maximum value of s^+ and w^+ , while maximum value of s^- and w^- corresponds to the nucleophilic site in the molecule. The local reactivity descriptors, like s_j^\pm and w_j^\pm , provide the reactivity tendencies of local site during nucleophilic or electrophilic attacks.

TABLE 4. Fukui electrophilic attack (f_j^-).

Atom	Mulliken	Hirshfeld
C8	0.018	0.029
C9	0.035	0.039
C3	0.016	0.028
N7	0.026	0.029
C7	0.005	0.008
N6	0.010	0.020
N5	0.186	0.182
N4	0.178	0.176
C1	0.004	0.016
N2	0.048	0.047
N1	0.028	0.033
C2	0.017	0.038
C3	0.039	0.058
C4	0.018	0.038
N3	0.001	0.007
C5	0.005	0.009
C6	0.005	0.010
O1	0.044	0.041
O2	0.044	0.041
H3	0.011	0.007
H2	0.010	0.007
H4	0.043	0.023
H1	0.042	0.022
H7	0.053	0.029
H5	0.058	0.033
H6	0.055	0.030

TABLE 5. Fukui nucleophilic attack (f_j^+).

Atom	Mulliken	Hirshfeld
C8	0.018	0.035
C9	0.066	0.062
C3	0.027	0.042
N7	0.041	0.046
C7	0.031	0.041
N6	0.047	0.048
N5	0.123	0.119
N4	0.142	0.136
C1	0.003	0.017
N2	0.034	0.036
N1	0.028	0.031
C2	0.014	0.035
C3	0.047	0.059
C4	0.012	0.032
N3	-0.005	0.005
C5	0.006	0.011
C6	0.006	0.010
O1	0.046	0.043
O2	0.045	0.042
H3	0.010	0.007
H2	0.009	0.006
H4	0.050	0.026
H1	0.052	0.028
H7	0.048	0.026
H5	0.054	0.032
H6	0.046	0.025

TABLE 6. Fukui free radical attack (f_j^0).

Atom	Mulliken	Hirshfeld
C8	0.018	0.032
C9	0.051	0.051
C3	0.022	0.035
N7	0.034	0.037
C7	0.018	0.024
N6	0.029	0.034
N5	0.154	0.151
N4	0.160	0.156
C1	0.004	0.017
N2	0.041	0.042
N1	0.028	0.032
C2	0.016	0.037
C3	0.043	0.059
C4	0.015	0.035
N3	-0.002	0.006
C5	0.006	0.010
C6	0.005	0.010
O1	0.045	0.042
O2	0.045	0.042
H3	0.011	0.007
H2	0.010	0.006
H4	0.047	0.025
H1	0.047	0.025
H7	0.050	0.027
H5	0.056	0.032
H6	0.050	0.028

From Table 4, Fukui electrophilic attacks at C8 down to C6 are greater at Hirshfeld charges than at Mulliken charges and Fukui electrophilic attacks at O1 to H6 are greater at Mulliken charges than at Hirshfeld charges. This shows that as Fukui electrophilic attack descends according to converging, the Mulliken charges become greater than the Hirshfeld charges. But at N5 and N4, Fukui electrophilic attacks for Mulliken charges are greater than for Hirshfeld charges for C8 to C6 range. According to Parr *et al.* [23], N5 for Mulliken is the indicated region for Fukui electrophilic attack, while N5 for Hirshfeld is also the indicated region for Fukui electrophilic attack.

A quick look at the results presented in Table 5 shows that Fukui nucleophilic attack at C9 is weak for Hirshfeld charges and strong for Mulliken charges. At N3, Fukui nucleophilic attack is weak for Mulliken charges and strong for Hirshfeld charges. From C8 down to C6 except C9, Fukui nucleophilic attack for Hirshfeld charges is greater than for Mulliken charges. And from O1 to H6, Fukui nucleophilic attacks for Mulliken charges are greater than for Hirshfeld charges. But Fukui nucleophilic attack for Mulliken charges at N5 and N4 is greater than for Hirshfeld charges. According to Parr *et al.* [23], N4 for Mulliken is the indicated region for Fukui nucleophilic attack, while N4 for Hirshfeld is also the indicated region for Fukui nucleophilic attack.

As reported in Table 6, the Fukui free radical attack is greater for Hirshfeld charges than for Mulliken charges from C8 down to C6. And Fukui free radical attacks at O1 to H6 for Mulliken charges are greater than for Hirshfeld charges. But Fukui free radical attacks at N5 and N4 for Mulliken charges are greater than for Hirshfeld charges. According to Parr *et al.* [23], N4 for Mulliken is the indicated region for Fukui radical attack, while N4 for Hirshfeld is also the indicated region for Fukui radical attack.

3.6 Electrostatic Potential (ESP) Fitted Charges

According to Muller [32], although Mulliken charges are adequate for approximating the charge on an atom, the charges generated are very basis set-dependent. A far better approach is electrostatic potential (ESP) fitting, which calculates the electrostatic potential at each point on a grid outside the molecule and then fits a set

of charges at the atoms to reproduce that potential.

As reported in Table 7, it is shown that C7 carries the highest charge followed by C1 > C3 > C8 > C2 > C4 > C6 > C5 > H5 > N3 > H6 > H7 > H3 = H2 > H4 > H1. This shows that the most positively charged atom is C7 and the most negatively charged atom is O1 m-diacetylaminoazopyrimidine.

TABLE 7. ESP fitted charges.

Atoms	ESP-fitted charges
C8	0.583
C9	-0.732
C3	0.619
N7	-0.890
C7	1.429
N6	-0.837
N5	-0.430
N4	-0.387
C1	1.296
N2	-0.806
N1	-0.755
C2	0.494
C3	-0.645
C4	0.446
N3	0.113
C5	0.329
C6	0.333
O1	-0.383
O2	-0.386
H3	0.061
H2	0.061
H4	0.057
H1	0.050
H7	0.069
H5	0.232
H6	0.079

3.7 Time-dependent Density Functional Theory (TD-DFT)

Time-dependent Density Functional Theory (TD-DFT) is a quantum mechanical theory used in physics and chemistry to investigate the properties and dynamics of many-body systems in the presence of time-dependent potentials. From the definition, the TD-DFT tabulated result (reported in Tables 8 and 9) shows an abrupt increase in eigenvalues (that is, for au and eV) from state 4 to state 5 with different spin (+ to -) orientation; same increase in eigenvalues occurs from state 18 to state 19 with same spin (- to -) orientation, then comes a drastic increment from state 38 to state 39 with the same spin (- to -) orientation. The dynamics studies show that an increase in eigenvalues can occur within a

system as a result of change in atom absorption and excitation. The positively charged eigenvalues are those of state 147 to state 148 with spin (+ to -) orientation; therefore, they are of the highest energy.

The TD-DFT excitation result in Table 9 shows an increase in energy (eV) down the table and a decrease in wavelength down the table. The oscillations show special features, as at the first spin level for each excitation a zero oscillation is observed before the second spin. Therefore, it is shown that at the first spin level, there is no oscillation and oscillations occur at the second spin level of each excitation.

TABLE 8. TD-DFT with spin unrestricted calculation.

States		Eigenvalues		
Spin		au	eV	
1	-	1	-18.761363	-510.523
2	+	1	-18.761363	-510.523
3	-	2	-18.761287	-510.521
4	+	2	-18.761287	-510.521
5	-	3	-14.064774	-382.722
6	+	3	-14.064774	-382.722
7	+	4	-14.040890	-382.072
8	-	4	-14.040890	-382.072
9	-	5	-14.040588	-382.064
10	+	5	-14.040588	-382.064
11	-	6	-14.011219	-381.265
12	+	6	-14.011218	-381.265
13	-	7	-14.010884	-381.256
14	+	7	-14.010883	-381.256
15	+	8	-13.995844	-380.846
16	-	8	-13.995843	-380.846
17	+	9	-13.995040	-380.825
18	-	9	-13.995039	-380.825
19	-	10	-10.010049	-272.387
20	+	10	-10.010049	-272.387
21	-	11	-10.010023	-272.387
22	+	11	-10.010023	-272.387
23	+	12	-9.989379	-271.825
24	-	12	-9.989378	-271.825
25	-	13	-9.977261	-271.495
26	+	13	-9.977261	-271.495
27	-	14	-9.968635	-271.260
28	+	14	-9.968635	-271.260
29	+	15	-9.962048	-271.081
30	-	15	-9.962046	-271.081
31	+	16	-9.960467	-271.038
32	-	16	-9.960467	-271.038
33	-	17	-9.942523	-270.550
34	+	17	-9.942523	-270.550
35	-	18	-9.942400	-270.547
36	+	18	-9.942400	-270.547
37	+	19	-9.912173	-269.724

States			Eigenvalues	
	Spin		au	eV
38	-	19	-9.912173	-269.724
39	-	20	-1.005929	-27.373
40	+	20	-1.005929	-27.373
41	-	21	-0.991501	-26.980
42	+	21	-0.991501	-26.980
43	-	22	-0.981861	-26.718
44	+	22	-0.981861	-26.718
45	+	23	-0.9444376	-25.698
46	-	24	-0.9444376	-25.698
47	+	25	-0.919201	-25.013
48	-	26	-0.919201	-25.013
49	-	27	-0.904054	-24.601
50	+	28	-0.904054	-24.601
51	-	28	-0.849202	-23.108
52	+	29	-0.849202	-23.108
53	+	29	-0.832600	-22.656
54	-	30	-0.832600	-22.656
55	+	31	-0.770760	-20.070
56	-	31	-0.770760	-20.070
57	+	32	-0.737551	-20.973
58	-	33	-0.737551	-20.973
59	+	33	-0.685987	-18.667
60	-	34	-0.685987	-18.667
61	+	34	-0.668289	-18.185
62	-	35	-0.668289	-18.185
63	+	35	-0.631215	-17.176
64	-	36	-0.631214	-17.176
65	+	36	-0.623338	-16.962
66	-	37	-0.623338	-16.962
67	-	37	-0.614140	-16.712
68	+	38	-0.614140	-16.712
69	+	38	-0.570230	-15.517
70	-	39	-0.570230	-15.517
71	+	39	-0.538467	-14.652
72	-	40	-0.538467	-14.652
73	-	40	-0.526409	-14.324
74	+	41	-0.526408	-14.324
75	+	41	-0.521491	-14.190
76	-	42	-0.521491	-14.190
77	+	42	-0.505805	-13.764
78	-	43	-0.505804	-13.764
79	-	43	-0.487524	-13.266
80	+	44	-0.487524	-13.266
81	+	44	-0.461962	-12.571
82	-	45	-0.461961	-12.571
83	-	45	-0.456637	-12.426
84	+	46	-0.456637	-12.426
85	-	47	-0.442610	-12.044
86	+	47	-0.442610	-12.044
87	+	48	-0.427484	-11.632
88	-	48	-0.427484	-11.632
89	+	49	-0.425746	-11.585
90	-	49	-0.425746	-11.585
91	-	50	-0.416911	-11.345
92	+	50	-0.416911	-11.345

States			Eigenvalues		States			Eigenvalues	
Spin			au	eV	Spin		au	eV	
93	+	51	-0.407886	-11.099	122	+	65	-0.268494	-7.306
94	-	51	-0.407886	-11.099	123	+	66	-0.260491	-7.088
95	+	52	-0.405175	-11.025	124	-	66	-0.260491	-7.088
96	-	52	-0.405175	-11.025	125	-	67	-0.233487	-6.354
97	-	53	-0.399591	-10.873	126	+	67	-0.233487	-6.354
98	+	53	-0.399591	-10.873	127	-	68	-0.226479	-6.163
99	-	54	-0.397365	-10.813	128	+	68	-0.226479	-6.163
100	+	54	-0.397365	-10.813	129	+	69	-0.221816	-6.036
101	-	55	-0.388507	-10.572	130	-	69	-0.221816	-6.036
102	+	55	-0.388507	-10.572	131	-	70	-0.203606	-5.540
103	+	56	-0.368445	-10.026	132	+	70	-0.203606	-5.540
104	-	56	-0.368445	-10.026	133	+	71	-0.142392	-3.875
105	+	57	-0.367048	-9.988	134	-	71	-0.142392	-3.875
106	-	57	-0.367048	-9.988	135	+	72	-0.105575	-2.873
107	-	58	-0.365940	-9.958	136	-	72	-0.105575	-2.873
108	+	58	-0.365940	-9.958	137	+	73	-0.091904	-2.501
109	+	59	-0.321793	-8.756	138	-	73	-0.091904	-2.501
110	-	59	-0.321793	-8.756	139	-	74	-0.085458	-2.325
111	-	60	-0.310440	-8.448	140	+	74	-0.085458	-2.325
112	+	60	-0.310440	-8.447	141	-	75	-0.069739	-1.898
113	+	61	-0.303417	-8.256	142	+	75	-0.069739	-1.898
114	-	61	-0.303416	-8.256	143	+	76	-0.040319	-1.097
115	-	62	-0.299552	-8.151	144	-	76	-0.040319	-1.097
116	+	62	-0.299552	-8.151	145	-	77	-0.016225	-0.442
117	+	63	-0.279786	-7.613	146	+	77	-0.016225	-0.442
118	-	63	-0.279786	-7.613	147	+	78	0.059585	1.621
119	+	64	-0.275061	-7.485	148	-	78	0.059585	1.621
120	-	64	-0.275061	-7.485					
121	-	65	-0.268494	-7.306					

TABLE 9. TD-DFT excitation result.

State			Eigenvalues		Oscillations (f)
From	To	Spin	TD-ex (eV)	TD-ex (nm)	
66	67	+	1.42	873	0.000000
66	67	-	1.95	634	0.027273
65	67	-	2.12	586	0.000000
65	67	+	2.21	560	0.000084
64	67	+	2.26	549	0.000000
64	67	-	2.32	535	0.001359
63	67	+	2.44	509	0.000000
63	67	-	2.56	485	0.020763
66	68	+	2.66	467	0.000000
66	68	-	2.69	461	0.001041
66	69	+	3.04	408	0.000000
66	69	+	3.05	407	0.001372

3.8 Vibrational Frequencies (IR)

The optimized structural parameters were used to compute the vibrational frequencies of m-diacetylaminoozopyrimidine at the DFT level of calculation. The proposed vibrational mode assignments are collected in Table 10. The simulated IR spectra have been plotted using pure Lorentzian band shapes with band width of

Full Width and Half Maximum of 10 cm^{-1} . All the vibrations are active in IR. The total energy distribution (TED) for each normal mode among the symmetry coordinates of the molecule was calculated. A complete assignment of the fundamentals was proposed based on the calculated TED values, infrared intensities. Reduction in the computed harmonic vibrations, though basis set-sensitive, are only marginal as

observed in the DFT values. Anyway, notwithstanding the level of calculations, it is customary to scale down the calculated harmonic frequencies in order to improve the agreement with the experiment. Due to some systematic errors, however, some sort of empirical correction of the force field is required to obtain an acceptable agreement (in the order 15–20 cm^{-1}) of calculated frequencies. In simpler molecules, global scaling (or uniform scaling) of the theoretical force field with one common scale factor may prove satisfactory [33]. It has been shown that application of multiple scale factors; that is, selective scaling of the *ab initio* calculated force field developed leads to better results and the natural coordinates constructed were defined as proposed by Pulay [34]. Following the SQMFF (Scaled Quantum Mechanical Force Field) procedure, the harmonic force field was scaled using the recommended scaling factors of Rauhut and Pulay.

C-H Vibrations

The hetero-aromatic structure shows the presence of C-H stretching vibrations in the region 3100–3000 cm^{-1} , which is the characteristic region for the ready identification of C–H stretching vibrations [35]. In this region, the bands are not affected appreciably by the nature of substituent. From the theoretical FT-IR spectrum, the band at 3074 cm^{-1} is assigned to the C-H stretching vibrations.

C=O Vibrations

C=O double bond gives rise to a very intense absorption band in IR spectrum. The position and intensity of this band range from 1870 cm^{-1} to 1540 cm^{-1} , depending on the physical state, electronic and mass effects of neighboring substituent, intra- and intermolecular interactions and conjugations [36]. In this study, the vibrational mode of C=O was found at 1835 cm^{-1} and 1590.77 cm^{-1} in gas phase.

C-N Vibrations

The vibrational wave number of C-N group as amines in IR spectrum ranges from 1350 – 1000 cm^{-1} , depending on the physical state, electronic and mass effects of neighboring substituent. In this study, the vibrational mode of C-N was found at 1158.66 cm^{-1} in gas phase.

N=N Vibrations

The vibrational wave number of N=N group in IR spectrum ranges from 1470 – 1400 cm^{-1} , depending on the physical state, electronic and mass effects of neighboring substituent. N=N vibration in this study was observed at 1431.62 cm^{-1} in gas phase.

Ring Vibrations

The ring stretching vibrations are expected within the region 1620 – 1390 cm^{-1} [37]. Most of the ring modes are altered by the substitution to aromatic ring. The band due to the C=C stretching vibrations is normally observed in the region 1625 – 1575 cm^{-1} [38-39]. In the present case, C=C vibrations were observed at 1766.66 cm^{-1} in gas phase.

TABLE 10. Infrared frequencies and vibrational assignment.

Mode	Frequency in cm^{-1}	Vibrational assignment
9	35.66	t_m C-C
10	54.35	
11	58.00	
12	89.26	
13	135.64	
14	152.07	torsion N-C-N
15	162.58	torsion N-C-N
16	213.82	torsion N-C-N
17	246.26	β C-C
18	257.78	β C-C
19	294.31	β C-C
20	307.88	β C-C
21	388.21	gamma C-C
22	388.28	gamma C-C
23	436.01	torsion C-C
24	443.07	torsion C-C

Mode	Frequency in cm^{-1}	Vibrational assignment
25	498.20	gamma C-C
26	516.06	torsion C-C
27	565.68	torsion C-C
28	598.44	torsion C-C
29	622.53	torsion C-H
30	666.18	torsion C-H
31	688.51	torsion C-H
32	743.73	torsion C-H
33	772.19	torsion C-H
34	788.16	torsion C-H
35	811.21	torsion C-H
36	841.13	torsion C-H
37	864.52	torsion C-H
38	866.95	torsion C-H
39	935.74	torsion C-H
40	956.31	torsion C-H
41	962.62	torsion C-H
42	969.41	torsion C-H
43	976.77	torsion C-H
44	977.35	torsion C-H
45	980.02	torsion C-H
46	1003.21	β ring, C-N
47	1032.37	s C-H, C-N
48	1061.69	t C-H, C-N
49	1077.84	β C-H, C-N
50	1101.06	C-N
51	1158.66	C-N
52	1219.06	s C-N
53	1249.83	s C-N
54	1260.50	v C-N
55	1290.10	v C-N
56	1300.96	m C-N
57	1308.25	C-N
58	1354.36	v C-H
59	1374.78	w C-H
60	1387.79	r C-H
61	1406.23	N=N
62	1417.51	N=N
63	1431.62	N=N
64	1525.07	s C-H
65	1554.25	C=O
66	1558.59	C=O
67	1571.91	C=O
68	1590.77	C=O
69	1766.60	s C=O
70	1835.24	s C=O
71	2906.58	symmetry C-H
72	2982.38	symmetry C-H
73	3066.68	symmetry C-H
74	3073.07	Asymmetry C-H
75	3074.60	Asymmetry C-H
76	3130.82	Asymmetry C-H
77	3157.71	Asymmetry C-H

v - stretching, β - in-plane bending, p - scissoring, w - wagging, r - rocking, t - twisting.

3.9 Photovoltaic Properties

3.9.1 Theoretical Background

According to Honsberg *et al.* [40], the efficiency is the most commonly used parameter to compare the performance of one solar cell to that of another. Efficiency is defined as the ratio of energy output from the solar cell to input energy from the sun. In addition to reflecting the performance of the solar cell itself, efficiency depends on the spectrum and intensity of the incident sunlight and the temperature of the solar cell. Therefore, conditions under which efficiency is measured must be carefully controlled in order to compare the performance of one device to that of another. Terrestrial solar cells are measured under AM 1.5 conditions and at a temperature of 25°C. Solar cells intended for space use are measured under AM 0 conditions. Energy conversion efficiency (η) is the ratio between the useful output of an energy conversion machine and the input in energy terms. The input, as well as the useful output maybe chemical, electric power, mechanical work, light (radiation) or heat and is given as:

$$\eta = \frac{V_{OC} J_{SC} FF}{P_{in}} \quad (6)$$

where η is the efficiency, V_{OC} is the open-circuit voltage, J_{SC} is the short-circuit current and FF is the fill factor. To analyze the relationship between V_{oc} and E_{LUMO} of the dyes based on electron injection (in DSSCs) from LUMO to the conduction band of semiconductor TiO_2 (E_{CB}), the energy relationship can be expressed as follows [41]:

$$V_{OC} = E_{LUMO} - E_{CB} \quad (7)$$

From the studied dye molecule, the LUMO values of the dye molecule and the experimental conduction band value of the TiO_2 (-4.0 eV) were applied to evaluate Eq. (7). These values are sufficient for a possible efficient electron injection. The short-circuit current density (J_{sc}) in DSSCs is determined by the following equation [42]:

$$J_{SC} = LHE(\lambda) \Phi_{inject} \eta_{collect} d\lambda \quad (8)$$

where $LHE(\lambda)$ is the light-harvesting efficiency at a given wavelength, Φ_{inject} is the electron injection efficiency and $\eta_{collect}$ denotes the charge collection efficiency. In the system where there are only differences in dye, $\eta_{collect}$ can be

assumed to be constant. The LHE can be calculated through the following equation [20]:

$$LHE = 1 - 10^{-f} \quad (9)$$

where f is the oscillator strength of adsorbed dye molecules. Φ_{inject} is related to the driving force (ΔG_{inject}) of electrons injected from the excited states of dye molecules to the semiconductor (conduction band). It can be estimated as follows [43]:

$$\Delta G_{inject} = E_{OX}^{dye*} - E_{CB}^{TiO_2} = E_{OX}^{dye} + E_{O-O}^{dye} - E_{CB}^{TiO_2} \quad (10)$$

In the above equation, E_{OX}^{dye*} is the oxidation potential of the excited state, E_{OX}^{dye} is the oxidation potential of the ground state of the dye, E_{O-O}^{dye} is the vertical transition energy and $E_{CB}^{TiO_2}$ is the conduction band edge of the TiO_2 semiconductor. So, J_{sc} can be well estimated through LHE and ΔG_{inject} .

Two models can be used for the evaluation of E_{OX}^{dye*} [44]. The first implies that the electron injection occurs from the unrelaxed excited state. For this reaction path, the excited state oxidation potential can be extracted from the redox potential of the ground state, E_{OX}^{dye} , which was calculated at the dnd basis set approach and the vertical transition energy corresponding to the photo-induced intermolecular charge transfer (ICT):

$$E_{OX}^{dye*} = E_{OX}^{dye} - \lambda_{max}^{ICT} \quad (11)$$

Here, λ_{max}^{ICT} is the energy of the ICT. Note that this relation is only valid if the entropy change during the light absorption process can be neglected as reported in previous literature [45]. For the second model, one assumes that electron injection occurs after relaxation. Given this condition, E_{OX}^{dye} is expressed as follows [45]:

$$E_{OX}^{dye*} = E_{OX}^{dye} - E_{O-O}^{dye} \quad (12)$$

3.9.2 Electron Injection

The description of the electron transfer from a dye to a semiconductor and the rate of the charge transfer process can be derived from the general classical Marcus theory [46]:

$$K_{inject} = \frac{|V_{RP}| (2/h (\pi/\lambda K_B T))^{1/2} \exp[-G_{inject} + \lambda] 2/4 K_B T}{\quad} \quad (13)$$

In Eq. (13), K_{inject} is the rate constant (in s^{-1}) of the electron injection from dye to TiO_2 , K_B is the Boltzmann thermal energy, h is the Planck constant, G_{inject} is the free energy of injection and V_{RP} is the coupling constant between the reagent and the product potential curves. Eq. (14) revealed that larger V_{RP} leads to higher rate constant which would result in a better sensitizer. The use of the generalized Mulliken-Hush (GMH) formalism allows evaluating V_{RP} for a photo-induced charge transfer [47]. It was explained that V_{RP} can be evaluated as follows [48]:

$$|V_{RP}| = \frac{\Delta E_{RP}}{2}. \quad (14)$$

The injection driving force can be formally expressed within Koopman's approximation as follows:

$$\Delta E_{RP} = [E_{LUMO}^{dye} + 2E_{HOMO}^{dye}] - [E_{LUMO}^{dye} + E_{HOMO}^{dye} + E_{CBO}^{TiO_2}] \quad (15)$$

where $E_{CBO}^{TiO_2}$ is the conduction band edge. It is difficult to accurately determine $E_{CBO}^{TiO_2}$, because it is highly sensitive to the operating conditions (e.g. the pH of the solution). Thus, we have used $E_{CBO}^{TiO_2} = -4.0\text{eV}$ [46] which is an experimental value corresponding to conditions where the semiconductor is in contact with aqueous redox electrolytes of fixed pH 7.0 [49-50]. More quantitatively, for a closed-shell system, E_{LUMO}^{dye} corresponds to the reduction potential of the dye E_{RED}^{dye} , whereas the HOMO energy is related to the potential of the first oxidation (that is, $E_{HOMO}^{dye} = E_{OX}^{dye}$). As a result, Eq. (15) becomes:

$$\Delta E_{RP} = E_{OX}^{dye} + E_{OX}^{TiO_2}. \quad (16)$$

According to Koopman's theory, the ground-state oxidation potential energy is related to ionization energy [51].

The photovoltaic properties λ_{max} , ΔG_{inject} , E_{OX}^{dye*} , E_{OX}^{dye} , λ_{max}^{CT} and LHE are presented in Table 11. The short-circuit current (J_{SC}) depends on two main influencing factors: light-harvesting efficiency (LHE) and the electronic injection free energy (ΔG_{inject}) (Eq. (10)). The LHE is considered as a very important factor for the organic dyes in which we could appreciate the role of the dyes in the DSSC; i.e., absorbing photons and injecting photo-excited electrons to the conduction band of the semiconductor

(TiO_2). In order to know what to give as an intuitional impression of the influence of the donor spacer of the LHE, we compared this research project with Juma *et al.* [20] and observed that the oscillator strengths were changing at different excitations. As shown in Table 11, the LHE has a value that's less than 1 and ΔG_{inject} is negative; these values reveal that the electron injection process is spontaneous [52] and m-diacetylaminoozopyrimidine at the excited state would be located above the conduction band edge of TiO_2 , resulting in a favorable condition for electron injection.

Also, comparing this research project with Juma *et al.* [20], it was observed that m-diacetylaminoozopyrimidine has a smaller ΔG_{inject} . Based just on LHE and ΔG_{inject} related to J_{SC} according to Bourass *et al.* [19], we could conclude that the dye-synthesized solar cell containing the m-diacetylaminoozopyrimidine should have the lowest J_{SC} due to its relatively small LHE and injection driving force.

From the calculation, it is revealed that m-diacetylaminoozopyrimidine has the smallest electron injection value due to its carbonyl (acetyl) as withdrawing group. With regard to light-harvesting efficiency which is responsible for power conversion efficiency, the higher the LHE, the higher the power conversion efficiency.

TABLE 11. Photovoltaic properties of dyes in gas phase.

Photovoltaic properties	Values obtained (eV)
E_{OX}^{dye}	-2.697
E_{OX}^{dye*}	-5.5
ΔG_{inject}	-8.59
(LHE)	0.060868
V_{OC}	1.303
$ V_{RP} $	-1.1515

4. Conclusion

This study being the maiden quantum mechanical/theoretical investigation on the hypothetical m-diacetylaminoozopyrimidine, complete vibrational and molecular structure analysis has been carried out using DMol3 Density Functional Theory (DFT) methods.

At the ground-state study, we observed that the molecular structure and geometry of m-diacetylaminoozopyrimidine were maintained

because of the resistance to alteration in electron distribution by chemical hardness. The highest occupied molecular orbital (HOMO) and the lowest unoccupied molecular orbital (LUMO) energies can be used to semi-quantitatively estimate the ionization potential, electron affinity, electronegativity, electrophilicity index, chemical potential, chemical hardness and chemical softness.

In order to understand electronic transitions and vibrations of m-diacetylaminoazopyrimidine at the excited state, TD-DFT calculations on FT-IR spectra in gas phase were also performed. It was observed that m-diacetylaminoazopyrimidine showed a distortion on the aromatic heterocyclic ring. Fukui function helps identify the electrophilic and nucleophilic nature of a specific site within the molecule. According to stability of the molecule to

softness, the molecule at least energy gap as compared with ground state and other research work is much more reactive.

It was observed that the high conjugated double bonds have both high absorption spectra and increased electron injection efficiency and the conjugations made the energy gap decrease at the excited state. Therefore, the investigation shows that m-diacetylaminoazopyrimidine is better for application in dye-synthesized solar cells (DSSCs).

Funding

Although this work was not supported by any funding agencies, the authors are thankful to Prof. Dr. Ayuk for his immense support and contributions.

References

- [1] Koh, J., Greaves, A.J. and Kim, J.P., *Dyes and Pigments*, 56 (1) (2003) 69.
- [2] Sekar, N., *Colourage*, 51 (2004) 59.
- [3] Katz, H.E., Lovinger, A.J., Johnson, J., Kloc, C., Siegrist, T., Li, W. and Dodabalapur, A., *Nature*, 404 (6777) (2000) 478.
- [4] Abe, H., Yoneda, M. and Fujiwara, N., *Japanese Journal of Applied Physics*, 47 (3R) (2008) 1435.
- [5] Chino, T. and Yamada, M., *J.P.*, (2002) 2001220519.
- [6] Wang, S., Shen, S. and Xu, H., *Dyes and Pigments*, 44 (3) (2000) 195.
- [7] Kuwahara, M., Takehara, S., Kashihara, Y., Watabe, K., Nakano, T., Tanaka, M., Nakamura, N., Ohsawa, H. and Satoh, H., *Jpn. J. Appl. Phys.*, 42 (2003) 1068.
- [8] Rangnekar, D.W., Kanetkar, V.R., Malanker, J.V. and Shankarling, G.S., *Indian Journal of Fibre & Textile Research (IJFTR)*, 24 (2) (1999) 142.
- [9] Hallas, G. and Choi, J.H., *Dyes and Pigments*, 40 (2-3) (1999) 119.
- [10] Gregory, P., Waring, D.R. and Hallos, G., "The chemistry and application of dyes". (Plenum Press, London, 1990), 18-20.
- [11] Kondil, S.S., *Transition Met. Chem.*, 23 (1998) 461.
- [12] Daniel, J.W., *Toxicology and Applied Pharmacology*, 4 (5) (1962) 572.
- [13] Woissetschläger, O.E., Sünkel, K., Weigand, W. and Beck, W., *Journal of Organometallic Chemistry*, 584 (1) (1999) 122.
- [14] Broekaert, J.A.C., Leis, F. and Laqua, K., *Talanta*, 28 (10) (1981) 745.
- [15] Amin, A.S. and Mohammed, T.Y., *Talanta*, 54 (4) (2001) 611.
- [16] Yazdanbakhsh, M.R., Yousefi, H., Mamaghani, M., Moradi, E.O., Rassa, M., Pouramir, H. and Bagheri, M., *Journal of Molecular Liquids*, 169 (2012) 21.
- [17] Gonçalves, L.M., de Zea Bermudez, V., Ribeiro, H.A. and Mendes, A.M., *Energy & Environmental Science*, 1 (6) (2008) 655.
- [18] Zhang, J., Li, H.B., Sun, S.L., Geng, Y., Wu, Y. and Su, Z.M., *Journal of Materials Chemistry*, 22 (2) (2012) 568.
- [19] Bourass, M., Benjelloun, A.T., Benzakour, M., Mcharfi, M., Hamidi, M., Bouzzine, S.M. and Bouachrine, M., *Journal of Materials and Environmental Science*, 7 (2016) 700.
- [20] Juma, J.M., Vuai, S.A.H. and Babu, N.S., *International Journal of Photoenergy*, 2019 (2019) 4616198.

- [21] Janjua, M.R.S.A., *Journal of the Chilean Chemical Society*, 63 (1) (2018) 3850.
- [22] Fleming, I., "Molecular Orbitals and Organic Chemical Reactions", (John Wiley & Sons, 2011).
- [23] Parr, R.G. and Yang, W., *Journal of the American Chemical Society*, 106 (14) (1984) 4049.
- [24] Parr, R.G., *International Journal of Quantum Chemistry*, 37 (4) (1990) 327.
- [25] Ali, M., Mansha, A., Asim, S., Zahid, M., Usman, M. and Ali, N., *Journal of Spectroscopy*, 2018 (2018) 9365153.
- [26] Yossa Kamsi, R.A., Ejuh, G.W., Tchoffo, F., Mkounga, P. and Ndjaka, J.M.B., *Advances in Condensed Matter Physics*, 2019 (2019) 4246810.
- [27] Demircioğlu, Z., Kaştaş, Ç.A. and Büyükgüngör, O., *Journal of Molecular Structure*, 1091 (2015) 183.
- [28] Mulliken, R.S., *J. Chem. Phys.*, 23 (1955) 1841.
- [29] Nazari, F. and Zali, F.R., *Journal of Molecular Structure: Theochem.*, 817 (1-3) (2007) 11.
- [30] Lee, C., Yang, W. and Parr, R.G., *Journal of Molecular Structure: Theochem.*, 163 (1988) 305.
- [31] Chattaraj, P.K., Maiti, B. and Sarkar, U., *The Journal of Physical Chemistry A*, 107 (25) (2003) 4973.
- [32] Muller, R.P. and Warshel, A., *The Journal of Physical Chemistry*, 99 (49) (1995) 17516.
- [33] Scott, A.P. and Radom, L., *J. Chem. Phys.*, 100 (1996) 16502.
- [34] Pulay, P., Fogarasi, G., Pongor, G., Boggs, J.E. and Vargha, A., *Journal of the American Chemical Society*, 105 (24) (1983) 7037.
- [35] Varsányi, G., "Assignments for vibrational spectra of seven hundred benzene derivatives", Vol. 1, (Halsted Press, 1974).
- [36] Temel, E., Alaşalvar, C., Eserci, H. and Açar, E., *Journal of Molecular Structure*, 1128 (2017) 5.
- [37] Pecsok, R.L., "Modern Methods of Chemical Analysis", (Wiley, 1976).
- [38] Sharma, Y.R., "Elementary Organic Spectroscopy: Principles and Chemical Application". (Chand and Company, Ltd., New Delhi, India, 2009).
- [39] Kalsi, P.S., "Spectroscopy of Organic Compounds", (New Age International, 2007).
- [40] Hohenberg, P. and Kohn, W., "Inhomogeneous Electron Gas *Physical Review* 136", (B864, 1964).
- [41] Marinado, T., Nonomura, K., Nissfolk, J., Karlsson, M.K., Hagberg, D.P., Sun, L.,... & Hagfeldt, A., *Langmuir*, 26 (4) (2010) 2592.
- [42] Zhang, J., Li, H.B., Sun, S.L., Geng, Y., Wu, Y. and Su, Z.M., *Journal of Materials Chemistry*, 22 (2) (2012) 568.
- [43] Ninis, O., Bouzzine, S.M., Toufik, H., Lamchouri, F., Abarkan, M., Hamidi, M. and Bouachrine, M., *Journal of Applied Chemical Research*, 7 (1) (2013) 19.
- [44] Barbara, P.F., Meyer, T.J. and Ratner, M.A., *The Journal of Physical Chemistry*, 100 (31) (1996) 13148.
- [45] De Angelis, F., Fantacci, S. and Selloni, A., *Nanotechnology*, 19 (42) (2008) 424002.
- [46] Marcus, R.A., *Angewandte Chemie, International Edition in English*, 32 (8) (1993) 1111.
- [47] Pourtois, G., Beljonne, D., Cornil, J., Ratner, M.A. and Brédas, J.L., *Journal of the American Chemical Society*, 124 (16) (2002) 4436.
- [48] Hsu, C.P., *Accounts of Chemical Research*, 42 (4) (2009) 509.
- [49] Asbury, J.B., Wang, Y.Q., Hao, E., Ghosh, H.N. and Lian, T., *Research on Chemical Intermediates*, 27 (4-5) (2001) 393.
- [50] Katoh, R., Furube, A., Yoshihara, T., Hara, K., Fujihashi, G., Takano, S. and Tachiya, M., *The Journal of Physical Chemistry B*, 108 (15) (2004) 4818.
- [51] Babu, N.S. and Jayaprakash, D., *HOMO*, 1 (2015) 1.
- [52] El Assyry, A., Jdaa, R., Benali, B., Addou, M. and Zarrouk, A., *Journal of Materials and Environmental Science*, 6 (9) (2015) 2612.

Coupling of Upper Hybrid Surface Plasmon Modes in Magnetoplasma Waveguide Structure

Fuad Rawwagah

Department of Physics, Yarmouk University, 211-63 Irbid, Jordan.

Doi: <https://doi.org/10.47011/14.2.6>

Received on: 20/03/2020;

Accepted on: 27/07/2020

Abstract: We investigate the spectra of high-frequency electrostatic surface electron plasmon oscillations propagating normal to a dc-magnetic field. These oscillations are supported by two identical magnetoplasma slabs separated by a vacuum slab. Propagation characteristics of surface magnetoplasma oscillations and their coupling are studied by simultaneously solving the homogeneous system of equations obtained by matching the electrostatic fields at the interfaces together with the warm plasma dielectric function of upper hybrid waves. We demonstrate the existence of two propagating magnetoplasma electrostatic surface modes (backward and forward modes). The backward mode emerges at frequency $\omega = \omega_{uh} = \sqrt{\omega_{pe}^2 + \omega_{ce}^2}$, where ω_{pe} and ω_{ce} are the electron plasma frequency and the electron cyclotron frequency, respectively, and the forward propagating mode emerges at a lower frequency $\omega = \omega_{uh} - \omega_{pe}$. The forward and backward surface modes become coupled and form a single mode at upper hybrid resonance quasi-static value $\omega = \omega_{uh}/\sqrt{2}$.

Keywords: Upper hybrid modes, Plasma slab waveguide, Coupled plasmon surface modes.

1. Introduction

The study of electron plasma wave interaction in the presence of magnetic fields is of importance for plasma heating and plasma diagnostics [1-6]. In the presence of a dc-magnetic field, the bulk electron plasma frequency ω_{pe} transforms into the upper hybrid (UH) frequency ω_{uh} . Understanding the mechanisms of excitation of UH waves is crucial for explaining certain features of the stimulated emission of electromagnetic waves observed in ionospheric heating experiments. In planetary magnetospheres and in the Earth's ionosphere, a large amplitude upper hybrid wave can nonlinearly excite a slow electromagnetic wave of X or Z type [7, 8]. In space plasmas, UH waves can be generated either by mode coupling or by electron beams, which then can decay into electromagnetic and lower hybrid waves [9].

Electrostatic UH waves can be induced when an obliquely incident electromagnetic wave is converted into an electrostatic wave of UH type due to density irregularities. Effects of mass motion on the evolution of electrostatic waves and instabilities have been studied analytically by Mohanty and Naik [10]. It was found that streaming motion enhances the wave frequency and diminishes the terms related to growth or damping of electrostatic instabilities.

Due to the fact that plasma can have a negative dielectric constant in certain frequency domains, propagation of true surface waves along a plasma-dielectric interface is possible [11]. There is a great interest in studying the propagation of waves on the plasma boundary, as most plasmas in laboratory and space

applications involve boundaries. It is well known that the propagation of a pure surface wave (i.e., a wave whose field decreases exponentially away from the interface) between two media is possible only when the permittivities of the two media have opposite signs [12-20].

This article studies high-frequency electron surface plasma modes of oscillation propagating perpendicular to an undisturbed magnetic field. These oscillations are supported by two identical, parallel and homogeneous plasma slabs separated by a vacuum slab. In Sec. 2, we present the model equations of the high-frequency electrostatic modes of magnetoplasma slabs. In Sec. 3, numerical examples of vacuum-plasma-vacuum-plasma-vacuum geometry are presented. Finally, we discuss the results and present the main conclusions of the paper in Sec. 4.

2. Model Equations

We consider a dielectric slab of thickness d and permittivity ϵ_d extending infinitely in the yz -plane between two infinite parallel plasma slabs of equal thicknesses ℓ and dielectric permittivities $\epsilon_p = \epsilon_0 \epsilon_p$, where ϵ_p is the plasma dielectric function. The rest of the space is taken to be vacuum, as shown in Fig. 1. For high-frequency waves, the dynamics of the ions can be neglected, which allows for treating the ions as a fixed uniform background of positive charges. The motion of the electrons is governed by the following closed system of equations [21, 22],

$$\frac{\partial n_e}{\partial t} + \vec{\nabla} \cdot (n_e \vec{v}_e) = 0, \quad (1)$$

$$m_e n_e \frac{d\vec{v}_e}{dt} = -en_e \vec{E} - en_e \vec{v}_e \times \vec{B} - m_e n_e \nu \vec{v}_e - \gamma_e k_B T \vec{\nabla} n_e, \quad (2)$$

$$\vec{\nabla} \cdot \vec{E} = -\frac{e}{\epsilon_0} (Zn_{0i} - n_e), \quad (3)$$

where m_e is the electron mass, e is the magnitude of electronic charge, ϵ_0 is the permittivity of free-space, γ_e is the ratio of specific heats, k_B is Boltzmann constant, T_e is the temperature of electrons, n_e is the electron density, ν is the electron collision frequency with neutrals, n_{0i} is the equilibrium ion density and Z

is the charge state. The coupled equations (1–3) can be linearized with:

$$n_e = n_{0e} + n_{1e}, \vec{v}_e = \vec{v}_{0e} + \vec{v}_{1e}, \vec{E} = \vec{E}_0 + \vec{E}_1, \vec{B} = B_0 \hat{z}, \quad (4)$$

where the quantities with subscript 0 express the state of the magnetoplasma in the absence of oscillations. Perturbation terms of corresponding quantities are denoted by subscript 1. In the absence of an initial electron drift ($\vec{v}_{0e} = 0$), this procedure results in the following dielectric permittivity of the electrostatic electron plasma waves in a homogeneous magnetoplasma [22-24]:

$$\epsilon_p = 1 - \frac{\omega_{pe}^2}{\omega(\omega + i\nu) - \omega_{ce}^2 - 3\nu_{th,e}^2 k^2}, \quad (5)$$

where ω_{pe} is the electron plasma frequency, ω_{ce} is the electron cyclotron frequency, ν is an effective collision frequency of electrons with neutrals, and $\nu_{th,e} = \sqrt{k_B T_e / m_e}$ is the electron thermal speed. The natural modes of Eq. (5) are the electrostatic upper hybrid waves across the dc-magnetic field in warm, collisional, and magnetized plasma.

In the electrostatic limit $\omega \sqrt{\mu_0 \epsilon} \ll 1$, the magnetic field component of the electromagnetic wave can be neglected. Accordingly, in a source-free nonconducting medium, the electric field obeys Laplace's equation. Without loss of generality, we will consider the surface wave modes that propagate along the interface in the y -direction such that:

$$E_y(x, y) = u(x) e^{iky}, \text{ and } E_x(x, y) = -\frac{i}{k} \frac{dE_y(x, y)}{dx}, \quad (6)$$

where $u(x)$ is a function that accounts for the electric field variations with x . Consequently, the function $u(x)$ obeys the equation $u''(x) - k^2 u(x) = 0$. For the waves guided by any planar structure, the propagation constant k must be the same in all regions of the guiding structure. This is a necessary condition for the existence of guided mode. Thus, in the electrostatic limit under consideration, the wave vector k is the same over all the regions of the structure.

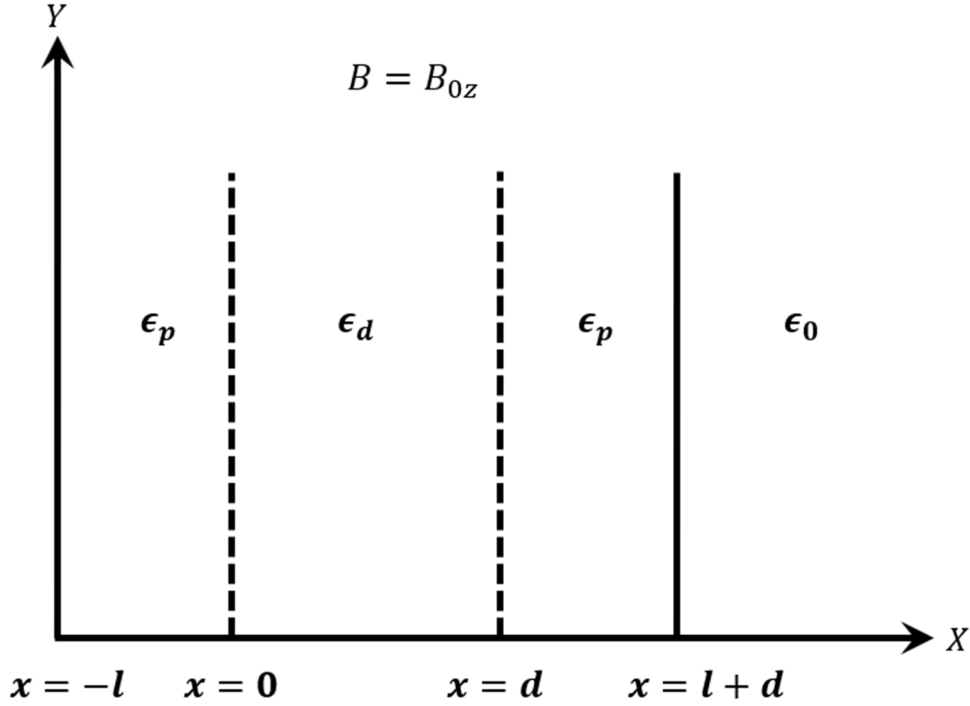


FIG. 1. Geometry of the problem.

Then, the electric field $E_y(x, y)$ in each slab of the waveguide geometry of Fig. 1 can be written as:

$$E_y^{(1)} = A_1 e^{k(iy+x)} \quad -\infty < x \leq -l \quad (7)$$

$$E_y^{(2)} = A_2 e^{k(iy+x)} + A_3 e^{k(iy-x)} \quad -l \leq x \leq 0 \quad (8)$$

$$E_y^{(3)} = A_4 e^{k(iy+x)} + A_5 e^{k(iy-x)} \quad 0 \leq x \leq d \quad (9)$$

$$E_y^{(4)} = A_6 e^{k(iy+x)} + A_7 e^{k(iy-x)} \quad d \leq x \leq d+l \quad (10)$$

$$E_y^{(5)} = A_8 e^{k(iy-x)} \quad d+l \leq x < \infty \quad (11)$$

In the electrostatic limit, applying the boundary conditions returns the continuity of the tangential component of the electric field and the normal component of the electric displacement vector $\vec{D} = \epsilon \vec{E}$. Accordingly, matching the tangential electric field E_y and the normal electric displacement D_x components at all interfaces leads to the following 8×8 homogeneous system of equations:

$$A_1 e^{-kl} - A_2 e^{-kl} - A_3 e^{kl} = 0 \quad (12)$$

$$\frac{A_1}{\epsilon_p} e^{-kl} - A_2 e^{-kl} + A_3 e^{kl} = 0 \quad (13)$$

$$A_2 + A_3 - A_4 - A_5 = 0 \quad (14)$$

$$\frac{\epsilon_p}{\epsilon_d} A_2 - \frac{\epsilon_p}{\epsilon_d} A_3 - A_4 + A_5 = 0 \quad (15)$$

$$A_4 e^{kd} + A_5 e^{-kd} - A_6 e^{kd} - A_7 e^{-kd} = 0 \quad (16)$$

$$A_4 e^{kd} - A_5 e^{-kd} - \frac{\epsilon_p}{\epsilon_d} A_6 + \frac{\epsilon_p}{\epsilon_d} A_7 = 0 \quad (17)$$

$$A_6 e^{k(d+l)} + A_7 e^{-k(d+l)} - A_8 e^{-k(d+l)} = 0 \quad (18)$$

$$A_6 e^{k(d+l)} - A_7 e^{-k(d+l)} + \frac{A_8}{\epsilon_p} e^{-k(d+l)} = 0 \quad (19)$$

3. Numerical Analysis and Example

In Figs. 2 and 3, we use Eqs. (12-19) together with Eq. (5) to plot the normalized mode frequency ω/ω_{pe} versus $k\lambda_D$ for the case of vacuum as a central region between the plasma slabs with $\epsilon_d = 1$. Here, $\lambda_D = v_{th,e}/\omega_{pe}$ is the electron Debye wavelength. The values of $k\lambda_D \ll 1$ are within the validity of the warm plasma approximation (long wavelength limit) [21-25].

The curves in Fig. 2 show the normalized mode frequencies for different values of cyclotron frequency ω_{ce}/ω_{pe} . For $\omega_{ce} = 0$, we observe two well known electrostatic modes, which emerge from $\omega = 0$ and $\omega = \omega_{pe}$. Both modes become coupled as $k\lambda_D$ increases and eventually degenerate into a single mode at the

quasi-static frequency $\omega = \frac{\omega_{pe}}{\sqrt{2}}$ of the plasma-vacuum interface [13, 15, 25]. By increasing the magnetic field, the mode frequencies shift up and become coupled at higher quasi-static surface wave frequency $\omega = \omega_{uh}/\sqrt{2}$. The shift is of the order of $\Delta\omega = \omega_{uh} - \omega_{pe}$. The bulk plasma mode at $\omega = \omega_{pe}$ for $\omega_{ce} = 0$ shifts upward toward the upper hybrid frequency $\omega_{uh} = \sqrt{\omega_{pe}^2 + \omega_{ce}^2}$. For $\omega_{ce} = \omega_{pe}$, for example, the upper hybrid frequency is $1.4\omega_{pe}$ with an upward shift of $\Delta\omega = 0.4\omega_{pe}$.

Curves of Fig. 3 show the normalized mode frequencies for different values of vacuum slab width to plasma slab width d/ℓ . To find out the effect of the width of the central vacuum slab on

the coupling of the electrostatic surface modes in a magnetoplasma, we consider the fixed value $\omega_{ce} = \omega_{pe}$ as a representative case. In the absence of the central slab (i.e., $d = 0$), the magnetoplasma slab has a width of 2ℓ and is surrounded by semi-infinite vacuum regions. In this case, we observe two uncoupled modes; namely, $\omega = \omega_{uh} = 1.4\omega_{pe}$ and a second mode, which emerges from the bulk plasma mode and approaches the quasi-static value $\omega \approx \omega_{uh}/\sqrt{2} = 1.22\omega_{pe}$. For $d \neq 0$, the bulk upper hybrid mode at $\omega = \omega_{uh} = 1.4\omega_{pe}$ and the bulk plasma mode at $\omega = \omega_{pe}$ become coupled and the coupled mode frequency approaches the upper hybrid quasi-static value $\omega = \omega_{uh}/\sqrt{2} = 1.22\omega_{pe}$.

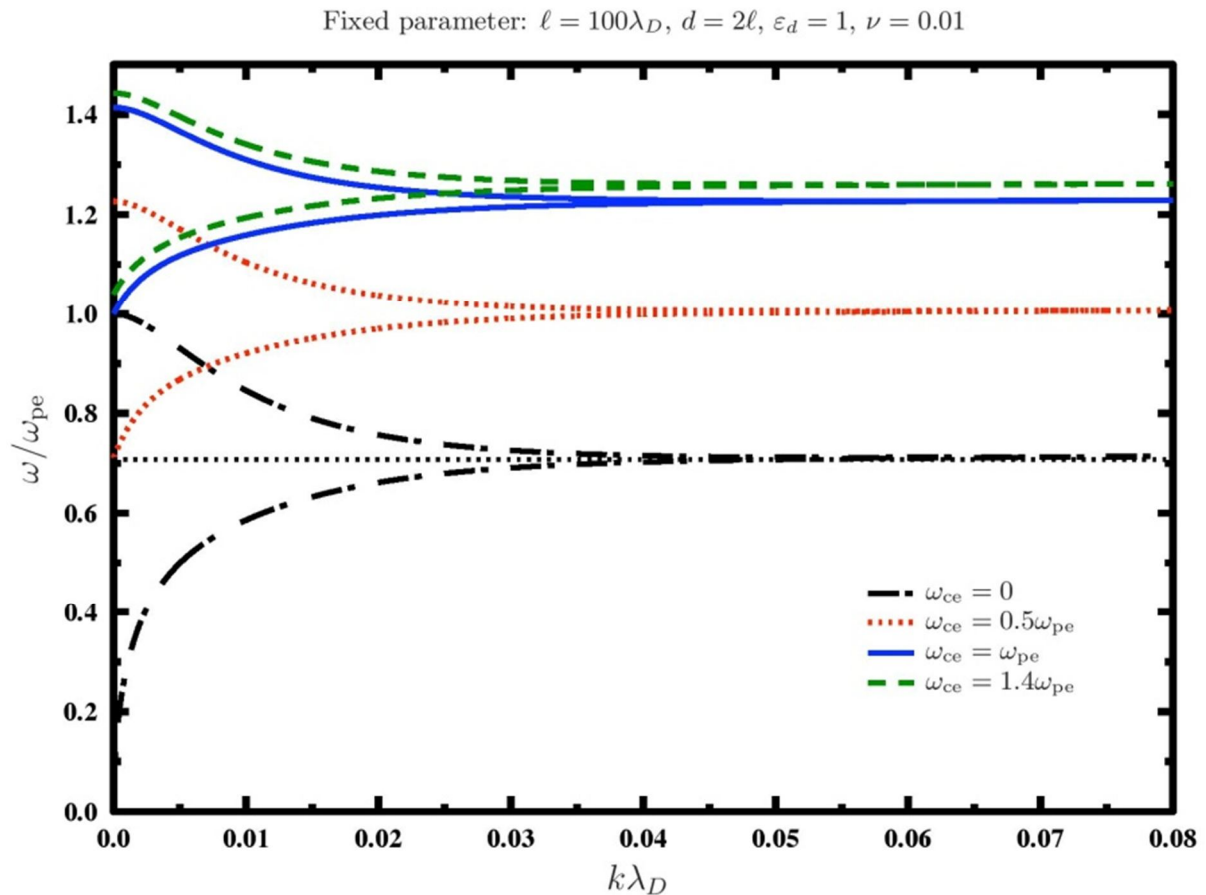


FIG. 2. Coupled plasma modes for different magnetic fields.

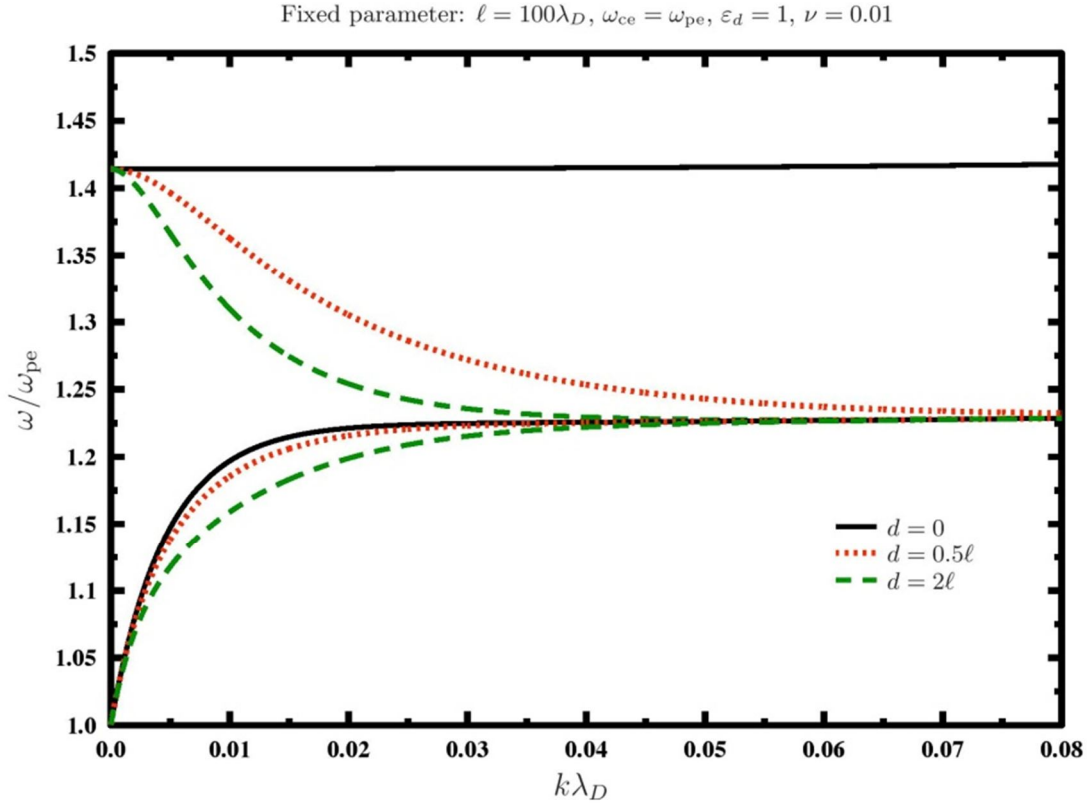


FIG. 3. Coupled plasma modes for different central slab thicknesses.

The existence of these upper hybrid frequencies has been verified experimentally by studying the microwave transmission across a magnetic field. As the plasma density is varied, the transmission through the plasma exhibits a dip at the density value that makes ω_{uh} equal to the applied frequency: upper hybrid oscillations are excited, and energy is absorbed from the beam.

4. Discussion and Conclusions

This work has been devoted to the investigation of the coupling of electrostatic surface magnetoplasma modes supported by two identical parallel plasma slabs separated by a vacuum slab. The general characteristics for the surface magnetoplasma modes are obtained by simultaneously solving the homogeneous system of Eqs. (12-19) together with Eq. (5). The normalized mode frequencies ω/ω_{pe} have been plotted versus $k\lambda_D$ in the range of the validity of the warm plasma approximation $k\lambda_D \ll 1$. A numerical value of the collision frequency with neutral $\nu = 0.01$ keeps the magnetoplasma slabs non-collisional. It is well known in literature that the effect of collisions is to down shift the

surface wave spectra and the corresponding quasi-static resonance frequency [15, 25].

The curves in Figs. 2 show the existence of backward and forward propagating electrostatic modes for $\omega_{ce} = 0$ or $\omega_{ce} \neq 0$. The backward mode emerges at $\omega = \omega_{uh} = \sqrt{\omega_{pe}^2 + \omega_{ce}^2}$, which reduces to $\omega = \omega_{pe}$ for unmagnetized plasma. The second mode is a forward propagating mode, which emerges at a lower value $\omega = \omega_{uh} - \omega_{pe}$ and becomes $\omega = 0$ in the absence of the dc-magnetic field [13, 15].

Backward and forward electrostatic magnetoplasma surface modes for different values of d/ℓ at fixed value $\omega_{ce} = \omega_{pe}$ are shown in Fig.3. When the central vacuum slab is absent ($d = 0$), the magnetoplasma slab supports two uncoupled modes at $\omega = \omega_{uh} = 1.4\omega_{pe}$ and $\omega = \omega_{pe}$. For $d \neq 0$, the bulk upper hybrid mode at $\omega = \omega_{uh} = 1.4\omega_{pe}$ and the bulk plasma mode at $\omega = \omega_{pe}$ become coupled and approach the upper hybrid quasi-static resonance value $\omega = \omega_{uh}/\sqrt{2} = 1.22\omega_{pe}$.

References

- [1] Kochetkov, V.M., *Zh. Tekh. Fiz.*, 49 (1979) 679. [*Sov. Phys. - Tech. Phys.*, 21 (1976) 280].
- [2] Markov, G.A. and Khazanov, I.V., *Plasma Physics Reports*, 28 (2002) 274.
- [3] Abedi-Varaki, M., *Modern Physics Letters B*, 33 (2019) 1950267.
- [4] Abedi-Varaki, M., *Modern Physics Letters B*, 32 (2018) 1850225.
- [5] Abedi-Varaki, M., *Physics of Plasmas*, 25 (2018) 023109.
- [6] Abedi-Veraki, M., *International Journal of Modern Physics B*, 34 (2020) 2050044.
- [7] Eliasson, B. and Shukla, P.K., *Phys. Lett. A*, 312 (2003) 91.
- [8] Yin, L. and Ashour-Abdalla, M., *Phys. Plasmas*, 6 (1999) 449.
- [9] Budden, K.G. and Jones, D., *Ann. Geophys. A*, 5 (1987) 21.
- [10] Mohanty, J.N. and Naik, A., *Phys. Plasmas*, 5 (1998) 3075.
- [11] Kliewer, K.L. and Fuchs, R., *Adv. Chem. Phys.*, 27 (1974) 355.
- [12] Landau, L.D. and Lifshitz, E.M., *"Electrodynamics of Continuous Media"*, (Pergamon Press, 1960).
- [13] Boardman, A.D., *"Electromagnetic Surface Modes"*, (Wiley, New York, 1982).
- [14] Trivelpiece, A.W., *"Slow-wave Propagation in Plasma Waveguides"*, (San Francisco Press, San Francisco, 1967).
- [15] Aliev, Y.M., Schlüter, H. and Shivarova, A., *"Guided-wave-produced Plasmas"*, (Springer, Berlin, 2000).
- [16] Abdel-Shahid, N.Z. and Pakhomov, V.I., *Plasma Phys.*, 12 (1970) 55.
- [17] Lee, H.J., *Plasma Phys. Controlled Fusion*, 37 (1995) 755.
- [18] Shivarova, A. and Zhelyazkov, I., *Plasma Phys.*, 20 (1978) 1049.
- [19] Girka, O., Pavlenko, I.V. and Thumm, M., *Physics of Plasmas*, 26 (2019) 052103.
- [20] Sital, S. and Sharma, E., *Journal of Electronics and Communication Engineering*, 12 (2017) 08.
- [21] Nicholson, D.R., *"Introduction to Plasma Theory"*, (John Wiley and Sons, Inc., New York, 1983).
- [22] Chen, F.F., *"Introduction to Plasma Physics and Controlled Fusion"*, 2nd edn., (Plenum, New York, 1984).
- [23] Stix, T.H., *"Waves in Plasmas"*, (AIP, New York, 1992).
- [24] Swanson, D.G., *"Plasma Waves"*, 2nd edn., (IOP Publishing Ltd, 2003).
- [25] Al-Sharif, A.I. et al., *The Arabian Journal for Science and Engineering*, 32 (1A) (2006) 49.

Factors Motivating Virtual Lab Simulations Adoption in Secondary School Physics Instruction in Jordan

Salah M. Jaradat^a, Marwan S. Mousa^b, Donald Dunn^a and Casey Reason^a

^a Department of Education, Aspen University, Denver, CO, USA.

^b Department of Physics, Mutah University, Al-Karak, Jordan.

Doi: <https://doi.org/10.47011/14.2.7>

Received on: 14/04/2020;

Accepted on: 25/06/2020

Abstract: The study investigated the factors that motivate secondary school physics instructors to use virtual lab simulations in teaching and learning in four regions of the Hashemite Kingdom of Jordan. To examine the research question, the study utilized a quantitative survey research methodology using a survey questionnaire consisting of 25 Likert-type scale questions to measure physics instructors' attitudes toward using virtual lab simulations in practical investigations' preparation and delivery. Contrary to what might be expected, the findings came across a number of variables that were not predictors of statistical significance for a physics instructor's virtual lab simulation adoption: gender; level of education; school site; average class size; ways of acquiring technology skills, for instance, self-taught and computer courses; and perceived barriers. The findings support the prediction that the lack of virtual lab simulations in the Jordanian high-school physics curriculum has an impact on Tawjihi students' achievement in physics.

Keywords: Simulation, Virtual lab, Roger's diffusion of innovations theory.

Introduction

The study intended to discover and recommend practical solutions using physics virtual lab simulations to improve student learning and raise the Tawjihi students' scores in physics. Therefore, the study is designed to investigate the lack of physics practical investigations (real labs/ virtual lab simulations) in Jordanian secondary-school curriculum and its impact on high-school students' results [1].

Thomton and Tamir (as cited in [2]) have demonstrated that even instructors who are proficient at delivering lectures still have merely partial accomplishment in assisting students in comprehending physics utilizing this method. They have suggested that students ought to be more involved than possible throughout the lecture, even in a conventional class with a substantial number of students. Science ought to

be viewed as a subject that inspires students' inquisitiveness to be inquiring minds and that demands students to have problem-solving skills. The experimental characteristic of the subject brings about collaboration and attainment of needed manipulative aptitudes. It likewise encourages observational, inferential and appraising aptitudes (Rawer, as cited in [2]).

It is noted that Tawjihi students' achievement in physics is relatively low compared to other science subjects such as chemistry, biology and geology. Hands-on experiments or virtual labs enable students to be active learners at the focal point of learning process rather than being passive learners receiving all the information from their teachers. Table 1.1 shows the mean success rates in science subjects from 2016-2019 for summer sessions in four cities in the

Hashemite Kingdom of Jordan: Irbid, Al-Karak, Zarka and Amman. The raw data was obtained from the Tests and Examination Department at

the Ministry of Education and was then analyzed by using Statistical Package for Social Science (SPSS), Version 25.0.

TABLE 1. Mean success rates in science subjects from 2016-2019.

City	Mean Success Rate from 2016-2019			
	Biology	Chemistry	Geology	Physics
Al-Karak	58.98%	85.13%	78.90%	55.93%
Amman	71.93%	81.63%	78.73%	66.60%
Irbid	71.73%	85.58%	79.25%	68.98%
Zarka	66.78%	80.53%	76.15%	62.45%

The purpose of this study was to investigate the effectiveness of integrating virtual lab simulations into the Jordanian physics curriculum to inspire secondary-school physics instructors in Jordan to include virtual lab simulations in the scope of instructional curriculum in ways that mimic traditional lab-based teaching and learning. Simulations created authentic classroom platforms that located instructors as facilitators and inspired learning to take place through student interaction with supervision from the instructor (Wieman, Adams, Loeblein & Perkins, as cited in [3]).

Literature Review

The study conceptualized the age of an instructor, teaching experience, Internet at home and school, availability of educational technology resources, perceived characteristics of technology and in-service training as independent variables. Using virtual lab simulations in teaching and learning in the four regions of the Hashemite Kingdom of Jordan is considered as the major dependent variable.

According to Ajredini, Izairi and Zajkov [4], although real investigations enable students to reflect more, especially at first, when they are required to plan the practical set up and work out practicable problems, simulations do not necessitate real design and the practical problems which are expected to be resolved are insignificant. Because simulations empower students to envision the imperceptible objects, this would yield preferable outcomes over the real investigations. Simulations are exceptionally effectual for assisting students in comprehending the theoretical and unjustified conceptions of specific topics of physics, since they can visualize, interact and efficiently exploit computations while using the simulations (McKagan et al., as cited in [4]).

According to Fan, Geelan and Gillies [5], several studies demonstrated that computer simulations reveal a substantial increase in strengthening the growth of students' abstract comprehension and advancing students' extrapolative aptitude as well. Easy Java Simulation (EJS) demonstrated proof of improving students' physics abstract learning. These simulations involve students in an inquiry-based learning process to assist them in attaining abstract comprehension and enhancing their inquiry aptitudes. When students utilize Physics Education Technology (PhET) simulations to examine their hypotheses, kinetic movements; pictures; graphs and tables displayed on the PC interface along with the printed words on textbooks assist in scaffolding students' comprehension. Utilizing PhET simulations, instructors are provided with more time to monitor students' learning rather than concentrating on students' security in the labs. To sum up, learners studying with the Interactive Simulations Instructional Approach (ISIA) model utilizing interactive simulations gain knowledge more efficiently than learners utilizing traditional education. This result was strong across both genders and all scholastic accomplishment levels [5].

Price, Wieman and Perkins [6] indicated that physics instructors utilizing PhET simulations as a demonstration tool are able to situate the exact scenarios they want for their students to observe while enabling the students to check their predictions from the supplementary clicker questions. According to Gasparella [7], physics simulation tools help students achieve higher understanding of the details of the physical procedures concerned, better comprehension of the modeling methodologies and their employment and a perception into all the simulation measures, their significance, consequences and progression.

Mourad and Mohamed [8] indicated that simulation engineering is a promising field that employs both simulation science and engineering fields to deal with numerous complicated real-world problems through a modeling activity that models physics phenomena and a simulation activity that achieves more awareness of phenomena, predictions and implementation study.

The theoretical framework of the study is based on Roger's Diffusion of Innovations (DOI) theory. According to Freeman and Mubichi [9], the Diffusion of Innovation (DOI) theory analyzes how and why choices to embrace a modern technology happen. Roger (as cited in [9]) described diffusion as the procedure by which an advancement moves in the bounds of a social framework in a short time. While an advancement frequently alludes to physical bodies, it can as well incorporate thoughts, practices or practices that are new to the people in the bounds of a framework [9].

Nan, Zmud and Yetgin [10] indicated that there are four fundamental components of diffusion of innovation: an innovation (thought, practice or object), communication channels (to transfer data from one individual to another), time (including three elements: innovation decision time, relative time with which an innovation is embraced and the innovation's percentage of embracing) and the social system (a group of interconnected individuals that are involved in common problem-solving to achieve a mutual objective). In a diffusion of innovation setting, social network content is exemplified by three innovation-associated indicators. These indicators can appear as data in regard to perception (the presence of an advancement), inspiration (convictions about potential benefits to be acquired from embracing an advancement) and aptitude (information associated with comprehending and employing an advancement) [10].

In this regard, the following research question was proposed:

Q: What are the varying factors that encourage secondary-school physics instructors to use virtual lab simulations in teaching

and learning in the four regions of the Hashemite Kingdom of Jordan?

Methods

Participants and Setting

The participants in the current study were 120 (60 male and 60 female) high-school physics instructors within the age range of 20-60. The participants work at public high schools in the four cities in the Hashemite Kingdom of Jordan: Irbid (northern region), Al-Karak (southern region), Zarka (eastern region) and Amman (western region).

Instrumentation

The instrument used in this study was a Physics Teachers' Survey (PTS) questionnaire consisting of 25 Likert-type scale questions to measure physics instructors' attitudes toward using virtual lab simulations in physics instruction.

Data Collection

Data collection of the study included a quantitative technique that made use of a questionnaire survey tool. The questionnaire forms were distributed in person and electronically using Google Forms through the Jordan Physics Teachers Forum in order to reach as many physics teachers as possible to fill out the questionnaire. The collected data was entered in a Microsoft Excel spreadsheet and then exported to Statistical Package of Social Sciences (SPSS), Version 25.0 necessary for multiple regression analysis.

Results

Table 2 introduces instructor gender and age groups. Table 3 shows the highest completed education degree and high-school physics teaching experience. Table 4 shows the school features that were gathered in the study. School features incorporated Internet access availability and places as well as the classroom computer availability. Table 5 shows the findings of the multiple regression analysis that were described depending upon the unstandardized regression coefficient B, standardized regression coefficient β , 95% confidence interval and statistical significance.

TABLE 2. Socio-demographic profile of instructors in sample ($N_{\text{Total}} = 120$).

Socio-demographics		N	%
Gender	Male	60	50.0
	Female	60	50.0
	Total	120	100.0
Age Group	20-30 years	16	13.3
	31-40 years	52	43.3
	41-50 years	36	30.0
	51-60 years	16	13.3
	Total	120	100.0

TABLE 3. Characteristics of instructors surveyed.

Teaching Characteristics		N	%
Highest Completed Education Degree	Teacher college diploma	1	0.8
	Bachelor's degree	89	74.2
	High diploma after bachelor	2	1.7
	Master's degree	27	22.5
	Doctorate (Ph.D. or Ed. D.)	1	0.8
Total		120	100.0
High-school Physics Teaching Experience	3 years or more but less than 10 years	45	37.5
	10 years or more but less than 15 years	28	23.3
	15 years or more but less than 20 years	18	15.0
	20 years or more	29	24.2
Total		120	100.0

TABLE 4. School features.

School Features		N	%
Internet Access Availability and Places	Yes: Home	54	45.0
	Yes: School	3	2.5
	Yes: Both	61	50.8
	I do not use it	1	0.8
	No	1	0.8
Total		120	100.0
Classroom Computer Availability	Laptop	1	0.8
	No	119	99.2
	Total	120	100.0

TABLE 5. Outline of the model parameters.

Predictor Variables	Model Parameters							
	Unstandardized Coefficients		Standardized Coefficients	t	Sig.	95.0% Confidence Interval for B		
	B	Std. Error	Beta (β)			Lower Bound	Upper Bound	
Socio-demographics								
	(Constant)	7.004	0.429		16.334	0.000	6.155	7.853
1	Teacher's age group	-0.529	0.209	-0.305	-2.531	0.013	-0.943	-0.115
	Teaching experience	0.473	0.154	0.370	3.064	0.003	0.167	0.779
Technology Resources								
	(Constant)	5.791	0.687		8.426	0.000	4.429	7.152
2	Internet access availability and places	0.345	0.135	0.225	2.551	0.012	0.077	0.612
	Availability of educational technology resources	0.163	0.183	0.081	0.889	0.376	-0.200	0.525
Technology Training								
	(Constant)	4.911	0.778		6.308	0.000	3.368	6.453
3	In-service training	0.297	0.223	0.129	1.331	0.186	-0.145	0.738
	Perceived characteristics of technology	0.178	0.117	0.139	1.528	0.129	-0.053	0.410

Discussion

After analyzing the data collected from the (PTS) survey by using Statistical Package for Social Science (SPSS), Version 25.0, the following socio-demographic profile (Tables 2 & 3) of physics instructors was made. The sample consisted of 60 female instructors (50%) and 60 male instructors (50%) as well. Age group was the second socio-demographic parameter, with the uppermost consideration of instructors lying in the 31–40 (43.3%) year range.

Most of the instructors were categorized into young adults. Probable explanations involve lowering the optional retirement age of public-school instructors from 60 years to 55, high teacher turnover rates and instructors moving into administrative roles and responsibilities. A bachelor's degree was the prevailing level of education achieved by 89 physics instructors in this sample (74.2%). Just one instructor informed an achieved doctorate. The Jordanian Ministry of Education requires instructors to hold a bachelor's degree in physics to tutor in secondary schools. This qualification

condition could account for the great number of instructors with a bachelor's degree in the sample. High-school physics teaching experience ranged from 3 to more than 20 years, with the greater part of physics instructors having tutored 3–10 years (37.5%). The 3–20 year category signified 75.8% of the sample. Physics instructors who tutored 15–20 years could have moved into administrative roles and so they could be more probable to avoid responding to a random survey. Having instructors with 3–10 years in the classroom can make the instruction setting more constructive, as these instructors are supposed to be better equipped to manage classroom matters; for example, discipline and lesson preparation and delivery.

The school features (Table 4) incorporated Internet access availability and places and classroom computer availability as well. Internet access in schools was rated poorly (2.5%) and only one classroom had a computer (0.8%). Yet again, low Internet access and providing classrooms with a computer may have to do with the Jordanian Ministry of Education dinars available particularly to support computer technology in schools and to adopt virtual lab

simulations in teaching and learning. If schools lack computer resources, using computer technology for lesson planning and preparation in addition to accommodating students' personal learning styles become exceptionally complicated, if not impossible.

Table 5 shows that the 95% confidence intervals for each of the six predictor variables did not comprise zero and consequently, in 95% of the chosen sample, the interval estimate involved the true population parameter. This indicates that the six predictors can precisely predict future virtual lab simulation adoption. The multiple regression analysis gave rise to the better statistical model. Two of the six variables, teacher's age group and teaching experience, served as controlled variables. Concentrating on the association between each predictor variable and virtual lab simulation adoption; teacher's age group and teaching experience significantly predicted virtual lab simulation adoption while Internet access availability and places, perceived characteristics of technology, in-service training and availability of educational technology resources moderately predicted virtual lab simulation adoption.

Raising one unit in each one of the six predictor variables produced a percentage variation in virtual lab simulation adoption by means of the following: teaching experience ($\beta = 0.370$), teacher's age group ($\beta = -0.305$), Internet access availability and places ($\beta = 0.225$), perceived characteristics of technology ($\beta = 0.139$), in-service training ($\beta = 0.129$) and availability of educational technology resources ($\beta = 0.081$). The overall regression model explained 17.2% (which is of a medium effect as indicated by Cohen's conventions) of the predicted variation in the physics instructors' virtual lab simulation adoption. The estimated R^2 was 12.7%. Obviously, the two values were not significantly different, which implied that virtual lab simulation adoption was quite verified by the predictor variables in the multiple regression model.

These findings imply that teaching experience of all physics instructors and teacher's age group, apart from their school sites, have to be borne in mind as a main concern throughout the integration of virtual lab simulations in schools. Pre-service teacher training programs should incorporate technology training to make sure that younger physics instructors graduating

from college are provided with sufficient technology skills for teaching physics.

The study indicated that teacher's age group, Internet access availability and places, perceived characteristics of technology and in-service training may result in higher physics instructors' virtual lab simulation adoption and may influence students optimistically and inspire instructors to incorporate virtual lab simulations in their instruction approach. Teaching experience was the strongest predictor of the physics instructors' virtual lab simulation adoption in teaching physics in the four regions of the Hashemite Kingdom of Jordan: Irbid, Al-Karak, Zarka and Amman. Nevertheless, there are other means where teachers can acquire technology; for instance, computer courses and being self-taught were not predictors of statistical significance for virtual lab simulation adoption and thus, they were not incorporated in the regression analysis model. It should be noted that perceived barriers variable was not a predictor of statistical significance for the physics teachers' virtual lab simulation adoption due to its very low beta ($\beta = -0.013$). Therefore, this variable was excluded from the regression analysis model.

Conclusion

This research study provided information about what contributed to successful adoption of virtual lab simulations in particular, for the improvement of physics instruction in public secondary-school classes in Jordan. Implications for policy and practice handle two major issues: supplying technology-based training (TBT) and supplying technology infrastructure and resources.

1. Supplying technology-based training (TBT)

The existing study demonstrates that in-service training of physics instructors is a considerable factor that persuades whether instructors employ computer technology or not in physics instruction. The suggested training would incorporate certified technology courses at the Queen Rania Teacher Academy (QRTA) paid for by the Ministry of Education. At the present time, Jordanian instructors get training during school holidays, which is insufficient to coach instructors who have no earlier knowledge with technology to recognize it and understand the way to employ it in physics instruction. Accordingly, the suggested training must be

provided with sufficient full-time study leave or as on-site workshops, so that instructors can be given chances to put into practice in the classrooms. Computer technology training for physics instructors must focus not only on Microsoft Office and Internet skills, but also on cutting-edge physics software such as COMSOL Multiphysics® software, Algodoo, Circuit Shop, Interactive Physics, Maplesoft, Solve Elec and Virtual Physical Laboratory (VPL). Instructor training must exceed training centers and must track the instructors in their classrooms by assigning mentor instructors and technical assistance to report on and assist them in the course of technology adoption procedure. Moreover, those instructors who achieve successful technology training courses' completion must be offered awards and incentives, appreciated and highly praised so as to inspire and persuade other instructors to attend training workshops to learn technology.

2. Supplying technology infrastructure and resources

The findings showed that instructors frequently encounter difficulties in employing technology in their lessons due to the deficiency of technology resources. Therefore, classrooms must be outfitted with technology resources and Internet connectivity, so that instructors can use virtual lab simulations to expand students' achievement. In addition, the government must provide low-priced smart phones and laptops for instruction and make internet access more reasonably priced and accessible at homes and schools. Since not all instructors can manage to pay for technology, instructors must be offered incentives and subsidies to purchase personal

technology in order to support technology adoption in physics instruction and to guarantee conformity.

The findings of the study may be beneficial to the educational community:

- Physics instructors who do not incorporate the real/virtual practical work in their teaching may improve their students' critical thinking, theoretical comprehension of high-school physics and lab experience by bringing about an interactive classroom setting through using virtual labs;
- Queen Rania Teacher Academy (QRTA), as a teachers' training institution, might be authorized to make an educational decision to modify their training methodologies and lay emphasis on practical investigation;
- Curriculum developers in the Jordanian Ministry of Education (MOE) may make use of the results of the study to change their methodology in designing the physics curriculum and integrating more practical investigations into it; and
- Examiners in the MOE may require to modify the high-school physics external examinations by adding a practical exam to assess the practical skills and acquisition procedures.

Acknowledgements

We are thankful to the physics instructors of the Jordanian schools who participated in this study. Their cooperation was a valuable tool in this investigation.

References

- [1] Al-Hawamdeh, A.M., *European Journal of Training and Development Studies*, 5 (2), (2018) 1.
- [2] Musasia, A.M., Ocholla, A.A. and Sakwa, T.W., *Journal of Education and Practice*, 7 (28) (2016) 129.
- [3] Agyei, E.D., Jita, T. and Jita, L.C., *Journal of Baltic Science*, 18 (6) (2019) 816.
- [4] Ajredini, F., Izairi, N. and Zajkov, O., *European Journal of Physics Education*, 5 (1) (2014) 59.
- [5] Fan, X., Geelan, D. and Gillies, R., *Education Sciences*, 8 (1) (2018) 29.
- [6] Price, A., Wieman, C. and Perkins, K., *The Science Teacher*, 86 (7) (2019) 46.
- [7] Gasparella, A., *Applied Mechanics and Materials*, 887 (2019) 117.
- [8] Mourad, M. and Mohamed, B., *Informatica*, 43 (1) (2019) 53.
- [9] Freeman, K. and Mubichi, F., *Journal of Rural Social Sciences*, 32 (2) (2017) 1.
- [10] Nan, N., Zmud, R. and Yetgin, E., *Computational and Mathematical Organization Theory*, 20 (1) (2014) 52.

Fullerite Nano-materials as a Moderator in Neutron Irradiators with Radium Sources: Feasibility and Advantages

F. Qamar and M. Nahili

Physics Department, Faculty of Sciences, Damascus University, Damascus, Syria.

Doi: <https://doi.org/10.47011/14.2.8>

Received on: 24/04/2020;

Accepted on: 25/06/2020

Abstract: In this study, the feasibility of using fullerite nano-materials as a moderator in ^{226}Ra -Be neutron irradiators has been theoretically investigated, for the first time. Thermal, intermediate and rapid neutron flux in irradiation channels was calculated using the MCNP5 code when a fullerite nano-material was used as a moderator. The simulation results were then compared with other simulation results performed when paraffin was used as a moderator. The comparison showed that using fullerite instead of paraffin as a moderator results in an increase in the total number of irradiation neutrons by more than twice in average (240 %) for each direction inside the irradiator. This increase is distributed as follows: 27.84 %, 87.84 % and 124.32 % thermal, intermediate and rapid neutrons, respectively. The previous distribution indicates a significant increase in the intermediate and fast neutron flux. This is considered as an additional advantage of using the ^{226}Ra -Be neutron irradiator with a fullerite moderator. The irradiator can then be used not only to irradiate the materials whose irradiation requires thermal neutrons, but also those that require medium- to high-energy neutrons.

Keywords: Neutronic irradiator, Ra-Be radiation source, Cadmium, Neutron flux, MCNP5-beta code.

PACS: Neutrons diffusion and moderation, 28.20.Gd, Moderators (nuclear reactors), 28.41.Pa.

Introduction

Many countries began applying nanotechnologies in the nuclear industry since the 1970s [1, 2], which included: reactor moderators [3], high-density nuclear fuel with nanotechnology additives [4] and the activation of thermal hardening processes by nanotechnology additions as one of the trends in technology innovation for new types of nuclear reactor fuel, such as plutonium oxides, uranium and nitrides for fast novel neutron reactors [5]. In recent years, the discovery of a new form of carbon nano-particle called fullerenes has attracted the interest of researchers to gain new basic knowledge of matter and the potential for its practical implementing applications [6].

Fullerenes are carbon molecules forming pentagonal and hexagonal rings and this term is currently applied to a broad class of atomic carbon molecules of general formula C_n (n even) that have a closed hollow polyhedron shape [7]. The most famous fullerenes are C_{60} and C_{70} . Other fullerene molecules that contain different numbers of carbon atoms from 36 to 540 and more have been manufactured and studied [7]. Among all known fullerene molecules, the C_{60} molecule is the most symmetrical molecule to date. It consists of sixty carbon atoms located on a spherical surface with a diameter of ~ 1 nm, as shown in Fig. 1.



FIG. 1. Fullerene molecule for C_{60} .

C_{60} molecules are arranged spatially under certain conditions, where they are placed in crystal lattice nodes. Structures of a solid phase formed on the basis of fullerene molecules are called fullerites [8]. The C_{60} fullerite crystal has a FCC type cubic mesh structure with a constant value of 1.42 nm, while its density is $1.65 \pm 0.03 \text{ g/cm}^3$ indicating a stable substance in the air. It does not dissolve and does not degrade even, after which it begins to sublime. Fig. 2 shows the lattice structure of a C_{60} crystal, where C_{60} molecules are mainly bound in the crystal by the van der Waals forces [8].

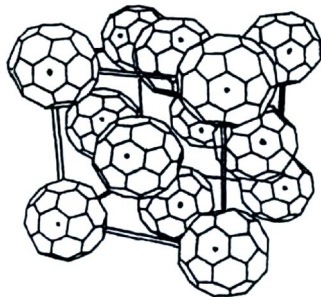


FIG. 2. C_{60} crystalline lattice structure.

Fullerite moderator was used with U^{235} to produce a homogeneous subcritical nuclear reactor [9]. According to the authors of [9], the reactor becomes subcritical when the fullerite moderator is transformed into a diamond-like form under pressure.

In this research, the feasibility of a use of fullerite nano-material as a moderator in $^{226}\text{Ra-Be}$ paraffin neutron irradiators has been investigated, for the first time. The viability of using fullerite nano-material moderator was demonstrated theoretically by using the MCNP5 code [10]. It can be used to calculate neutron flux values in each irradiation channel of $^{226}\text{Ra-Be}$ irradiator available at the Physics Department of the Faculty of Science, Damascus University. The neutron flux was calculated in two conditions. These are when paraffin and then fullerite nano-material was used as a neutron moderator. Neutron flux in each irradiated channel of the two studied states was then compared.

Modeling of $^{226}\text{Ra-Be}$ Irradiator

The $^{226}\text{Ra-Be}$ irradiator is one of the isotopic neutron irradiators that are used to obtain fast, intermediate and thermal neutron flux. The irradiator was made by the PHYWE German company. It consists of an isotope source $^{226}\text{Ra-Be}$ and a paraffinic moderator surrounded by a 4 mm thick parallelepiped steel container of dimensions $50 \times 50 \times 60 \text{ cm}^3$. The container is covered with a rectangular steel lid. The moderator in its turn contains ten cylindrical irradiation channels and a rectangular gap that is dedicated to insert a cadmium plate. Each channel is surrounded by a 1 mm thick and 2.2 cm diameter steel liner. The rectangular gap is also surrounded by a 1 mm thick steel liner. Five of the ten irradiation channels are distributed around the $^{226}\text{Ra-Be}$ neutron source on the circumference of a 10 cm radius. Three of the remaining five channels are situated on the ox axis at 15, 20 and 25 cm away from the source. The last two channels are located at diagonal distances of 20 and 25 cm from the radium-beryllium source. Positions of the irradiation channels, the cadmium plate and the $^{226}\text{Ra-Be}$ neutron source are shown in Fig. 3 and described in Table (1).

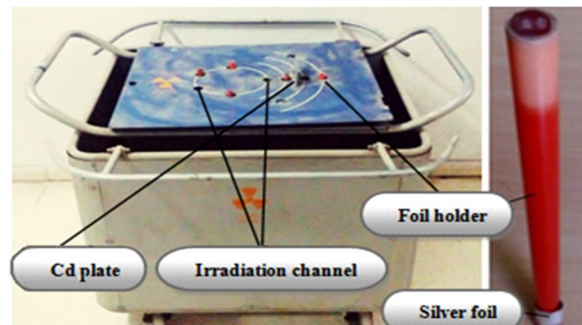
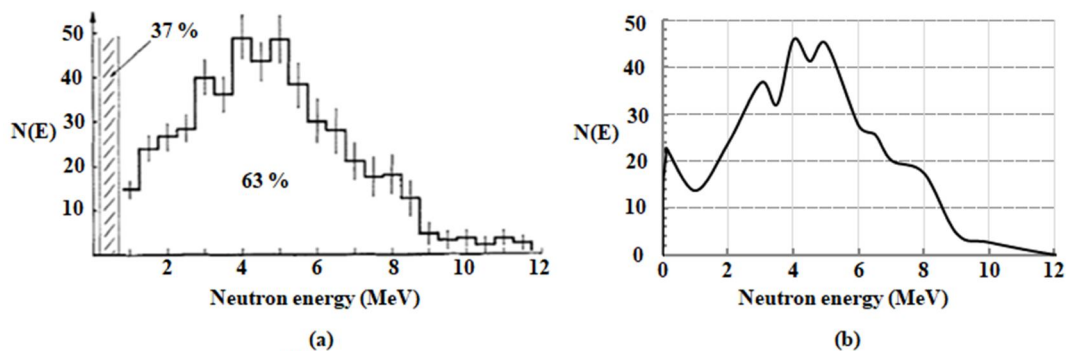


FIG. 3. $^{226}\text{Ra-Be}$ paraffinic neutron irradiator.

The $^{226}\text{Ra-Be}$ neutron source consists of a homogeneous mixture of the ^9Be and ^{226}Ra isotopes, where beryllium forms most of its material (Ra to Be ratio is 1/5). The mixture weight and the source's activity are 3.5 mg and $9.09 \times 10^4 \text{ n/s}$, respectively. The $^{226}\text{Ra-Be}$ neutron source is surrounded by a 7 cm length and 2 cm diameter double-walled nickel-steel cylindrical tube. The tube was itself surrounded by a 7 cm length and 4 cm diameter cylindrical lead. Fig. 4 illustrates (a) the spectrum of the neutron source $^{226}\text{Ra-Be}$ according to reference [11] and (b) the spectrum from which values used in the simulation of this research were obtained.

TABLE 1. ^{226}Ra -Be radioactive physical properties that have been applied in the simulation with MCNP5 code.

Name	Shape	Name	Distance from ^{226}Ra -Be source (cm)	Notice
Steel container	Parallel rectangles	Steel container		Contains paraffin moderator
Cadmium	Plate	Cadmium	17.5	On ox axis
Channel number	Distance of 2 cm diameter cylindrical irradiation channels from ^{226}Ra -Be source (cm)			
1		10		On oy axis
2		10		On ox axis
3		-10		On oy axis
4		-10		In the xoy plane
5		-10		In the xoy plane
6		15		On ox axis
7		18.023		In the xoy plane
8		20		On ox axis
9		25		In the xoy plane
10		25		On ox axis
Sample holder	Plastic cylinder with 30 cm length and 0.5 cm radius			Length inside the paraffin is 20 cm.
^{226}Ra -Be Source				
^{226}Ra -Be mixture weight	3.5 mg	The mixture is housed within a double-walled nickel-steel cylindrical tube with 7 cm length and 2 cm diameter.		
^{226}Ra to ^9Be ratio	1/5			
Lead barrier	Cylinder with 7 cm length and 2 cm diameter surrounds the tube.			
Lead holder	Cylinder with 18 cm length and 4 cm diameter.			

FIG. 4. Neutrons spectrum of ^{226}Ra -Be source (a) according to reference [11] and (b) the values used in the simulation.

MCNP5 code was used to model ^{226}Ra -Be paraffinic irradiator. This code is applied widely around the world to model neutral particle radiography, photon, electron or coupled neutron, photon and electron transport, for three-dimensional or time-dependent general geometry [10]. The ^{226}Ra -Be neutron source within the SDEF source ID card provided in the MCNP5

code has been described as a point source located at (0,0,0); the centre of the Cartesian coordinate system is supported in the modeling. The considered point source is at a 25 cm depth from the top surface of the irradiator. It is also 35 cm and 25 cm away from the right and the left irradiator surface, respectively (Fig. 5).

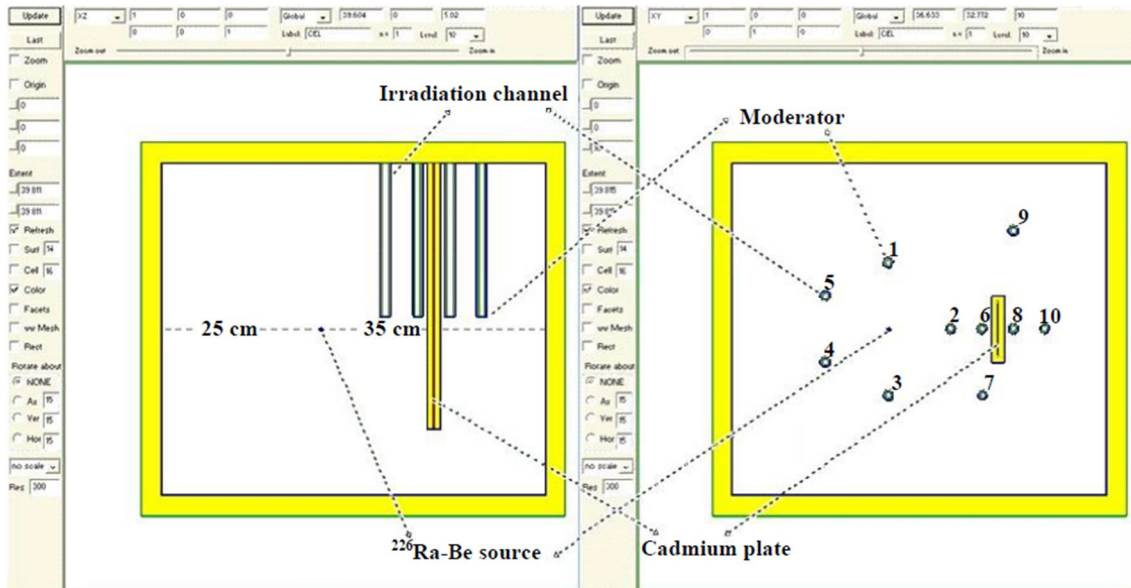


FIG. 5. Irradiation diagram for ²²⁶Ra-Be point source, moderator, irradiation channel numbers and the Cadmium plate (Cd) in the order that was used in the input entry file of the MCNP5 code.

Neutron Flux Calculation within the Irradiation Channels ²²⁶Ra-Be

The F4 (Tally) card provided in the MCNP5 code was used to compute the entire neutron flux in each channel using: 1. paraffin and 2. fullerite with densities of 0.904 g / cm³ and 1.65 g / cm³,

respectively as a moderator. Fig. 6 shows the variation of the neutron flux in the irradiator channels for the neutron energy (calculated by MCNP5 code for each lethargy unit) when the paraffinic moderator was used.

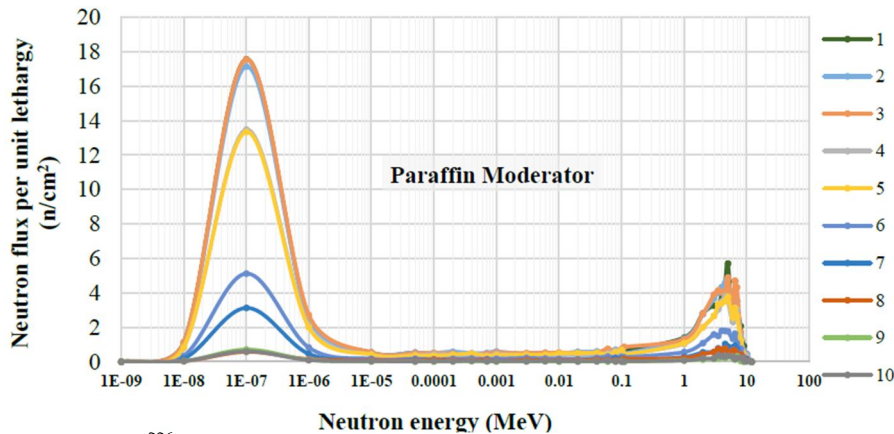


FIG. 6. Variation of the ²²⁶Ra-Be irradiator channel neutron flux for the neutron energy when the paraffin moderator was used.

Fig. 7 shows the variation of the neutron flux in the irradiator channels for the neutron energy (calculated by MCNP5 code for each lethargy unit) using the fullerite moderator.

paraffin and fullerite were used as a moderator for neutrons. The cadmium plate absorbs the thermal neutrons to produce fast neutrons. This reduces the thermal neutron flux in the irradiation channels behind it.

Fig. 8 shows a comparison of average neutron flux rate in all ten irradiation channels shown in Figs. 6 and 7 with paraffin and fullerite as moderator, respectively.

Fig. 10 shows a comparison of the total neutron flux in each of the ten irradiation channels separately for the use of paraffin and fullerite as a neutron moderator.

Fig. 9 shows a comparison of average neutron flux rate in the cadmium plate where both

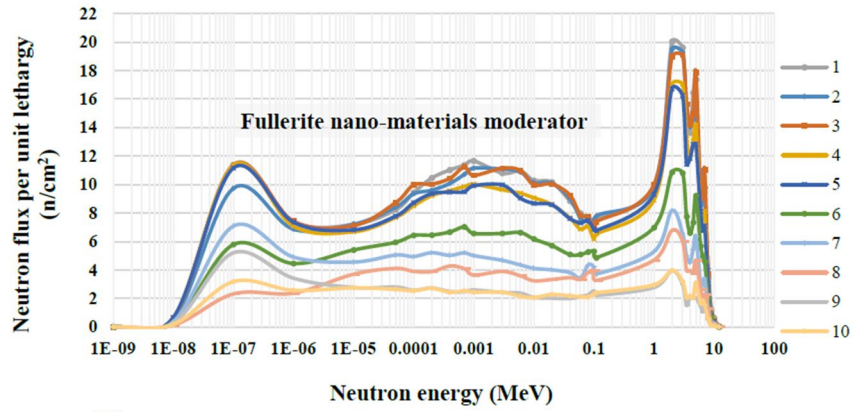


FIG. 7. Variation of the ^{226}Ra -Be irradiator channel neutron flux for the neutron energy when the fullerite (C_{60}) moderator was used.

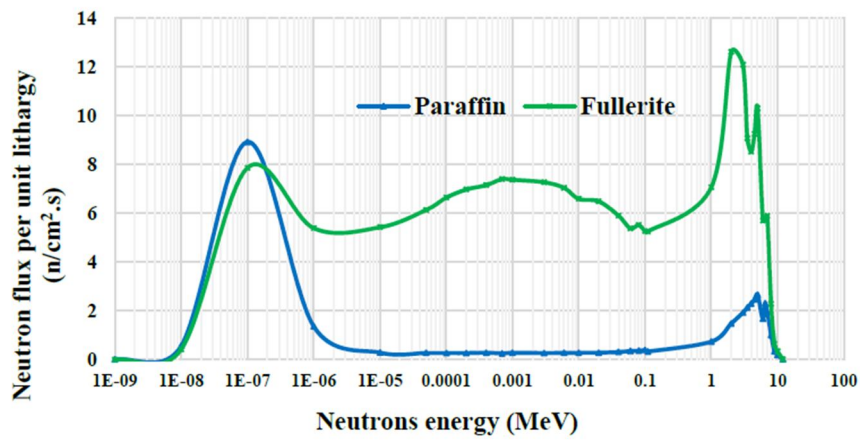


FIG. 8. A comparison of average neutron flux rate in all ten irradiation channels with paraffin and fullerite as moderator, respectively.

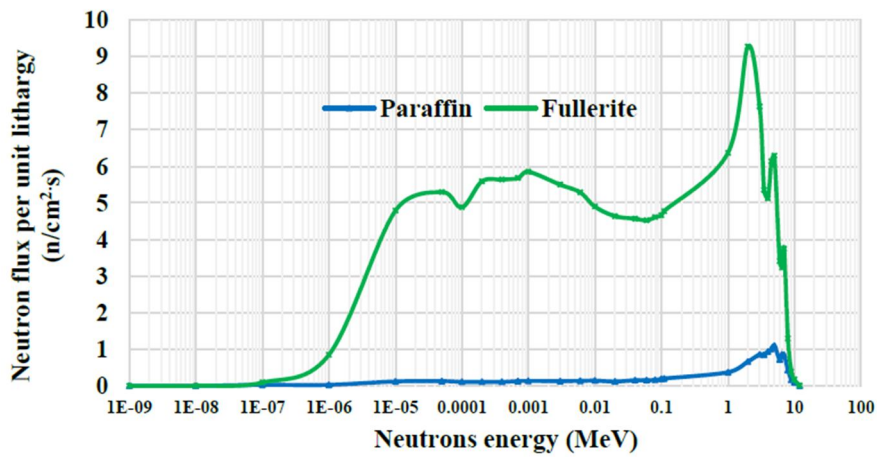


FIG. 9. A comparison of average neutron flux rate in the cadmium plate with paraffin and fullerite as moderator, respectively.

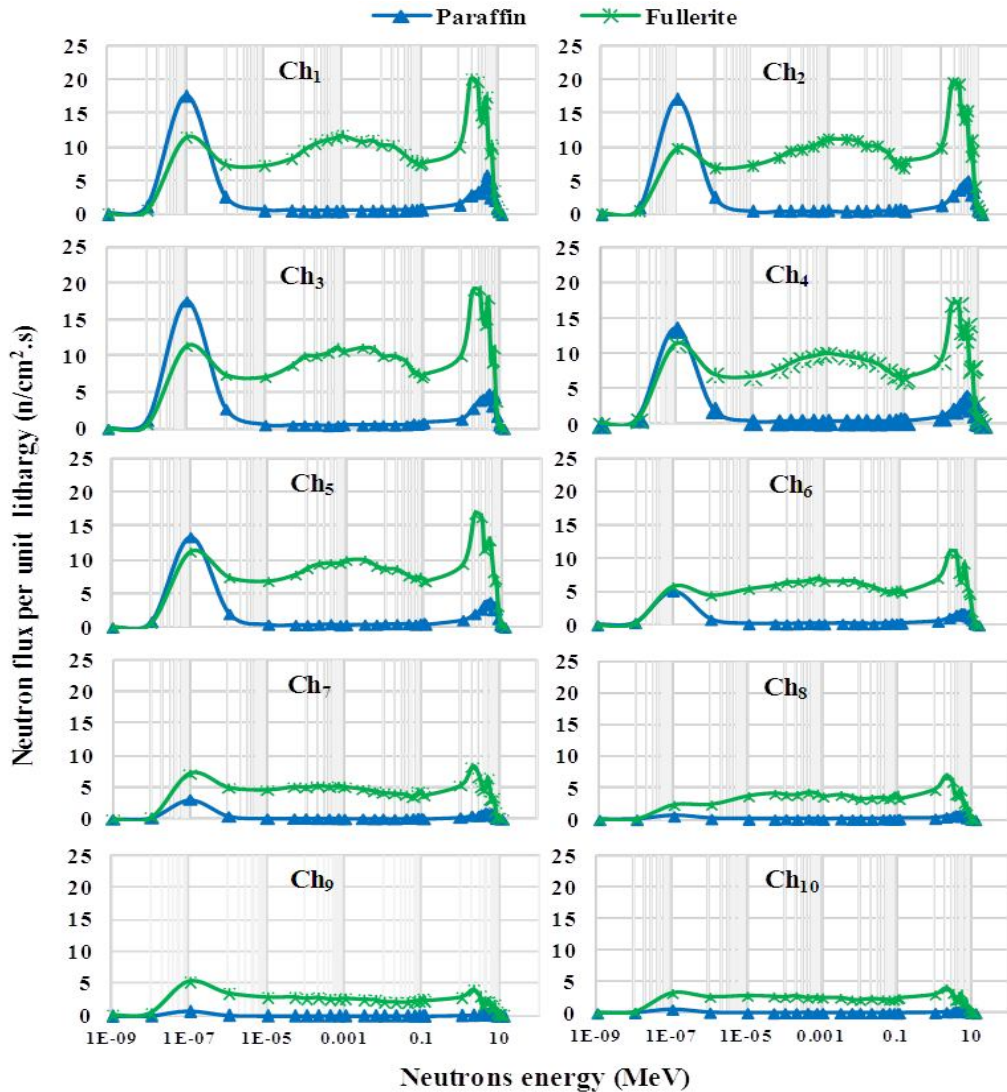


FIG. 10. Variation of the neutron flux in each channel of the ^{226}Ra -Be irradiator for the neutron energy where both paraffin and fullerite were used as neutron moderator, respectively.

Results and Discussion

Figs. 8 and 9 show that there is a significant change in the distribution of the intermediate and fast neutron fluxes in the irradiation channels and the cadmium plate for using fullerite instead of paraffin as a neutron moderator. In the intermediate energy field, it is observed that the neutron flux is virtually non-existent in all channels when the paraffin moderator is used. This is because most of the fast neutrons slow down to thermal energy within the paraffin moderator. Paraffin moderator also absorbs a large number of neutrons that pass through it. Paraffin has a high capability (cross-section) of moderating neutrons from a fast to a thermal range. It also has a large absorption cross-section for thermal neutrons, which leads to loss of a significant number of these neutrons as a result of being absorbed during the moderation

process. The intermediate neutron flux increases clearly in the case of using fullerite as a moderator and its maximum value ranges between 2 - 11 $\text{n}/\text{cm}^2\text{s}$. This indicates that a ^{226}Ra -Be irradiator with fullerite moderator can irradiate substances requiring only intermediate to fast energy neutrons, such as iron, nickel, aluminum, thorium and cobalt [12].

On the other hand, there are no significant differences in all ten irradiation channels within the thermal range between the two neutron flux curves of the fullerite and paraffin moderators. However, it can be concluded from Fig. 10 that:

1. It is preferred to use paraffin as a moderator for the channels close to the source (less than 10 cm). The peak of the thermal neutron flux for the paraffin moderator is higher in this case.

- There is no advantage in using either fullerite or paraffin moderator for the channels within a distance of 10 - 15 cm from the irradiation source. The thermal neutron flux is approximately the same for both moderators.
- It is preferred to use fullerite as a moderator for channels located at distances greater than 15 cm from the source. The thermal neutron flux in paraffin medium begins to decrease at

a distance greater than 15 cm until it practically approaches zero at a distance of 25 cm from the source.

Fig. 11 shows the variation of the thermal neutron flux as a function of the channel's distance from the irradiation source when using paraffin and fullerite, respectively, as a neutron moderator.

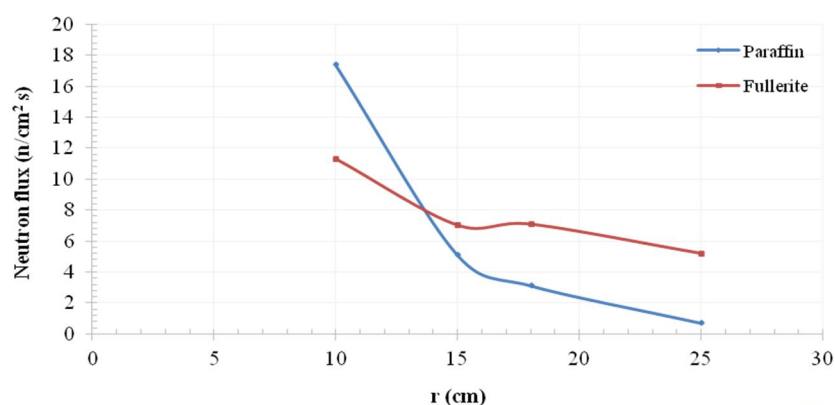


FIG. 11. Thermal neutron flux at irradiator channels according to their distance from the ^{226}Ra -Be irradiator when using paraffin and fullerite, respectively, as a neutron moderator.

Finally, It was also possible from Fig. 10 to calculate the average increase in neutron flux across the entire neutron energy range when fullerite is used instead of paraffin as a moderator. The average increase of neutron flux distributed in one direction was as follows: 27.84 %, 87.84 % and 124.32 % for the thermal, intermediate and rapid neutrons, respectively. Thus, the average total increase of the neutron flux was about 240% when replacing the paraffin as a moderator with fullerite moderator. This means that the number of irradiation neutrons rises by more than double when fullerite was used as a moderator. The simulation results, in addition to the weather and high temperature resistance of fullerite nanostructure, encourage the use of this type of moderator in radium source irradiators instead of paraffin.

Conclusion

The neutron flux in irradiation channels with fullerite as a moderator was calculated using the MCNP5 code for modeling the ^{226}Ra -Be neutron irradiator at Physics Department in the Faculty of Science at Damascus University. The neutron flux was also calculated when paraffin was used as a neutron moderator. The comparison between the calculated flux values showed some variations depending on the energy of the neutrons. The difference in the values of the thermal neutron flux also depends on the

distance of the irradiation channel from the irradiator source. The value of flux in channels close to the irradiation source (at a distance less than 10 cm), where paraffin was used as a moderator, is slightly greater than that when using fullerite as a moderator. By contrast, the thermal neutron flux value in far channels (at a distance greater than 15 cm) increases if fullerite is used as a moderator. The upshots also confirm the presence of a strong moderation of fast and intermediate neutrons with large absorption of thermal neutrons in both the paraffin and the cadmium plate when using paraffin as a moderator in contrast to the use of fullerite for moderation. Thus, using fullerite as a moderator has many advantages. First, it provides the ability to irradiate materials of various types across the entire neutron spectrum. The magnitude of the irradiation neutron flux depends on the distance of the channel from the neutron source. Second, it absorbs fewer neutrons than paraffin. Finally, it has a solid structure and withstands extreme environmental conditions of high temperature and humidity. These advantages make fullerite more suitable than paraffin to be used as a moderator. This is still factual, although the thermal neutron flux in the channels close to the source is slightly better in the presence of paraffin than the same flux in the presence of fullerite.

References

- [1] Kovtung, G.P. and Verevkin, A.A., "Nanomaterials: Technologies and Materials Science: Overview", (Kharkov: NSC KIPT, Ukraine, 2010), 73.
- [2] Azarenkov, N., Vojevodin, V., Kirichenko, V., Kovtun, G., Kurinny, V. and Lytovchenko, S., The Journal of Kharkiv National University, Physical Series "Nucleus, Particles, Fields", 1041 (2/58) (2013) 19.
- [3] Andrievski, R.A., Materials Science Forum, 555 (2007) 327.
- [4] Soudagar, M.E.M., Nik-Ghazali, N.N., Kalam, M.A., Badruddin, I.A., Banapurmath, N.R. and Akram, N., Energy Conversion and Management, 178 (2018) 146.
- [5] Silvestre, J., Silvestre, N. and de Brito, J., Journal of Environmental and Civil Engineering, 20 (4) (2016) 455.
- [6] Jeong, J., Jung, J., Choi, M, Kim, J.W., Chung, S.J., Lim, S., Lee, H. and Chung, B.H., "Advanced Materials", (WILEY-VCH Verlag GmbH & Co. KGaA, Weinheim, 2012).
- [7] Pierson, H.O., "Handbook of carbon, graphite, diamonds and fullerenes: Processing, properties and applications", (Noyes Publications: Park Ridge, New Jersey, U.S.A., 2012).
- [8] Weaver, J.H., Acc. Chem. Res., 25 (3) (1992) 149.
- [9] Gall, N.R., Physics Letters B, 560 (2003) 161.
- [10] X-5 Monte Carlo Team, "MCNP-A General Monte Carlo, N-Particle Transport Code, VERSION 5", (Diagnostics Application Group - Los Alamos National Laboratory, 2003).
- [11] Geiger, K.W., Hum, R. and Jarvis, C.J.D, Canadian Journal of Physics, 42 (6) (1964) 1097.
- [12] Coleman, R.F., Analyst, 86 (1018) (1961) 39.

Comparing of the Natural Radioactivity in Soil Samples of University at Al-Husseineya and Al-Mothafeen Sites of Kerbala, Iraq

Abrrar A. Ibrahim^a, Abdalsattar K. Hashim^a and Ali A. Abojassim^b

^a Department of Physics, Collage of Science, University of Kerbala, Kerbala, Iraq.

^b Department of Physics, Faculty of Science, University of Kufa, Al-Najaf, Iraq.

Doi: <https://doi.org/10.47011/14.2.9>

Received on: 28/05/2020;

Accepted on: 21/07/2020

Abstract: Radioactivity must be studied in soil to see the changes in the doses of human exposure. In this study, natural radioactivity and radiological hazard indices in soil samples of the Faculty of Agriculture (Al-Husseineya site) and the Faculty of Medicine (Al-Mothafeen site) in Kerbala Governorate were determined using gamma-ray spectroscopy. The results showed that the mean values of specific activity (in units of Bq/kg) and standard errors of: ²³⁸U, ²³²Th and ⁴⁰K at Al-Husseineya site was 21.7±7.2, 9.43±3.2 and 335.8±82.2, respectively, while at Al-Mothafeen site, the mean values and standard errors were 22.4±8.8, 11.2±3.3 and 333.1±70.7, respectively. Radiation maps of natural radioactivity (²³⁸U, ²³²Th and ⁴⁰K) at Al-Husseineya and Al-Mothafeen sites were mapped using geographic information system (GIS) technology. Moreover, most results in the present study fall within the acceptable levels, as defined by OCDE, UNSCEAR and ICRP. Therefore, there is no significant radiological hazard at the sites which were studied.

Keywords: Radiological hazard, Natural radioactivity, Soil, NaI (TI), Gamma-ray, Karbela University.

Introduction

Background radiation reaches us everywhere and at all times. It is an important part of our lives, where all aspects of earth's life are being subjected to ionizing radiation. Both human-made and natural radionuclides release background radiation. Natural radionuclides arise from the atmosphere due to the outer space radiation, crusts of earth including mineral rock ores and soil; or even from our bodies due to radionuclides in water and food that we intake and air that we breathe [1]. The term "NORM" indicates a material that is naturally occurring radioactive. In addition, human-made radiation comes into the environment every day from nuclear power plants, medical processes and consumer products. In general, the main radiation types are: alpha particles, beta particles and gamma rays; They often come from radionuclides [2, 3]. NORMs are divided into

two major groups. The first group is the naturally occurring radioactive materials with very long half-lives (hundreds of millions of years). These materials existed around 4.5 billion years ago; i.e., when the earth was born. These materials are called primordial radionuclides [2, 3]. They can be found in sedimentary igneous rocks and can transfer into soil, water and even through air [4]. However, the NORM of the second group is cosmogenical; it comes from the interactions between the outer atmosphere and the cosmic rays [2, 3]. It is important to investigate natural radioactivity, as the NORM can work as a good geochemical and biochemical tracer within the environment having geological events like eruptions, volcanoes and earthquakes [4]. It is well known that the biologically harmful effects occur even from exposing the body to a small amount of gamma-ray from these radionuclides

and the lung tissue irradiation from radon and its daughters' inhalation [5]. Therefore, it is very important to know the exposure dose limits for measuring the radiation level provided by air, land, food, water, buildings ... etc., in order to assess exposure and human protection regarding natural sources of radiation [6, 7]. As the soil is considered as the leading contributor to background radiation, the knowledge of its radioactivity content worldwide is quite important. The main soil's natural radioactivity arises from ^{238}U , ^{232}Th series and ^{40}K during earth creation. In Iraq and other countries, these natural radioactivities were studied utilizing various techniques, such as gamma spectroscopy [6, 7].

The main purpose of this work is to evaluate the specific activity of natural radioactivity in soil samples from the Faculty of Agriculture (Al-Husseineya site) and the Faculty of Medicine (Al-Mothafeen site) in Kerbala Governorate. Moreover, ten radiological hazard parameters were estimated, which include: Radium Equivalent Activity (R_{eq}), External Hazard Index (H_{ex}), Internal Hazard Index (H_{in}), Representation Level Index (I_{γ}), Alpha Index (I_{α}), exposure rate (\dot{x}), absorbed dose rate in the air (d), equivalent gonad dose (AGED), annual equivalent outdoor active dose and lifelong cancer risks calculated (ELCR). Finally, map of ^{238}U , ^{232}Th and ^{40}K concentrations in the present study area using GIS technique was drawn as a reference to be a base for any future studies.

Area of Study

University of Kerbala consists of many faculties distributed over three sites; namely, Frariha site, Al-Husseineya site and Al-Mothafeen site. In this work, the natural gamma radioactivity for (^{238}U , ^{232}Th and ^{40}K) was measured in soil samples that have been distributed across residency quarters that are belonging to the University of Kerbala at Al-Husseineya site and Al-Mothafeen site.

Al-Husseineya site is located between 3240'33.37"N north latitude and 4409'50.98"E east longitude. It consists of five faculties; Medicine, Dentistry, Pharmacy, Applied Medical Sciences and Nursing. Al-Mothafeen site is located between 3236'31.36"N north latitude and 4400'15.1"E east longitude. It consists of two faculties; Agriculture and Veterinary Medicine.

Materials and Methods

Sample Collection and Preparation

Forty soil samples were collected from different locations in Kerbala Governorate (Al-Husseineya site and Al-Mothafeen site) during the past year from October-November 2019 at a depth equal to (10 to 15 cm) from the earth's surface. Locations were determined using Global Positioning System (GPS) coordinates (GARMIN, Model: 010-00779-00, SKU: ETREXLEGEND) (2017) and drawn using GIS technique, as shown in Figs. 1 and 2. After collecting the soil samples, they were placed in a plastic bag and marked with the sample codes and symbols. Samples were then transferred to the laboratory of nuclear physics in the department of physics, Faculty of Science, University of Kufa. Samples were crushed and then dried inside the oven at (120) °C for (60) minutes to ensure removing any significant moisture. Then, a sieve of (500 μm) pores was used to obtain homogeneous soil samples of 0.750 kg each. Samples were then packed using one-liter plastic Marinelli cups to ensure uniformity around the detector. Plastic Marinelli cups were kept close using a proper tape and then stored for about a month prior to the counting time to permit a secular equilibrium between ^{222}Rn and ^{226}Ra in the uranium chain [8].

Experimental Setting and Measurement of Samples

The detection system (see Fig. 3) used in this work consists of a sodium iodide detector (Alpha Spectra, Inc.-12I12 / 3) with dimensions "3x3" connected to an MCA (ORTEC-Digi Base) "4096" with a high-voltage measurement scale from 0 to 1500 volts. The detector operating voltage is 787 volts. The protective cover (i.e., shielding) contains two parts: the upper one is made of lead with a thickness equal to 5 cm and 20 cm length which surrounds the crystal with a circular cover having a thickness of 5 cm and a diameter of 22 cm, while the lower part forms the base. The detector was located at the center of the chamber to minimize the influence of scattered radiation from the shield. NaI(Tl) detector was calibrated by obtaining a spectrum from radioactive standard sources of gamma-ray ^{137}Cs , ^{54}Mn , ^{60}Co , ^{22}Na and ^{152}Eu . All samples were measured for a period of 18000 sec. The MAESTRO-32 data analysis package was used

to estimate the sample specific activity which is equal to the net area below the corresponding peaks within the energy spectrum. This area was calculated by subtracting the counts owing to background sources from the area under a certain peak. An empty (1-liter) polyethylene plastic Marinelli cup was placed on the detector to measure the background spectrum for the same period of time as for the soil samples. For low gamma energies which had not well-separated photo-peaks and poor resolution of NaI(Tl) detector, activity concentration measurements

are possible if well-separated photo-peaks at elevated energies have been used, as shown in Fig. 4. In this study, the results obtained from the gamma rays emitted by the progenies of ^{232}Th and ^{238}U are in secular equilibrium with them; however, estimation of ^{40}K was direct using its gamma-line of 1460 keV. Therefore, the ^{238}U specific activity was found using the gamma-lines 1765 keV (^{214}Bi). The corresponding ^{232}Th results were estimated *via* the gamma-ray lines 2614 keV (^{208}Tl) [9].

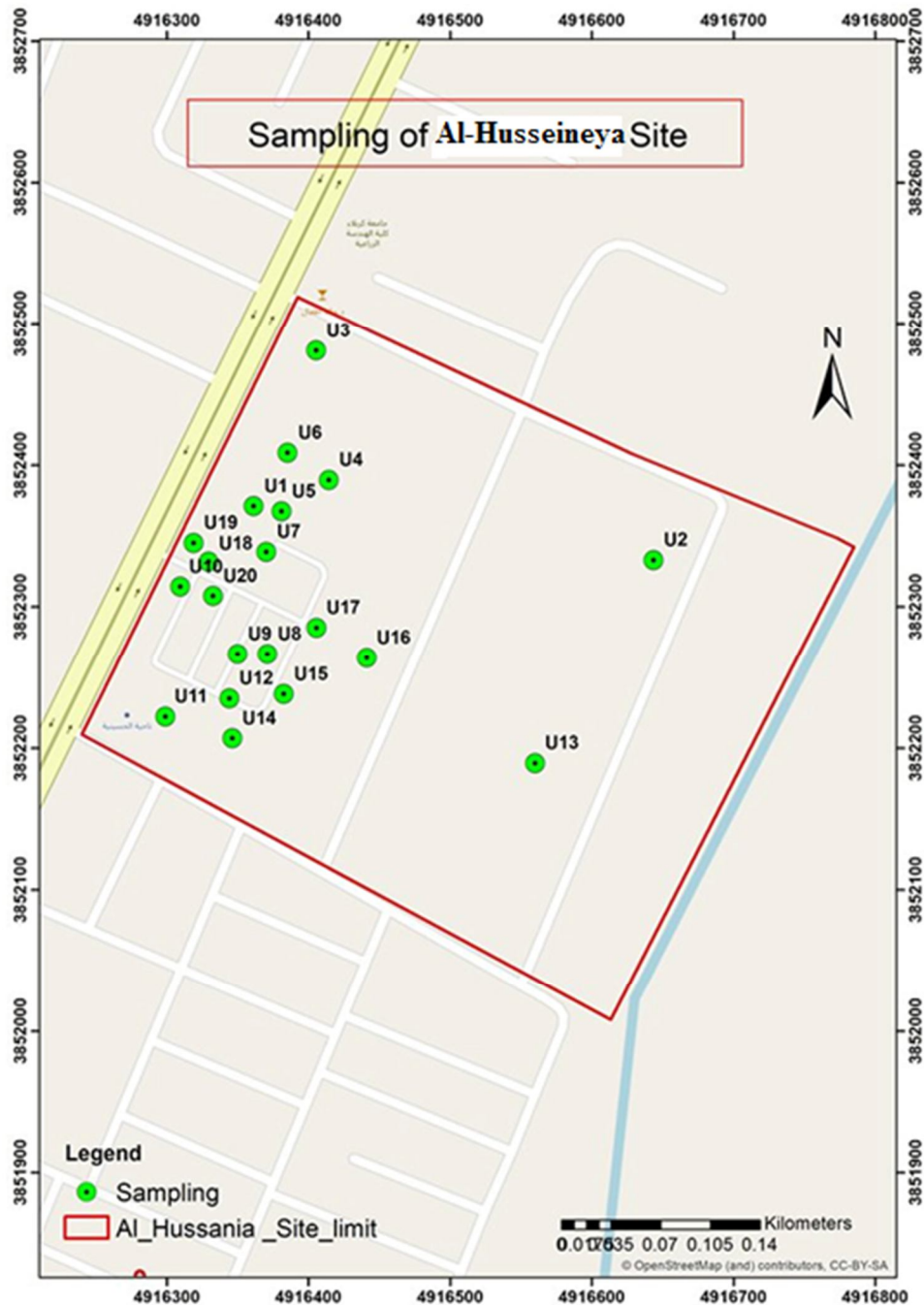


FIG. 1. Map of samples' location for Al-Husseineya site.

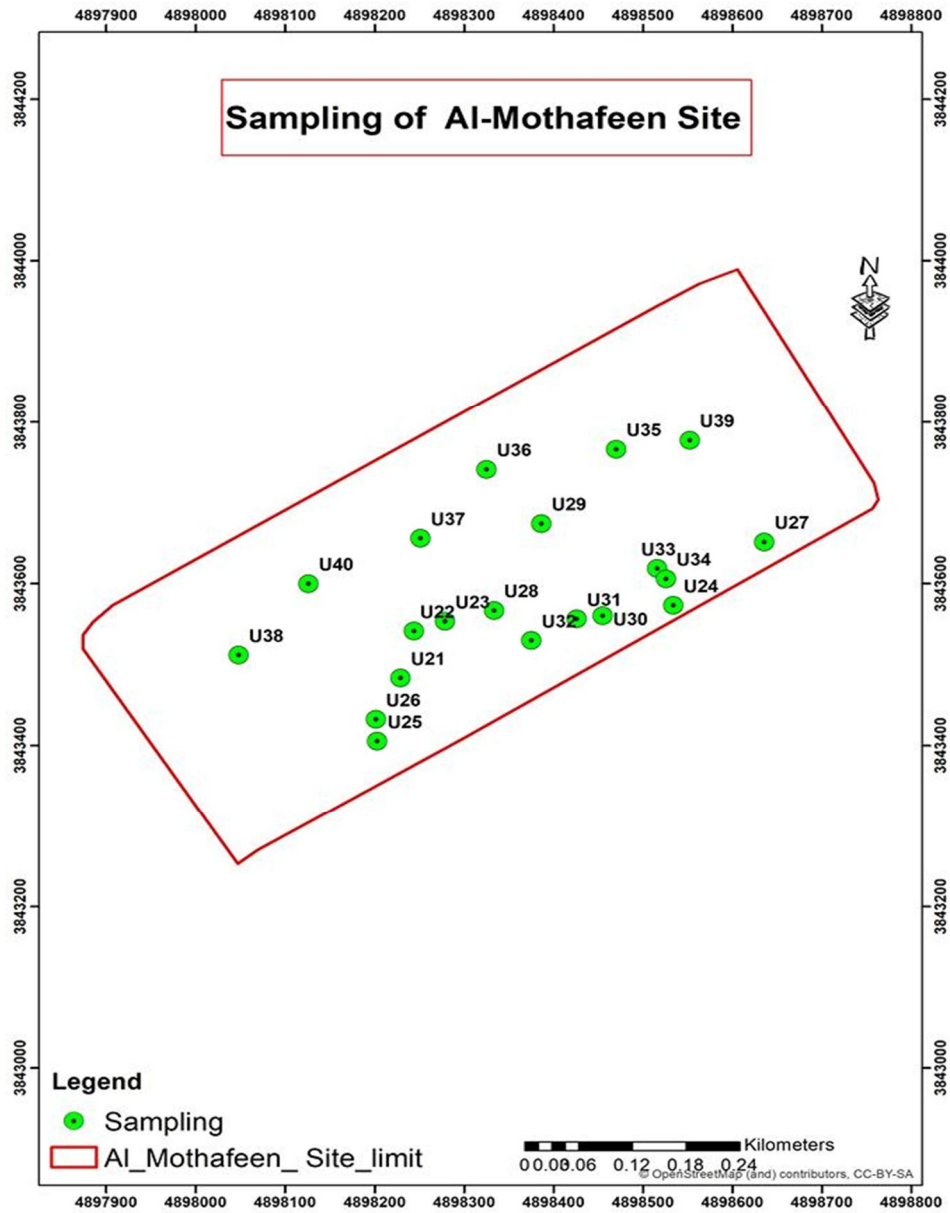


FIG. 2. Map of samples' location for Al-Mothafeen site.

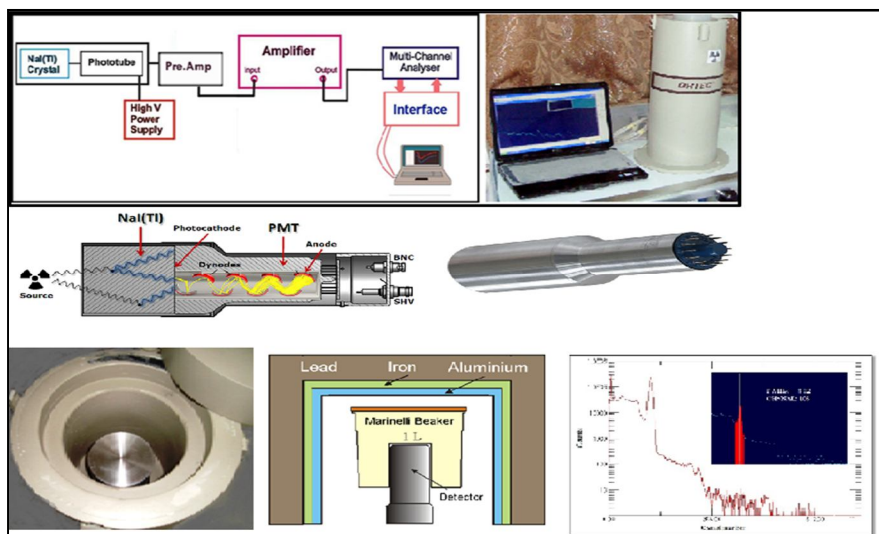


FIG. 3. Diagram of NaI(Tl) system.

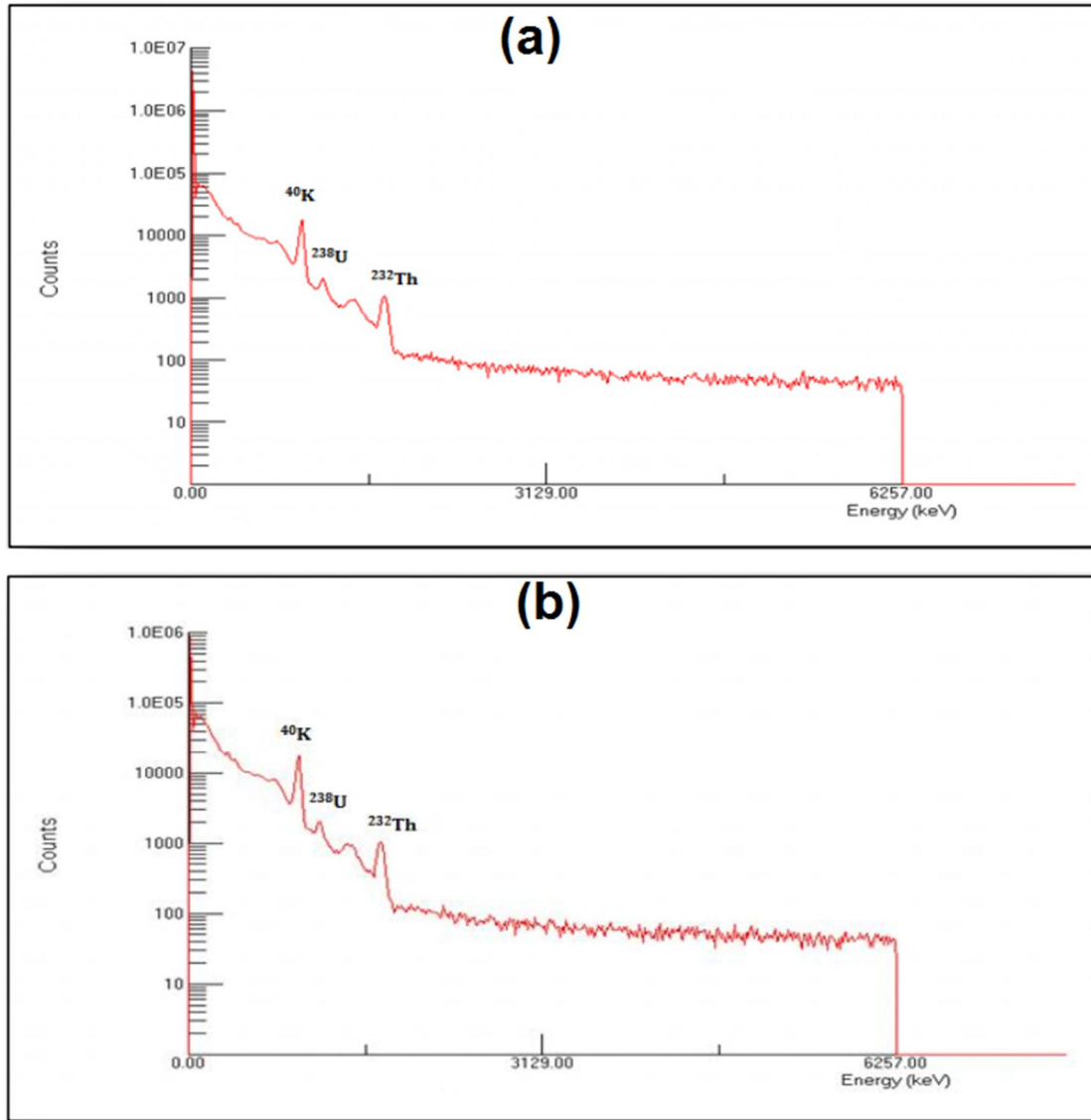


FIG. 4. Gamma-ray spectrum using MAESTRO-32 soft for NaI(Tl) NaI (Tl) (3"×3") for some samples: (a) Sample U1, (b) Sample U21.

Theoretical Equations

Specific Activity (A)

The gamma- ray emitting radionuclide specific activity or which is called the activity concentration within the sample is calculated as per Eq. (1) [10, 11]:

$$A \left(\frac{\text{Bq}}{\text{kg}} \right) = \frac{N}{I_{\gamma} \varepsilon T M} \quad (1)$$

where the symbol A denotes the radionuclide specific activity in the sample, N indicates the net area below the photopeak, I_{γ} denotes the gamma decay probability, ε denotes the gamma-ray detector efficiency, M is the measured sample weight (kg) and T indicates the live time for collecting the spectrum (seconds).

External Hazard Index (H_{ex})

The sample external hazard index can be calculated as per Eq. (2) [12]:

$$H_{ex} = \frac{A_U}{370} + \frac{A_{Th}}{259} + \frac{A_K}{4810} \quad (2)$$

A_U , A_{Th} and A_k stand for the specific activity of ^{238}U , ^{232}Th and ^{40}K , respectively.

Internal Hazard Index (H_{in})

Internal exposure to ^{222}Rn and its radioactive progenies is controlled by the internal hazard index which is calculated as per Eq. (3) [13]:

$$H_{in} = \frac{A_U}{185} + \frac{A_{Th}}{259} + \frac{A_K}{4810} \quad (3)$$

Representative Level Index (I_γ)

Radiation dangers due to the predetermined radionuclides of ^{238}U (^{226}Ra), ^{232}Th , and ^{40}K were evaluated by another parameter called representative level index (I_γ). The following equation can be utilized to determine I_γ for soil samples under study [14]:

$$I_\gamma = \left(\frac{1}{150}\right)A_U + \left(\frac{1}{100}\right)A_{\text{Th}} + \left(\frac{1}{1500}\right)A_K \quad (4)$$

Alpha Index (I_α)

This index has been created to evaluate the impact of an excess of alpha radiation due to the inhaled radon emanating from building materials. This index was resolved utilizing Eq. (5) [12]:

$$I_\alpha = \frac{A_U}{200 \left(\frac{\text{Bq}}{\text{kg}}\right)} \quad (5)$$

Radium Equivalent Activity (Ra_{eq})

The radiological hazard that is accompanied by samples that normally contain radionuclides; namely, ^{238}U , ^{232}Th and ^{40}K , can be evaluated by the radium equivalent activity [15]. It is described mathematically by the following equation:

$$\text{Ra}_{\text{eq}} \left(\frac{\text{Bq}}{\text{kg}}\right) = A_U + 1.43 A_{\text{Th}} + 0.077A_K \quad (6)$$

Exposure Rate (\dot{X})

The rate of gamma-ray exposure in the air, measured at one meter above a thick slab that is infinitely extended, due to ^{238}U , ^{232}Th series and ^{40}K that were uniformly distributed within the material, is equal to [13, 16]:

$$\dot{X} \left(\frac{\mu\text{R}}{\text{h}}\right) = 1.90 A_U + 2.82 A_{\text{Th}} + 0.197A_K \quad (7)$$

\dot{X} is defined as the exposure rate ($\mu\text{R}/\text{h}$). Here, the concentrations of activity are usually given in pCi/g . For each radionuclide in the radioactive series, the average values of the gamma-ray energies are described by the constants presented on the right-hand side of Eq. (7).

Absorbed Dose Rate in Air (D_r)

The major contribution to the rate of absorbed dose in the air arises from the radionuclides of the terrestrial gamma-ray that exist in soil trace amounts. The dose rate measurements are actually depending on measurements of

concentrations of the specific activity of radionuclides, mainly ^{232}Th , ^{238}U and ^{40}K . The report of UNSCEAR 2008 shows that the rate of absorbed dose, 1 meter higher than the ground surface in the air, is described by Eq. (8) [17]:

$$D_r \left(\frac{\text{nGy}}{\text{h}}\right) = 0.462 A_U + 0.604 A_{\text{Th}} + 0.0417A_K \quad (8)$$

Annual Gonadal Equivalent Dose (AGED)

As per UNSCEAR [18], the gonads are viewed as intrigue organs. The yearly gonads' identical portions [AGED] for the occupants in the study site because of particular activities of ^{238}U , ^{232}Th and ^{40}K were determined by utilizing Eq. (9) [19, 20] as:

$$\text{AGED} \left(\frac{\text{mSv}}{\text{y}}\right) = 3.09 A_U + 4.18 A_{\text{Th}} + 0.314A_K \quad (9)$$

Annual Effective Dose Equivalent (AEDE)

The yearly successful portion equivalent (AEDE) is determined from the consumed portion using the portion transformation factor of 0.7 (Sv/Gy) with an outside inhabitation factor of 0.2 as in Eq. (10) [21]:

$$\text{AEDE}_{\text{outdoor}} \left(\frac{\text{mSv}}{\text{y}}\right) = [D_r (\text{mGy}/\text{hr}) \times 8760 \text{ hr} \times 0.2 \times 0.7 \text{ Sv}/\text{Gy}] \times 10^{-6} \quad (10)$$

Excess Lifetime Cancer Risk (ELCR)

This factor measures the cancer probability created over a lifetime span for a given level of exposure. In this factor, 70 years is considered as the normal life-span for an individual. This risk factor can be given by [10, 15]:

$$\text{ELCR} = \text{AEDE} \times \text{DL} \times \text{RF} \quad (11)$$

where $\text{AEDE}_{\text{outdoor}}$ is the outdoor Annual Effective Dose Equivalent, DL is the normal duration of life (70 years as mentioned previously), RF is the risk factor (1/Sv). For the stochastic impact, generally, ICRP utilizes RF as 0.05 for people.

Results and Discussion

The Specific Activity

The radionuclides' specific activities for ^{238}U , ^{232}Th and ^{40}K that were measured in the selected soil samples taken from various locations at the Faculty of Agriculture (Al-Husseineya site) in Kerbala Governorate are presented in Table (1). It is noted that the specific activity of ^{238}U ranged from 6.5 ± 0.6 Bq/kg in sample U1 to 35.1 ± 1.5 Bq/kg in sample U19, with a mean value of 21.7 ± 7.2 Bq/kg, the specific activity of

^{232}Th varied from 3.1 ± 0.2 Bq/kg in sample U20 to 14.2 ± 0.5 Bq/kg in sample U1, with a mean value of 9.4 ± 3.2 Bq/kg. Moreover, the values of ^{40}K were 115.5 ± 2.5 Bq/kg in sample U14 and 419.7 ± 5.6 Bq/kg in sample U6, with a mean value of 335.8 ± 82.2 Bq/kg. The comparison between the specific activities of ^{238}U , ^{232}Th and ^{40}K of Al-Husseineya site in Bq/kg for all the samples is shown in Figs. (5), (6) and (7) which are drawn by GIS technology. The specific activities of ^{40}K , ^{232}Th and ^{238}U that were measured in selected soil samples for different locations at the Faculty of Medicine (Al-Mothafeen site) belonging to Kerbala

Governorate are recorded in Table (2). In Table (2), the specific activity in Bq/kg of ^{238}U ranged from 11.0 ± 0.7 in sample U38 to 41.5 ± 1.4 in sample U34, with a mean value of 22.4 ± 8.8 , the specific activity in Bq/kg for ^{232}Th ranged from 6.1 ± 0.3 in sample U28 to 17.3 ± 0.5 in sample U35, with a mean value of 11.2 ± 3.3 and for ^{40}K , the specific activity ranged from 207.1 ± 3.2 in sample U35 to 448.4 ± 6.0 in sample U27, with a mean value of 333.1 ± 70.7 . The comparison between the specific activities of ^{238}U , ^{232}Th and ^{40}K of Al-Mothafeen site in Bq/kg for all the samples is shown in Figs. (8), (9) and (10) which are drawn by GIS technology.

TABLE 1. Specific activity results at Al-Husseineya site.

No.	Sample code	Specific activity (Bq/kg)					
		Uranium-238		Thorium-323		Potassium-40	
		Average	\pm S.D.	Average	\pm S.D.	Average	\pm S.D.
1	U1	6.5	0.6	14.2	0.5	407.8	4.9
2	U2	25.1	1.1	13.0	0.5	383.5	4.4
3	U3	13.6	0.8	5.8	0.3	294.7	3.8
4	U4	19.9	1.0	5.4	0.3	152.4	2.9
5	U5	27.6	1.3	9.6	0.4	329.1	4.5
6	U6	15.3	1.0	9.6	0.5	419.7	5.6
7	U7	27.1	1.2	11.5	0.5	373.4	4.5
8	U8	28.3	1.4	13.1	0.6	390.8	5.2
9	U9	21.6	1.0	4.7	0.3	246.0	3.6
10	U10	17.1	1.1	8.4	0.5	308.4	4.7
11	U11	23.9	1.2	11.4	0.5	417.1	5.2
12	U12	27.7	1.4	9.3	0.5	365.3	5.2
13	U13	30.1	1.4	9.9	0.5	329.9	4.7
14	U14	24.1	1.1	3.4	0.3	111.5	2.5
15	U15	18.8	0.9	13.4	0.5	290.8	3.9
16	U16	12.1	0.8	10.9	0.4	363.5	4.3
17	U17	20.7	1.1	10.5	0.5	391.2	5.2
18	U18	11.4	0.9	12.8	0.6	417.4	5.6
19	U19	35.1	1.5	8.7	0.4	376.9	5.0
20	U20	29.0	1.1	3.1	0.2	348.3	4.1
	Max.	35.1	1.5	14.2	0.5	419.7	5.6
	Min.	6.5	0.6	3.1	0.2	111.5	2.5
	Average \pm S.D.	21.7 \pm 7.2		9.4 \pm 3.2		335.8 \pm 82.2	
	Worldwide average [11]	35		45		420	

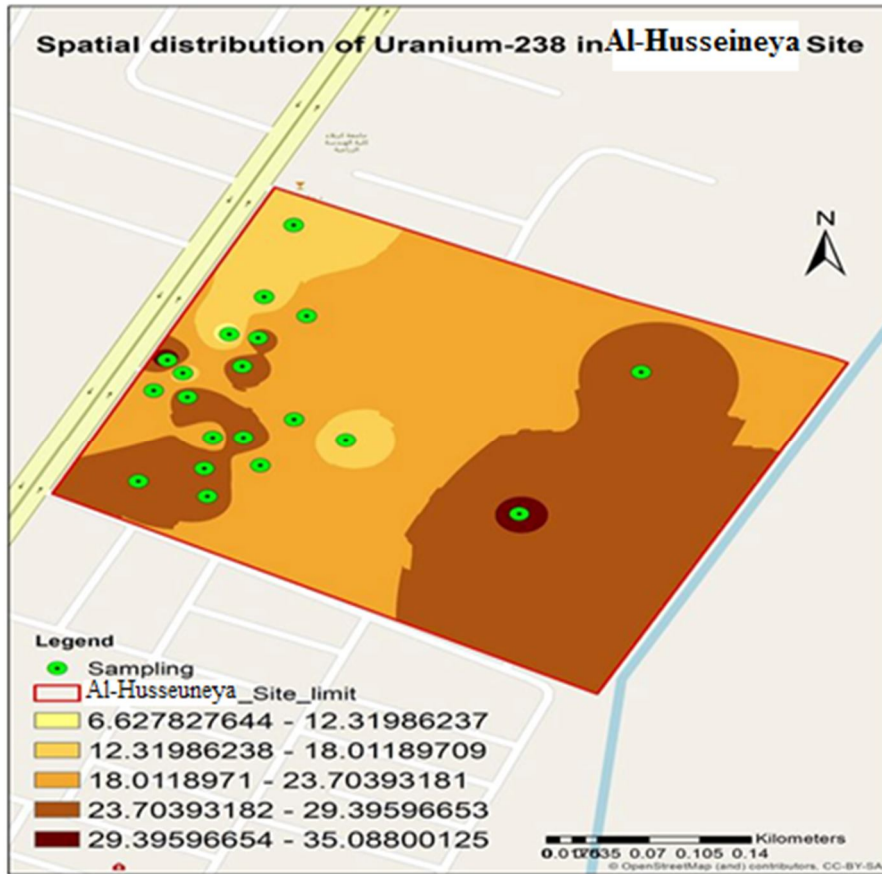


FIG. 5. Spatial distribution map of the specific activity values of ^{238}U using GIS technology.

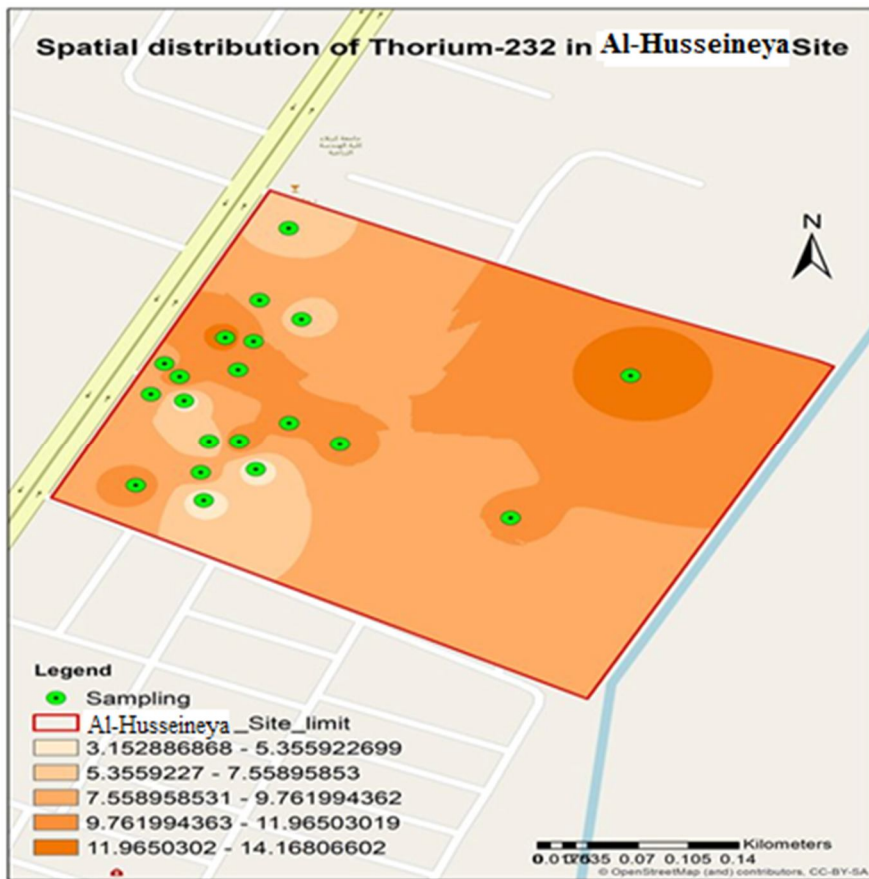


FIG. 6. Spatial distribution map of the specific activity values of ^{232}Th using GIS Technology.

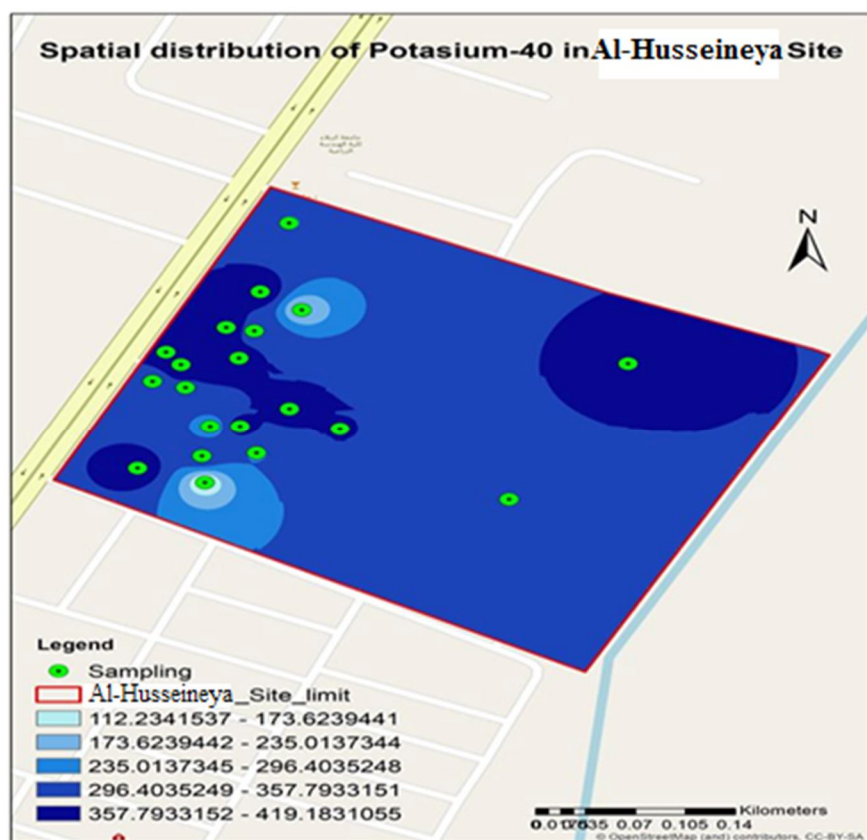


FIG. 7. Spatial distribution map of the specific activity values of ⁴⁰K using GIS technology.

TABLE 2. Specific activity results in Al-Mothafeen site.

No.	Sample code	Specific activity (Bq/kg)					
		Uranium-238		Thorium-323		Potassium-40	
		Average	±S.D.	Average	±S.D.	Average	±S.D.
21	U21	16.3	0.9	11.0	0.5	403.6	4.8
22	U22	14.5	0.9	6.7	0.4	249.5	3.8
23	U23	16.3	1.0	6.1	0.4	360.9	4.8
24	U24	17.6	1.0	11.9	0.5	397.5	5.1
25	U25	37.2	1.5	12.1	0.5	373.7	4.9
26	U26	17.5	1.0	13.0	0.5	313.9	4.6
27	U27	25.1	1.4	17.2	0.7	448.4	6.0
28	U28	17.7	1.0	6.1	0.3	374.4	4.7
29	U29	27.3	1.5	10.5	0.6	314.1	5.3
30	U30	31.4	1.5	10.5	0.5	424.7	5.6
31	U31	32.2	1.2	10.1	0.4	240.4	3.3
32	U32	30.1	1.4	16.8	0.6	340.5	5.0
33	U33	31.1	1.4	14.7	0.6	216.1	3.9
34	U34	41.5	1.4	10.8	0.4	290.5	3.9
35	U35	13.1	0.8	17.3	0.5	207.1	3.2
36	U36	12.4	0.8	10.9	0.4	313.0	4.1
37	U37	12.9	0.8	6.6	0.3	244.6	3.6
38	U38	11.0	0.7	11.2	0.5	348.7	4.4
39	U39	24.4	1.3	10.4	0.5	396.9	5.2
40	U40	18.4	0.9	9.9	0.4	403.7	4.4
	Max.	41.5	1.4	17.3	0.5	448.4	6.0
	Min.	11.0	0.7	6.1	0.3	207.1	3.2
	Average± S.D.	22.4±8.8		11.2±3.3		333.1±70.7	
	Worldwide average [20]	35		45		420	

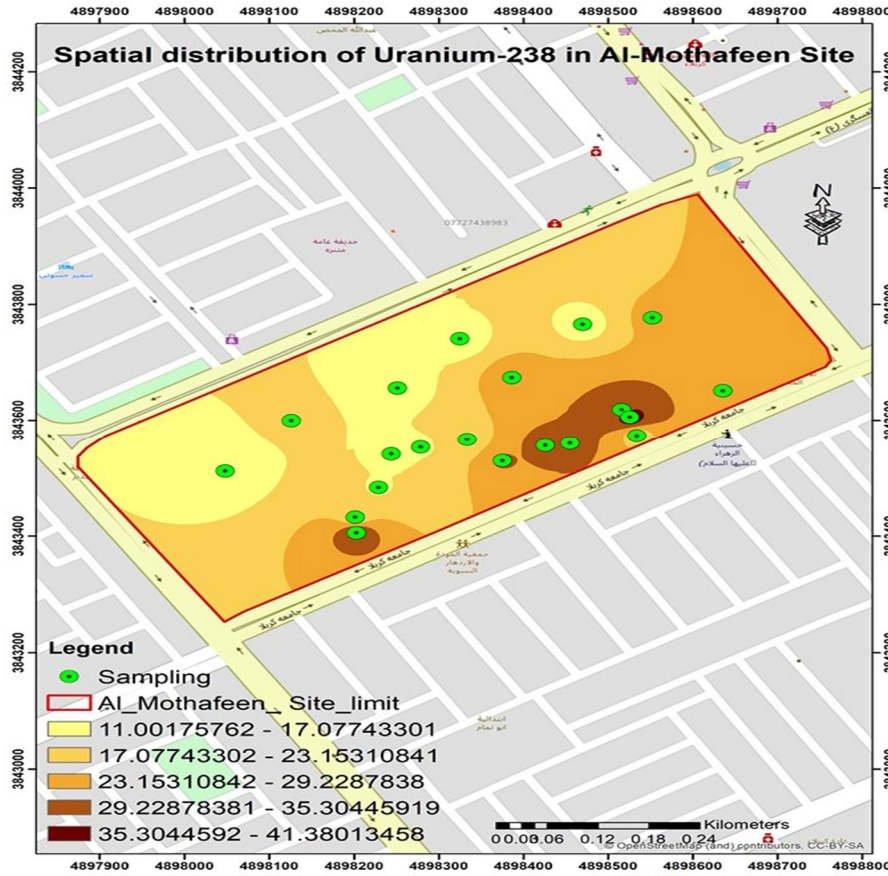


FIG. 8. Spatial distribution map of the specific activity values of ²³⁸U using GIS technology.

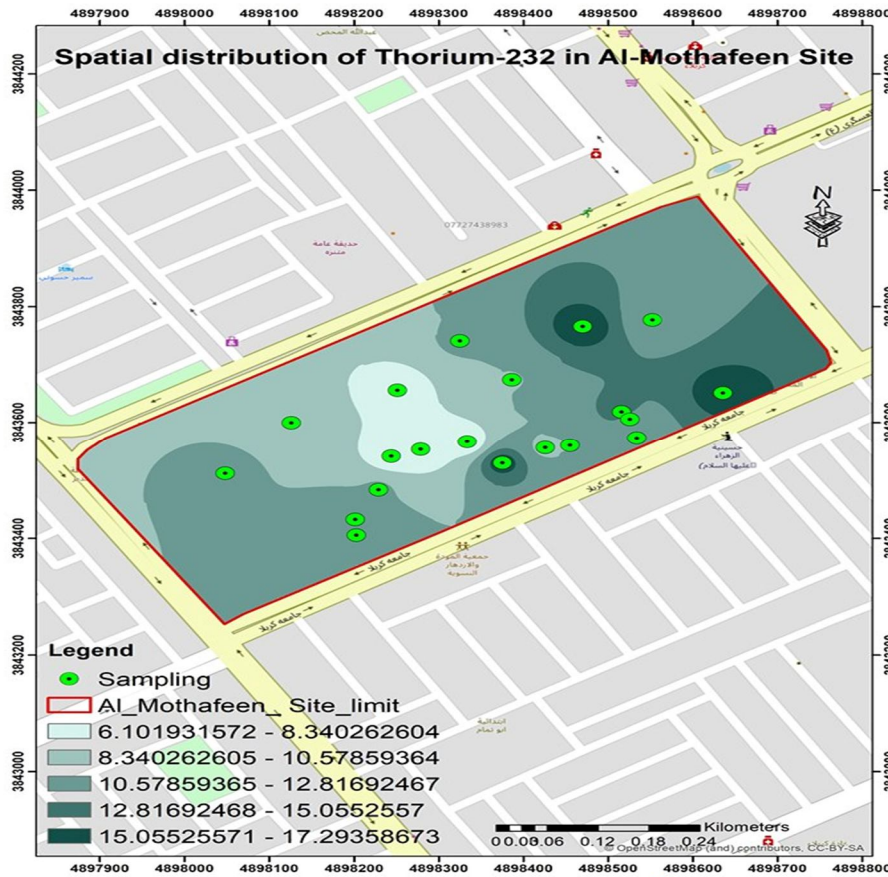


FIG. 9. Spatial distribution map of the specific activity values of ²³²Th using GIS technology.

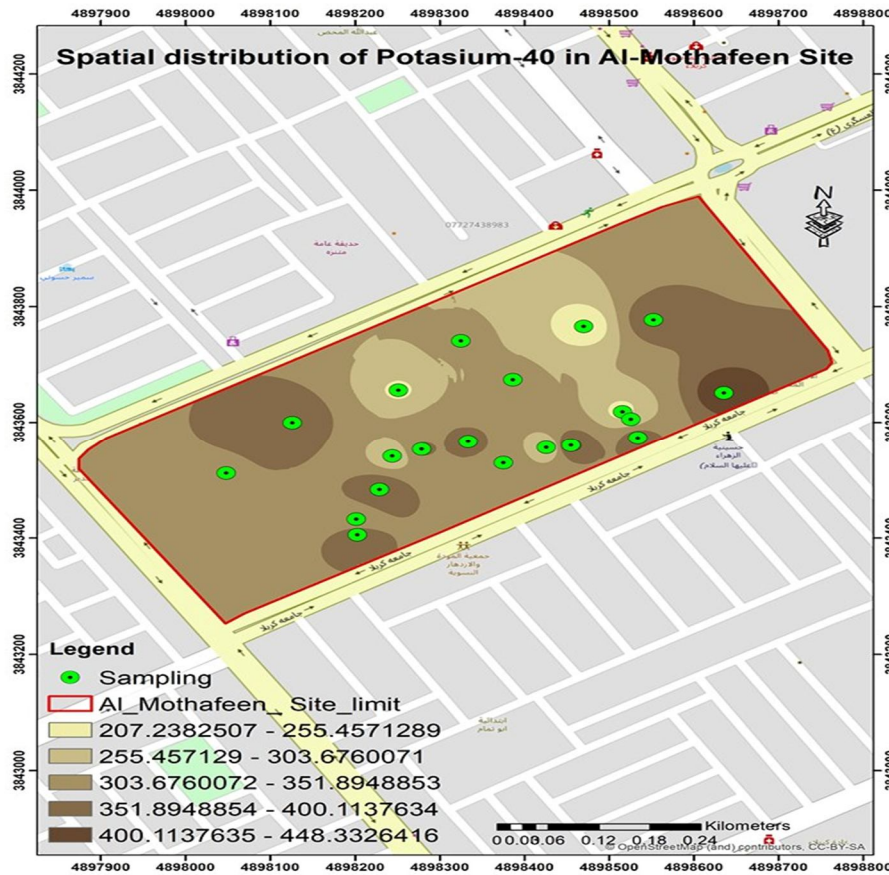


FIG. 10. Spatial distribution map of the specific activity values of ^{40}K using GIS technology.

From the readings of the natural radioactivity concentrations presented in Tables (1) and (2), one can notice that these values are different for ^{238}U , ^{232}Th and ^{40}K due to the differences in the types of soil (different sites) (sandy and clayey) for the locations where the samples are tested. Furthermore, the uranium specific activity is higher than that corresponding to thorium for most of the tested samples. In addition, the specific activity that was measured for ^{40}K is found to exceed noticeably the specific activity values for thorium and uranium, as it is the richest radioactive element. The highest allowable concentration was found in some samples because of the increase in the concentration of potassium nuclide in some areas due to the existence of agricultural land and areas containing phosphate fertilizers, in which potassium (^{40}K) is concentrated. Based on the recommended standard levels, the mean specific activity values of ^{238}U , ^{40}K and ^{232}Th are 35 Bq/kg, 420 Bq/kg and 45 Bq/kg, respectively [11]. It is noted that all specific activity values of ^{238}U (with the exception of U19 in Al-Husseineya site, U25 and U34 in Al-Mothafeen site) are lower than the values recommended by

UNSCEAR 2008 for the world. All specific activity values of ^{232}Th in Al-Husseineya and Al-Mothafeen sites were within the limits recommended by UNSCEAR 2008. For ^{40}K , those values were lower than the mean activity world's values recommended by UNSCEAR 2008 [11]. Exceptions are samples U27 and U30 in Al-Mothafeen site, which might be due to the unnecessary usage of potassium-containing fertilizers in the area near to the sampling sites, which may contribute to the higher values of ^{40}K activity.

Radiological Effects

The values of external and internal hazard indices (H_{ex} and H_{in} , respectively), radium equivalent activity (Ra_{eq}), alpha index (I_{α}), representative level index (I_r), annual gonadal equivalent dose (AGED), exposure rate (\dot{x}), absorbed dose rate in air (Dr), annual effective indoor and outdoor dose equivalent and excess lifetime cancer risk (ELCR) in Al-Husseineya and Al-Mothafeen sites are presented in Tables (3) and (4), respectively. From Table (3), the results of Ra_{eq} (measured in Bq/kg) ranged from 37.5 to 77.1 with a mean value of 61.11 ± 2.589 .

As for H_{ex} , the measured values ranged from 0.101 to 0.208 with a mean value of 0.165 ± 0.0070 . For H_{in} , the measured values ranged from 0.157 to 0.302 with a mean value of 0.224 ± 0.009 . The measured values for I_γ ranged from 0.269 to 0.58 with a mean value of 0.463 ± 0.019 . And for I_α , the measured values ranged from 0.0325 to 0.1755 with a mean value of 0.108 ± 0.0080 . In addition, it was found that the maximum value of \dot{x} in sample U8 was 167.7 $\mu R/h$ and the minimum value in sample U14 was 77.3 $\mu R/h$, with a mean value of 134.1 ± 5.735 $\mu R/h$. The results of D_r ranged from 17.8 nGy/h to 37.3 nGy/h with a mean value of 29.745 ± 1.259 nGy/h. The results of AGED ranged from 123.7 mSv/y to 264.9 mSv/y with a mean value of 212.115 ± 9.031 mSv/y. The values of $AEDE_{outdoor}$ started from 0.022 mSv/y to 0.046 mSv/y, with a mean value of 0.0365 ± 0.0015 mSv/y. At last, the results of ELCR started from 0.077×10^{-3} to 0.160×10^{-3} with a mean value of $0.12775 \pm 0.0053 \times 10^{-3}$. The results of radiological hazard indices (Ra_{eq} , H_{ex} , H_{in} , I_γ and I_α) for Al-Mothafeen site that can be seen from Table 4 are as follows: Ra_{eq} ranged from 41.2 to 84.2 Bq/kg with a mean value of 64.055 ± 2.7 Bq/kg, while H_{ex} ranged from 0.111 to 0.227 with a mean value of 0.173 ± 0.0075 . H_{in} ranged from 0.146 to 0.326 with a mean value of 0.2335 ± 0.0122 . I_γ

ranged from 0.315 to 0.638 with a mean value of 0.4832 ± 0.0199 and I_α ranged from 0.055 to 0.2075 with a mean value of 0.112 ± 0.0098 . The results for \dot{X} ranged from 91.3 $\mu R/h$ to 184.5 $\mu R/h$ with a mean value of 139.73 ± 5.734 $\mu R/h$, while the results for D_r ranged from 20.1 nGy/h to 40.7 nGy/h with a mean value of 31.005 ± 1.313 nGy/h and the results for AGED ranged from 144.3 mSv/y to 290.3 mSv/y with a mean value of 220.60 ± 9.119 mSv/y. The results for $AEDE_{outdoor}$ ranged from 0.025 mSv/y to 0.05 mSv/y with a mean value of 0.038 ± 0.0015 mSv/y and the results for ELCR ranged from 0.086×10^{-3} to 0.175×10^{-3} with a mean value of $0.133 \pm 0.005 \times 10^{-3}$. All values of Ra_{eq} were lower than the acceptable value of 370 [23] (equivalent to 1 ms); therefore, the maximum value in this study lies within the acceptable level. Also, it was found that the results of H_{ex} , H_{in} , I_γ and I_α were less than unity [24]. The values of D_r were lower than the corresponding world mean (55 nGy/h) recommended by UNSCEAR 2000 [22]. AGED values were lower than the corresponding values recommended for the world mean, ≤ 300 mSv/y [12]. All values of $AEDE_{outdoor}$ are lower than the worldwide value, 0.08 mSv/y [25]. ELCR values are small; therefore, the risk of cancer can be ignored.

TABLE 3. Radiological hazard indices for Al-Husseineya site in the present work.

No.	Sample code	Ra_{eq} (Bq/kg)	H_{ex}	H_{in}	I_γ	I_α	Exposure ($\mu R/h$)	D_r (nGy/h)	AGED (mSv/y)	$AEDE_{outdoor}$ (mSv/y)	ELCR $\times 10^{-3}$
1	U1	58.2	0.157	0.175	0.457	0.0325	132.7	28.6	207.5	0.035	0.123
2	U2	73.2	0.198	0.266	0.553	0.1255	159.9	35.4	252.3	0.043	0.152
3	U3	44.6	0.120	0.157	0.345	0.068	100.3	22.1	158.8	0.027	0.095
4	U4	39.4	0.106	0.160	0.288	0.0995	83.1	18.8	131.9	0.023	0.081
5	U5	66.7	0.180	0.255	0.499	0.138	144.3	32.3	228.7	0.040	0.139
6	U6	61.3	0.166	0.207	0.478	0.0765	138.8	30.4	219.2	0.037	0.130
7	U7	72.3	0.195	0.269	0.545	0.1355	157.5	35.0	249.1	0.043	0.150
8	U8	77.1	0.208	0.285	0.580	0.1415	167.7	37.3	264.9	0.046	0.160
9	U9	47.3	0.128	0.186	0.355	0.108	102.8	23.1	163.6	0.028	0.099
10	U10	52.9	0.143	0.189	0.404	0.0855	116.9	25.8	184.8	0.032	0.111
11	U11	72.3	0.195	0.260	0.551	0.1195	159.7	35.3	252.5	0.043	0.152
12	U12	69.1	0.187	0.262	0.521	0.1385	150.8	33.6	239.2	0.041	0.144
13	U13	69.7	0.188	0.270	0.520	0.1505	150.1	33.6	238.0	0.041	0.144
14	U14	37.5	0.101	0.167	0.269	0.1205	77.3	17.8	123.7	0.022	0.077
15	U15	60.4	0.163	0.214	0.453	0.094	130.8	28.9	205.4	0.035	0.124
16	U16	55.7	0.150	0.183	0.432	0.0605	125.3	27.3	197.1	0.034	0.117
17	U17	65.8	0.178	0.234	0.504	0.1035	146.0	32.2	230.7	0.040	0.138
18	U18	61.8	0.167	0.198	0.482	0.057	140.0	30.4	219.8	0.037	0.131
19	U19	76.6	0.207	0.302	0.572	0.1755	165.5	37.2	263.2	0.046	0.160
20	U20	60.3	0.163	0.241	0.457	0.145	132.5	29.8	211.9	0.037	0.128
	Max.	77.1	0.208	0.302	0.269	0.1755	167.7	37.3	264.9	0.046	0.160
	Min.	37.5	0.101	0.157	0.58	0.0325	77.3	17.8	123.7	0.022	0.077
	Average \pm S.D.	61.11 ± 2.5	0.165 ± 0.007	0.224 ± 0.009	0.463 ± 0.01	0.108 ± 0.008	134 ± 5.7	29.7 ± 1.2	212.1 ± 9.0	0.03 ± 0.001	0.12 ± 0.005
	Worldwide mean	<370[23]	<1[24]	<1[24]	<1[24]	<1[24]	-----	55 [22]	≤ 300 [12]	0.08 [25]	-----

TABLE 4. Radiological hazard indices for Al-Mothafeen site in the present work.

No.	Sample code	Ra _{eq} (Bq/kg)	H _{ex}	H _{in}	I _γ	I _α	Exposure (μR/h)	D _r (nGy/h)	AGED (mSv/y)	AEDE _{outdoor} (mSv/y)	ELCR×10 ⁻³
21	U21	63.1	0.170	0.214	0.488	0.0815	141.5	31.0	223.1	0.038	0.133
22	U22	43.3	0.117	0.156	0.330	0.0725	95.6	21.1	151.2	0.026	0.091
23	U23	52.8	0.143	0.187	0.410	0.0815	119.3	26.3	189.2	0.032	0.113
24	U24	65.2	0.176	0.224	0.501	0.088	145.3	31.9	228.9	0.039	0.137
25	U25	83.3	0.225	0.325	0.618	0.186	178.4	40.1	282.9	0.049	0.172
26	U26	60.3	0.163	0.210	0.456	0.0875	131.7	29.0	207.0	0.036	0.125
27	U27	84.2	0.227	0.295	0.638	0.1255	184.5	40.7	290.3	0.050	0.175
28	U28	55.3	0.149	0.197	0.429	0.0885	124.6	27.5	197.8	0.034	0.118
29	U29	66.5	0.180	0.253	0.496	0.1365	143.4	32.1	226.9	0.039	0.138
30	U30	79.1	0.214	0.299	0.597	0.157	172.9	38.6	274.3	0.047	0.166
31	U31	65.2	0.176	0.263	0.476	0.161	137.0	31.0	217.2	0.038	0.133
32	U32	80.3	0.217	0.298	0.596	0.1505	171.6	38.3	270.2	0.047	0.164
33	U33	68.8	0.186	0.270	0.498	0.1555	143.1	32.3	225.4	0.040	0.138
34	U34	79.3	0.214	0.326	0.578	0.2075	166.5	37.8	264.6	0.046	0.162
35	U35	53.8	0.145	0.181	0.398	0.0655	114.5	25.1	177.8	0.031	0.108
36	U36	52.1	0.141	0.174	0.400	0.062	116.0	25.4	182.2	0.031	0.109
37	U37	41.2	0.111	0.146	0.315	0.0645	91.3	20.1	144.3	0.025	0.086
38	U38	53.9	0.145	0.175	0.418	0.055	121.2	26.4	190.3	0.032	0.113
39	U39	69.8	0.189	0.255	0.531	0.122	153.9	34.1	243.5	0.042	0.146
40	U40	63.6	0.172	0.222	0.491	0.092	142.4	31.3	225.0	0.038	0.134
	Max.	84.2	0.227	0.326	0.638	0.2075	184.5	40.7	290.3	0.05	0.175
	Min.	41.2	0.111	0.146	0.315	0.055	91.3	20.1	144.3	0.025	0.086
	Average	64.1	0.173	0.233	0.483	0.112	139.7	31.0	220.6	0.038	0.133
	± S.D.	±2.7	±0.007	±0.012	±0.019	±0.009	±5.7	±1.3	±9.1	±0.001	±0.006
	Worldwide mean	<370[23]	<1[24]	<1 [24]	<1 [24]	<1 [24]	-----	55 [22]	≤ 300 [12]	0.08 [25]	-----

The results of this study; namely, the mean specific activities for ²³⁸U, ²³²Th and ⁴⁰K are compared to other results recorded in different

countries and different locations in Iraq. The comparison results are listed in Table 5.

TABLE 5. Comparison between current work and other works for different countries and locations.

Country/Location	Specific Activity in Bq/kg			Reference
	²³⁸ U	²³² Th	⁴⁰ K	
Qatar	25.5	7.7	165.8	[26]
Jordan	49	70	291	[27]
Kuwait	3.82	11.27	384.47	[28]
Egypt	27	31.4	427.5	[29]
Malaysia	127	304	302	[30]
Thailand	64.48	67.04	447.7	[31]
Iran	23	31	453	[32]
Libya	7.5	4.2	27.5	[33]
Baghdad	14.09	11.53	402	[17]
Babylon	14.07	12.32	416.65	[18]
Kerbala	19.45	24.47	245.1	[15]
Kurdistan	83.33	19.147	284.86	[16]
Missan	21.19	9.72	453.91	[20]
Kerbala / Al-Husseineya site	21.7±7.2	9.4±3.2	335.8±82.2	Present study
Kerbala / Al-Mothafeen site	22.4±8.8	11.2±3.3	333.1±70.7	

The mean values of specific activity for ²³²Th and ²³⁸U in Al-Mothafeen site were the highest mean values of specific activity of natural radioactivity of Al-Husseineya site, while specific activity for ⁴⁰K in Al-Husseineya site was larger than in Al-Mothafeen site. These differences are attributable to the geological characteristics of the layers of the soil under study.

This result of the radiological hazard index is still compatible with the acceptable limits and lower than the action levels based on UNSCEAR, OCDE and ICRP, as well as with other studies in Iraq and in other countries. Indeed, the study area is safe and posing no significant radiological threat to the population.

Conclusion

The specific activity values for ^{232}Th , ^{238}U and ^{40}K for several samples of soil at some locations of the Faculty of Agriculture (Al-Husseineya site) and the Faculty of Medicine (Al-Mothafeen site) in Kerbala Governorate. The uranium-238 activities were within the normal values for all samples of the studied areas except for three samples that showed higher values than the worldwide average range, while the activities

for potassium-40 radionuclide in all samples were higher than the worldwide average range except for some samples and the activities for thorium-232 for all samples were lower than the worldwide average range. Radiological hazard index in all soil samples of the present study was lower than the permissible limit; thus, it can be concluded that the study area is radioactively safe.

References

- [1] Hoover, M.D. et al., *Health Physics*, 108 (2) (2015) 179.
- [2] Lilley, J., "Nuclear physics: Principles and applications", (John Wiley & Sons, 2013).
- [3] Cember, H., Johnson, T.E. and Alaei, P., *Medical Physics*, 35 (12) (2008) 5959.
- [4] Eisenbud, M. and Gesell, T.F., "Environmental Radioactivity from Natural, Industrial and Military Sources", (Elsevier, 1997).
- [5] Durrance, E.M., "Radioactivity in Geology: Principles and Applications", (1986).
- [6] Linton, O.W. and Mettler Jr, F.A., National Council on Radiation Protection and Measurements. In: National Conference on Dose Reduction in CT, with an Emphasis on Pediatric Patients. *AJR Am. J. Roentgenol.* (2003).
- [7] Wang, Z., Natural radiation environment in China. In: International Congress Series, (Elsevier, 2002).
- [8] Abojassim, A.A. et al., *International Journal of Environmental Analytical Chemistry*, 100 (1) (2020) 99.
- [9] Aswood, M.S., Abojasim, A.A. and Al-Musawi, M.S.A., *Radiation Detection: Technology and Methods*, 3 (4) (2019) 57.
- [10] Abojasim, A.A., Oleiwi, M.H. and Hassan, M., *Nuclear Physics and Atomic Energy*, 17 (3) (2016) 308.
- [11] UNSCEAR., "Effects of ionizing radiation: Report to the General Assembly, with scientific annexes", Vol. 1. (United Nations Publications, 2008).
- [12] Okogbue, C. and Nweke, M., *J. Environ. Geol.*, 2 (1) (2018) 14.
- [13] Tanasković, I., Golobocanin, D. and Miljević, N., *Journal of Geochemical Exploration*, 112 (2012) 226.
- [14] Trevisi, R. et al., *Journal of Environmental Radioactivity*, 105 (2012) 11.
- [15] Kadhim, I.H. and Muttaleb, M.K., *International Journal of Chem. Tech. Research*, 9 (08) (2016) 228.
- [16] Yousuf, R.M. and Abullah, K.O., *ARPN Journal of Science and Technology*, 3 (6) (2013) 632.
- [17] Tawfiq, N.F., Mansour, H. and Karim, M., *International Journal of Recent Research and Review*, 8 (1) (2015) 1.
- [18] Hatif, K.H., *Journal of Kerbala University*, 13 (1) (2015) 103.
- [19] Jaffer, M., Doctoral Dissertation, M.Sc. Thesis, University of Kufa, (2013).
- [20] Jassim, A., Al-Gazaly, H. and Abojasim, A., *Journal of Environmental Science and Pollution Research*, 2 (1) (2016) 39.
- [21] Lindell, B., Dunster, H.J. and Valentin, J., *Chinese Journal of Radiological Health*, 8 (1) (1999) 1.
- [22] UNSCEAR., "Sources and effects of ionizing radiation: Sources", Vol. 1. (United Nations Publications, 2000).
- [23] Agency, N.E., "Exposure to radiation from the natural radioactivity in building materials", report: OECD, (1979).
- [24] ICRP., "Radiological Protection Principles concerning the Natural Radioactivity of Building Materials Radiation Protection", *Radiological Protection* 112, (1999).

- [25] ICRP., "Age-dependent Doses to Members of the Public from Intake of Radionuclides - Part 2: Ingestion Dose Coefficients", Vol. 67, (Elsevier Health Sciences, 1994).
- [26] Al-Sulaiti, H. et al., Nuclear Instruments and Methods in Physics Research-Section A: Accelerators, Spectrometers, Detectors and Associated Equipment, 619 (1-3) (2010) 427.
- [27] Al-Hamarneh, I.F. and Awadallah, M.I., Radiation Measurements, 44 (1) (2009) 102.
- [28] Saad, H. and Al-Azmi, D., Applied Radiation and Isotopes, 56 (6) (2002) 991.
- [29] Agbalagba, E. and Onoja, R., Journal of Environmental Radioactivity, 102 (7) (2011) 667.
- [30] Ramli, A.T., Apriantoro, N.H. and Wagiran, H., "Assessment of radiation dose rates in the high terrestrial gamma radiation area of Selama District, Perak, Malaysia." Applied Physics Research 1.2 (2009): 45.
- [31] Beierle, T.C., "Democracy in practice: Public participation in environmental decisions", (Routledge, 2010).
- [32] El Mamoney, M. and Khater, A.E., Journal of Environmental Radioactivity, 73 (2) (2004) 151.
- [33] Saleh Kotahi, M., Iranian Journal of Medical Physics, 14 (2) (2017) 98.

Authors Index

A. A. Ajayi.....	111
Abdalsattar K. Hashim.....	177
Abrrar A. Ibrahim	177
Ali A. Abojassim.	177
Amal M. Banoosh.....	129
Ayuk Usaji Atu.....	139
Casey Reason	161
Donald Dunn	161
Emmanuel I. Akaerue	117
F. Qamar.....	169
Fuad Rawwagah	155
Hitler Louis	139
I. M. Odeh.....	101
Israel Solomon Etim.....	139
M. Nahili	169
Marwan S. Mousa	161
N. Hamdadou	101
Ndianabasi. H. Valentine	117
Nelson Ibe Nzeata	139
O. W. Abodunrin	111
Ogri J. Ushie.....	117
Rajaa A. Basheer.....	129
Salah M. Jaradat	161
Waleed I. Al-Rijabo.....	129

Subject Index

Cadmium.....	169
Clearness index.....	129
Concentration-concentration fluctuation.....	111
Coupled plasmon surface modes.....	155
CV.....	129
Darken stability function.....	111
DFT.....	139
Diacetylaminoazopyrimidine.....	139
DSSCs.....	139
Excited state.....	139
Extraterrestrial radiation.....	129
Fingerprint.....	117
Gamma-ray.....	177
Global solar radiation.....	129
GPS.....	117
IBAD.....	101
Karbel University.....	177
MCNP5-beta code.....	169
Module.....	117
NaI (Tl).....	177
Natural radioactivity.....	177
Neutron flux.....	169
Neutronic irradiator.....	169
Ordering energy.....	111
Plasma slab waveguide.....	155
Ra-Be radiation source.....	169
Radiological hazard.....	177
Roger's diffusion of innovations theory.....	161
SD.....	129
Simulation.....	161
Soil.....	177
Spectroscopy.....	139
Structural and optical properties.....	101
Time series.....	129
TiO ₂ thin film.....	101
Tracking system.....	117
Upper hybrid modes.....	155
Virtual lab.....	161
XRD.....	101

المراجع: يجب طباعة المراجع بأسطر مزدوجة ومرقمة حسب تسلسلها في النص. وتكتب المراجع في النص بين قوسين مربعين. ويتم اعتماد اختصارات الدوريات حسب نظام Wordlist of Scientific Reviewers.

الجدول: تعطى الجداول أرقاماً متسلسلة يشار إليها في النص. ويجب طباعة كل جدول على صفحة منفصلة مع عنوان فوق الجدول. أما الحواشي التفسيرية، التي يشار إليها بحرف فوقي، فتكتب أسفل الجدول.

الرسوم التوضيحية: يتم ترقيم الأشكال والرسومات والرسومات البيانية (المخططات) والصور، بصورة متسلسلة كما وردت في النص.

تقبل الرسوم التوضيحية المستخرجة من الحاسوب والصور الرقمية ذات النوعية الجيدة بالأبيض والأسود، على أن تكون أصيلة وليست نسخة عنها، وكل منها على ورقة منفصلة ومعرفة برقمها بالمقابل. ويجب تزويد المجلة بالرسومات بحجمها الأصلي بحيث لا تحتاج إلى معالجة لاحقة، وألا تقل الحروف عن الحجم 8 من نوع Times New Roman، وألا تقل سماكة الخطوط عن 0.5 وكتافة متجانسة. ويجب إزالة جميع الألوان من الرسومات ما عدا تلك التي ستنشر ملونة. وفي حالة إرسال الرسومات بصورة رقمية، يجب أن تتوافق مع متطلبات الحد الأدنى من التمايز (1200 dpi Resolution) لرسومات الأبيض والأسود الخطية، و 600 dpi للرسومات باللون الرمادي، و 300 dpi للرسومات الملونة. ويجب تخزين جميع ملفات الرسومات على شكل (jpg)، وأن ترسل الرسوم التوضيحية بالحجم الفعلي الذي سيظهر في المجلة. وسواء أرسل المخطوط بالبريد أو عن طريق الشبكة (Online)، يجب إرسال نسخة ورقية أصلية ذات نوعية جيدة للرسومات التوضيحية.

مواد إضافية: تشجع المجلة الباحثين على إرفاق جميع المواد الإضافية التي يمكن أن تسهل عملية التحكيم. وتشمل المواد الإضافية أي اشتقاقات رياضية مفصلة لا تظهر في المخطوط.

المخطوط المنقح (المعدل) والأقراص المدمجة: بعد قبول البحث للنشر وإجراء جميع التعديلات المطلوبة، فعلى الباحثين تقديم نسخة أصلية ونسخة أخرى مطابقة للأصلية مطبوعة بأسطر مزدوجة، وكذلك تقديم نسخة إلكترونية تحتوي على المخطوط كاملاً مكتوباً على Microsoft Word for Windows 2000 أو ما هو استجد منه. ويجب إرفاق الأشكال الأصلية مع المخطوط النهائي المعدل حتى لو تم تقديم الأشكال إلكترونياً. وتخزن جميع ملفات الرسومات على شكل (jpg)، وتقدم جميع الرسومات التوضيحية بالحجم الحقيقي الذي ستظهر به في المجلة. ويجب إرفاق قائمة ببرامج الحاسوب التي استعملت في كتابة النص، وأسماء الملفات على قرص مدمج، حيث يعلم القرص بالاسم الأخير للباحث، وبالرقم المرجعي للمخطوط للمراسلة، وعنوان المقالة، والتاريخ. ويحفظ في مغلف واقٍ.

حقوق الطبع

يُشكّل تقديم مخطوط البحث للمجلة اعترافاً صريحاً من الباحثين بأن مخطوط البحث لم يُنشر ولم يُقدّم للنشر لدى أي جهة أخرى كانت وبأي صيغة ورقية أو إلكترونية أو غيرها. ويشتترط على الباحثين ملء نموذج يُنصّ على نقل حقوق الطبع لتصبح ملكاً لجامعة اليرموك قبل الموافقة على نشر المخطوط. ويقوم رئيس التحرير بتزويد الباحثين بإنموذج نقل حقوق الطبع مع النسخة المُرسلة للتتقيح. كما ويُمنع إعادة إنتاج أي جزء من الأعمال المنشورة في المجلة من دون إذن خطّي مُسبق من رئيس التحرير.

إخلاء المسؤولية

إن ما ورد في هذه المجلة يعبر عن آراء المؤلفين، ولا يعكس بالضرورة آراء هيئة التحرير أو الجامعة أو سياسة اللجنة العليا للبحث العلمي أو وزارة التعليم العالي والبحث العلمي. ولا يتحمل ناشر المجلة أي تبعات مادية أو معنوية أو مسؤوليات عن استعمال المعلومات المنشورة في المجلة أو سوء استعمالها.

الفهرسة: المجلة مفهرسة في:



المجلة الأردنية للفيزياء هي مجلة بحوث علمية عالمية متخصصة مُحكمة تصدر بدعم من صندوق دعم البحث العلمي، وزارة التعليم العالي والبحث العلمي، عمان، الأردن. وتقوم بنشر المجلة عمادة البحث العلمي والدراسات العليا في جامعة اليرموك، إربد، الأردن. وتنتشر البحوث العلمية الأصيلة، إضافة إلى المراسلات القصيرة Short Communications، والملاحظات الفنية Technical Notes، والمقالات الخاصة Feature Articles، ومقالات المراجعة Review Articles، في مجالات الفيزياء النظرية والتجريبية، باللغتين العربية والإنجليزية.

تقديم مخطوط البحث

تقدم البحوث عن طريق إرسالها إلى البريد الإلكتروني : jjp@yu.edu.jo

تقديم المخطوطات إلكترونياً: اتبع التعليمات في موقع المجلة على الشبكة العنكبوتية.

ويجري تحكيم البحوث الأصيلة والمراسلات القصيرة والملاحظات الفنية من جانب مُحكمين اثنين في الأقل من ذوي الاختصاص والخبرة. وتُشجّع المجلة الباحثين على اقتراح أسماء المحكمين. أما نشر المقالات الخاصة في المجالات الفيزيائية النشطة، فيتم بدعوة من هيئة التحرير، ويُشار إليها كذلك عند النشر. ويُطلب من كاتب المقال الخاص تقديم تقرير واضح يتسم بالدقة والإيجاز عن مجال البحث تمهيداً للمقال. وتنتشر المجلة أيضاً مقالات المراجعة في الحقول الفيزيائية النشطة سريعة التغير، وتشجّع كاتبي مقالات المراجعة أو مُستكثبيها على إرسال مقترح من صفحتين إلى رئيس التحرير. ويُرفق مع البحث المكتوب باللغة العربية ملخص (Abstract) وكلمات دالة (Keywords) باللغة الإنجليزية.

ترتيب مخطوط البحث

يجب أن تتم طباعة مخطوط البحث ببنت 12 نوعه Times New Roman، وبسطر مزدوج، على وجه واحد من ورق A4 (21.6 × 27.9 سم) مع حواشي 3.71 سم، باستخدام معالج كلمات ميكروسوفت وورد 2000 أو ما استُجد منه. ويجري تنظيم أجزاء المخطوط وفق الترتيب التالي: صفحة العنوان، الملخص، رموز التصنيف (PACS)، المقدمة، طرق البحث، النتائج، المناقشة، الخلاصة، الشكر والعرفان، المراجع، الجداول، قائمة بدليل الأشكال والصور والإيضاحات، ثم الأشكال والصور والإيضاحات. وتُكتب العناوين الرئيسة بخط غامق، بينما تُكتب العناوين الفرعية بخط مائل.

صفحة العنوان: وتشمل عنوان المقالة، أسماء الباحثين الكاملة وعناوين العمل كاملة. ويكتب الباحث المسؤول عن المراسلات اسمه مشاراً إليه بنجمة، والبريد الإلكتروني الخاص به. ويجب أن يكون عنوان المقالة موجزاً وواضحاً ومعبراً عن فحوى (محتوى) المخطوط، وذلك لأهمية هذا العنوان لأغراض استرجاع المعلومات.

الملخص: المطلوب كتابة فقرة واحدة لا تزيد على مائتي كلمة، موضحة هدف البحث، والمنهج المتبع فيه والنتائج وأهم ما توصل إليه الباحثون.

الكلمات الدالة: يجب أن يلي الملخص قائمة من 4-6 كلمات دالة تعبر عن المحتوى الدقيق للمخطوط لأغراض الفهرسة.

PACS: يجب إرفاق الرموز التصنيفية، وهي متوافرة في الموقع <http://www.aip.org/pacs/pacs06/pacs06-toc.html>.

المقدمة: يجب أن توضّح الهدف من الدراسة وعلاقتها بالأعمال السابقة في المجال، لا أن تكون مراجعة مكثفة لما نشر (لا تزيد المقدمة عن صفحة ونصف الصفحة مطبوعة).

طرائق البحث (التجريبية / النظرية): يجب أن تكون هذه الطرائق موضحة بتفصيل كاف لإتاحة إعادة إجرائها بكفاءة. ولكن باختصار مناسب، حتى لا تكون تكراراً للطرائق المنشورة سابقاً.

النتائج: يستحسن عرض النتائج على صورة جداول وأشكال حيثما أمكن، مع شرح قليل في النص ومن دون مناقشة تفصيلية.

المناقشة: يجب أن تكون موجزة وتركز على تفسير النتائج.

الاستنتاج: يجب أن يكون وصفاً موجزاً لأهم ما توصلت إليه الدراسة ولا يزيد عن صفحة مطبوعة واحدة.

الشكر والعرفان: الشكر والإشارة إلى مصدر المنح والدعم المالي يكتبان في فقرة واحدة تسبق المراجع مباشرة.

Jordan Journal of

PHYSICSAn International Peer-Reviewed Research Journal issued by the
Support of the Scientific Research Support Fund

Published by the Deanship of Research & Graduate Studies, Yarmouk University, Irbid, Jordan

Name: الأسم:
 Specialty:..... التخصص:
 Address: العنوان:
 P.O. Box:..... صندوق البريد:
 City & Postal Code: المدينة/الرمز البريدي:
 Country: الدولة:
 Phone: رقم الهاتف:
 Fax No:..... رقم الفاكس:
 E-mail:..... البريد الإلكتروني:
 No. of Subscription: عدد الاشتراكات:
 Method of Payment:..... طريقة الدفع:
 Amount Enclosed:..... المبلغ المرفق:
 Signature: التوقيع:

Cheques should be paid to Deanship of Research and Graduate Studies - Yarmouk University.

I would like to subscribe to the Journal
For

- One Year
 Two Years
 Three Years

One Year Subscription Rates

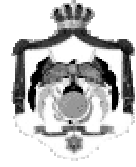
	Inside Jordan	Outside Jordan
Individuals	JD 8	€ 40
Students	JD 4	€ 20
Institutions	JD 12	€ 60

Correspondence**Subscriptions and Sales:**

Prof. Ibrahim O. Abu Al-Jarayesh
 Deanship of Research and Graduate Studies
 Yarmouk University
 Irbid – Jordan
Telephone: 00 962 2 711111 Ext. 2075
Fax No.: 00 962 2 721121



جامعة اليرموك



المملكة الأردنية الهاشمية

المجلة الأردنية

للفيزياء

مجلة بحوث علمية عالية متخصصة محكمة
تصدر بدعم من صندوق دعم البحث العلمي

المجلة الأردنية
للفيزياء
مجلة بحوث علمية عالمية محكمة

المجلد (14)، العدد (2)، حزيران 2021م / ذو القعدة 1442هـ

المجلة الأردنية للفيزياء: مجلة علمية عالمية متخصصة محكمة تصدر بدعم من صندوق دعم البحث العلمي، عمان، الأردن، وتصدر عن عمادة البحث العلمي والدراسات العليا، جامعة اليرموك، إربد، الأردن.

رئيس التحرير:

ابراهيم عثمان أبو الجرايش

قسم الفيزياء، جامعة اليرموك، إربد، الأردن.
ijaraysh@yu.edu.jo

هيئة التحرير:

نبيل يوسف أيوب

رئيس الجامعة الأمريكية في مادبا، مادبا، الأردن.
nabil.ayoub@gju.edu.jo

جميل محمود خليفة (رحمه الله)

قسم الفيزياء، الجامعة الأردنية، عمان، الأردن.
jkalifa@ju.edu.jo

طارق فتحي حسين

قسم الفيزياء، الجامعة الأردنية، عمان، الأردن.
t.hussein@ju.edu.jo

مروان سليمان موسى

قسم الفيزياء، جامعة مؤتة، الكرك، الأردن.
mmousa@mutah.edu.jo

محمد خالد الصغير

قسم الفيزياء، الجامعة الهاشمية، الزرقاء، الأردن.
msugh@hu.edu.jo

عبد المجيد الياسين

قسم الفيزياء، جامعة اليرموك، إربد، الأردن.
alyassin@yu.edu.jo

محمد العمري

قسم الفيزياء، جامعة العلوم والتكنولوجيا، إربد، الأردن.
alakmoh@just.edu.jo

إبراهيم البصول

قسم الفيزياء، جامعة آل البيت، المفرق، الأردن.
Ibrahimbsoul@yahoo.com

سكرتير التحرير: مجدي الشناق

ترسل البحوث إلى العنوان التالي:

الأستاذ الدكتور إبراهيم عثمان أبو الجرايش
رئيس تحرير المجلة الأردنية للفيزياء
عمادة البحث العلمي والدراسات العليا، جامعة اليرموك
إربد، الأردن

هاتف 00 962 2 7211111 فرعي 2075

E-mail: jjp@yu.edu.jo Website: <http://Journals.yu.edu.jo/jjp>